GRADUATE COURSE IN PHYSICS UNIVERSITY OF PISA

THE SCHOOL OF GRADUATE STUDIES IN BASIC SCIENCE "GALILEO GALILEI"
Scuola di Dottorato in Scienze di base "Galileo Galilei"

PhD thesis

Online trigger processing for the NA62 rare kaon decay experiment

Candidate:
Jacopo Pinzino

Supervisor:
Prof. Marco Sozzi

Dottorato di Ricerca in Fisica XXVII ciclo

Contents

List of Figures

List of Tables

Introduction

The work reported in this thesis has been performed within the Trigger and Data Acquisition (TDAQ) working group of the CERN NA62 experiment, with the purpose of studying and developing the trigger system essential for the collection of rare kaon decays. The NA62 experiment is located in the CERN North Area SPS extraction site and it aims at measuring the Branching Ratio of the ultra-rare decay $K^+ \to \pi^+\nu\overline{\nu}$ in order to provide a stringent test of the Standard Model. The theoretical introduction of the $K^+ \to \pi^+\nu\overline{\nu}$ decay and the NA62 experimental strategy are described in chapter 1. In chapter 2 the NA62 experimental setup is described, composed of an upstream part, with detectors used to identify and measure the propriety of the K^+ inside the beam, and a downstream part where the decay products are detected. The first part of this work concerns the development of the common Trigger and Data Acquisition system for the majority of detectors in NA62. The system, the boards and the firmwares are presented in chapter 3. The second part of the work describes in chapter 4 the studies of both hardware low-level (L0) and software high-level triggers for the selection of the $K^+ \to \pi^+\nu\overline{\nu}$ decay, on the real data collected in 2015. The chapter 5 focuses on the development of a L1 trigger algorithm for the NA62 STRAW spectrometer, essential to reach the design rate for the L1 event output.

Chapter 1

Theoretical and experimental framework

1.1 Introduction

The NA62 experiment is located in the CERN North Area SPS extraction site and aims at measuring the Branching Ratio of the ultra-rare decay $K^+ \to \pi^+\nu\overline{\nu}$, collecting about 100 events in two years of data taking. This decay, with its neutral partner $K_L \to \pi^0\nu\overline{\nu}$, is a very useful process to study flavour physics and to obtain a stringent test of the Standard Model; in fact the Branching Ratio of these decays can be computed with high precision within the Standard Model (SM) [37].

$$BR(K^+ \to \pi^+\nu\overline{\nu})(SM) = (7.81^{+0.80}_{-0.71} \pm 0.29) \times 10^{-11} \tag{1.1}$$

$$B(K_L \to \pi^0\nu\overline{\nu}) = (2.43^{+0.40}_{-0.37} \pm 0.06) \times 10^{-11}. \tag{1.2}$$

The first error is related to the uncertainties in the input parameters, the second error quantifies the remaining theoretical uncertainties. The uncertainties in the Branching Ratio are dominated by the knowledge of the CKM mixing matrix parameters, but the purely theoretical error is unusually low, about 2%, because this decay is suppressed by a quadratic GIM mechanism[58] and is dominated by short-distance dynamics. The short-distance amplitude is controlled by one single semileptonic operator whose hadronic matrix element, usually the most important source of uncertainties, can be obtained precisely from the experimental measure of $K^+ \to \pi^0 e^+\nu$ decay. The combination of the Branching Ratio of these two decays ($K^+ \to \pi^+\nu\overline{\nu}$ and $K^0 \to \pi^0\nu\overline{\nu}$) would allow to determine the β angle of the Unitarity Triangle and to have a powerful test on Standard Model.

The $K^+ \to \pi^+\nu\overline{\nu}$ decay is one of the best probes for new physics effects and it is complementary to direct searches for models like non Minimal Flavour Violation[69][31][29]. This decay is computed very precisely also within these new physics models: even a deviations of 20% from the SM value can be considered as a signal of new physics.

At the present time the most accurate measurement (1.3) of this decay was obtained by the E787 experiment and its upgrade E949 at BNL (from 1995 to

2002) which collected seven events [22].

$$BR(K^+ \to \pi^+ \nu\overline{\nu})(E787 + E949) = 17.3^{+11.5}_{-10.5} \times 10^{-11} \tag{1.3}$$

This result shows the present large gap between the theoretical precision and the experimental error. NA62 wants to improve the measurement of this decay Branching Ratio reaching a precision of 10%, by collecting about 100 events in three years of data taking. $10^{13} K^+$ decays are required, assuming a signal acceptance of the 10% and a branching ratio of the order of 10^{-10} and the rejection factor for other kaon decays shall be about 10^{12}. The possibility to measure trigger efficiencies and background suppression factors directly from data will allow to control other systematic uncertainties.

1.2 The CKM matrix

The Cabibbo-Kobayashi-Maskawa (CKM) matrix [43][72] describes the quark flavour-mixing in the Standard Model weak decays connecting the quark flavour eigenstates (d, s, b) to the weak interaction eigenstates (d', s', b') which interact with the u, c, t quarks flavour eigenstates.

$$\begin{pmatrix} d' \\ s' \\ b' \end{pmatrix} = \begin{pmatrix} V_{ud} & V_{us} & V_{ub} \\ V_{cd} & V_{cs} & V_{cb} \\ V_{td} & V_{ts} & V_{tb} \end{pmatrix} \begin{pmatrix} d \\ s \\ b \end{pmatrix}$$

Quark mixing only appears between negatively charged quarks and not between the positively charged ones for historical reasons: when Cabibbo suggested this mechanism only the u, d and s quarks had been discovered.

The CKM matrix is a generalisation of the 2 x 2 Cabibbo matrix to include three quark families, it is an unitary 3 x 3 matrix that can be expressed through the Wolfenstein parametrisation[92]

$$V = \begin{pmatrix} 1 - \lambda^2/2 & \lambda & A\lambda^3(\rho - i\eta) \\ -\lambda & 1 - \lambda^2/2 & A\lambda^2 \\ A\lambda^3(1 - \rho - i\eta) & -A\lambda^2 & 1 \end{pmatrix} + O(\lambda^4)$$

The 4 real matrix parameters are:

$$\lambda = \sin\theta_{12}, \qquad A\lambda^2 = \sin\theta_{23}, \qquad A\lambda^3(\rho - i\eta) = \sin\theta_{13} e^{-i\phi}$$

where θ_{ij} are three real Cabibbo-like angles expressing a rotation and ϕ is a phase factor that encodes the CP violation in the SM. Shown below are the current experimental values of the nine CKM elements obtained by combining the results of different measurements. The elements of the two u- and c-quark columns ($|V_{ud}|$, $|V_{us}|$, $|V_{ub}|$, $|V_{cd}|$, $|V_{cs}|$ and $|V_{cb}|$) are extracted from measurements of the leptonic ($q_1\bar{q}_2 \to l\nu$) and semileptonic ($q_1 \to q_2 l\nu$) decays of the π, K, D and B mesons and from measurements of their masses and lifetimes. The t-quark column elements ($|V_{td}|$, $|V_{ts}|$ and $|V_{tb}|$) cannot be obtained from leptonic or semileptonic decays because the top quark mass is above the Wb threshold and the process

$t \to Wb$ occurs before top hadronisation. The element $|V_{tb}|$ is therefore obtained from the measurement of the t-quark production cross-sections ($\sigma(p\bar{p} \to t\bar{b})$ and $\sigma(pp \to tb)$). The same processes for d- and s-quark are instead suppressed by at least a factor 10^3: in this way no tree-level processes are suitable to determinate $|V_{td}|$ and $|V_{ts}|$, requiring the study of loop-mediated processes such rare K and B decays and $B-\bar{B}$ oscillations for their determinations. The current measurements of these two parameters are obtained by CDF[2] and LHCb[1] experiments from the mass difference of the mass eigenstates B_L and B_H mesons. The branching ratio of the $K^+ \to \pi^+\nu\overline{\nu}$ (main goal of the NA62 experiment) will give a clean and independent measurement of $|V_{td}V_{ts}^*|$.

$$\begin{pmatrix} |V_{ud}| = 0.97425 \pm 0.00022 & |V_{us}| = 0.2252 \pm 0.0009 & |V_{ub}| = (4.15 \pm 0.49) \times 10^{-3} \\ |V_{cd}| = 0.230 \pm 0.011 & |V_{cs}| = 1.006 \pm 0.023 & |V_{cb}| = (40.9 \pm 1.1) \times 10^{-3} \\ |V_{td}| = (8.4 \pm 0.6) \times 10^{-3} & |V_{ts}| = (42.9 \pm 2.6) \times 10^{-3} & |V_{tb}| = 0.89 \pm 0.07 \end{pmatrix}$$

1.3 The unitary triangles

The CKM matrix unitarity leads to nine conditions on its elements: one for each element of the $V^\dagger V$ matrix. Shown below is one of the combinations conditions

$$V_{ud}V_{ub}^* + V_{cd}V_{cb}^* + V_{td}V_{tb}^* = 0$$

that can be represented graphically in the complex plane as a triangle made of three vectors (see figure 1.1): each one corresponding to one term of the relation.

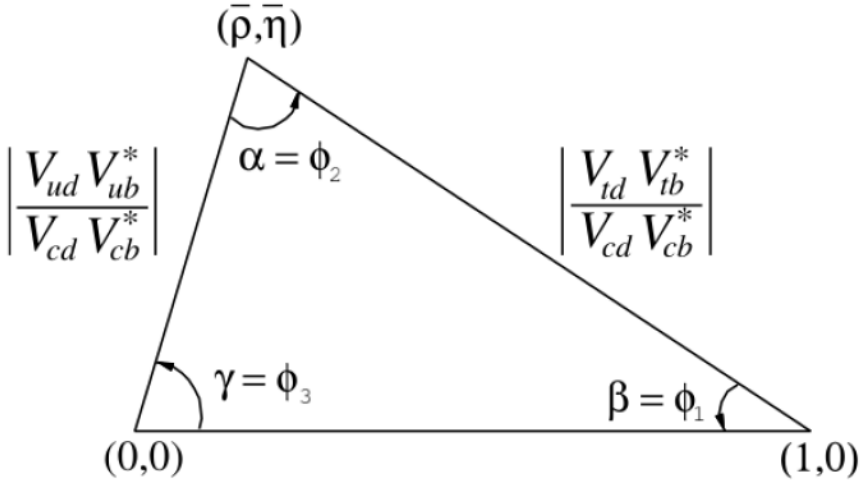

Figure 1.1: Unitarity triangle.

The angles and the side lengths of the triangle are physical observables. So the previous relation (like the others) combination can be tested experimentally to verify the matrix unitarity and therefore to test the SM. For the chosen relation the vertexes of the triangle are (0,0), (1,0), $(\bar{\rho}, \bar{\eta})$ with

$$\bar{\rho} = \rho\left(1 - \frac{\lambda^2}{2}\right), \qquad \bar{\eta} = \eta\left(1 - \frac{\lambda^2}{2}\right).$$

The angles are given by the following relations:

$$\beta = \arg\left(-\frac{V_{cd}V_{cb}^*}{V_{td}V_{tb}^*}\right), \qquad \alpha = \arg\left(-\frac{V_{td}V_{tb}^*}{V_{ud}V_{ub}^*}\right), \qquad \gamma = \arg\left(-\frac{V_{ud}V_{ub}^*}{V_{cd}V_{cb}^*}\right).$$

Measurement of CP asymmetries in B_d decay (like $B_d \to J/\Psi K_s$ and $B_d \to \pi\pi$) allow to obtain the values $\sin 2\beta$ and $\sin 2\alpha$. In the next sections we will see that the $K \to \pi\nu\overline{\nu}$ processes offers a complementary and independent tool to test the above relation in the SM.

1.4 The $K^+ \to \pi^+\nu\overline{\nu}$ branching ratio

Before discussing with the theoretical computation of the branching ratio, it is useful to define the decay width for a decay $X \to Y$:

$$\Gamma(X \to Y) \stackrel{def}{=} \frac{1}{2m_X}\int |A(X \to Y)|^2 d\Phi(Y)$$

where $A(X \to Y)$ is a matrix element that describes the dynamics of the process $X \to Y$ and is called decay amplitude, $\Phi(Y)$ is the final state phase space and m_X is the mass of the decaying particle X.

The branching ratio of the decay $X \to Y$ is the ratio between that process decay width and the sum of all the decay widths of all possible decays of particle X:

$$B(X \to Y) \stackrel{def}{=} \frac{\Gamma(X \to Y)}{\sum_n \Gamma(X \to Y_n)}$$

If there are different final states that are experimentally indistinguishable, the branching ratio is obtained as by the sum of these branching ratios. This is the case for the $K^+ \to \pi^+\nu\overline{\nu}$ decay, because the three neutrino flavours are indistinguishable in our experiment, so the branching ratio is given by the formula:

$$B(K^+ \to \pi^+\nu\overline{\nu}) = \sum_{l=e,\mu,\tau} \frac{1}{2m_K\Gamma_{tot}}\int |A_l|^2 d\Phi(\pi^+\nu_l\overline{\nu}_l)$$

where $A_l \equiv A(K^+ \to \pi^+\nu\overline{\nu})$ and $\Gamma_{tot} \equiv \sum_n \Gamma(X \to Y_n)$. The main contribution to the amplitude A_l in the SM derives from the flavour changing quark transition $s \to d\nu\overline{\nu}$ described by three one-loop Feynman diagrams, the Z-penguins and the W-box (see figure 1.2).

The effective Hamiltonian for this contribution can be written in the SM as [69]:

$$H_{eff}^{SM} = \frac{G_F}{\sqrt{2}}\frac{\alpha}{2\pi\sin^2\theta_W}\sum_{l=e,\mu,\tau}(V_{cs}^*V_{cd}X^l + V_{ts}^*V_{td}X(x_t))(\bar{s}d)_{V-A}(\bar{\nu}_l\nu_l)_{V-A} \qquad (1.4)$$

where

- G_F is the Fermi constant,

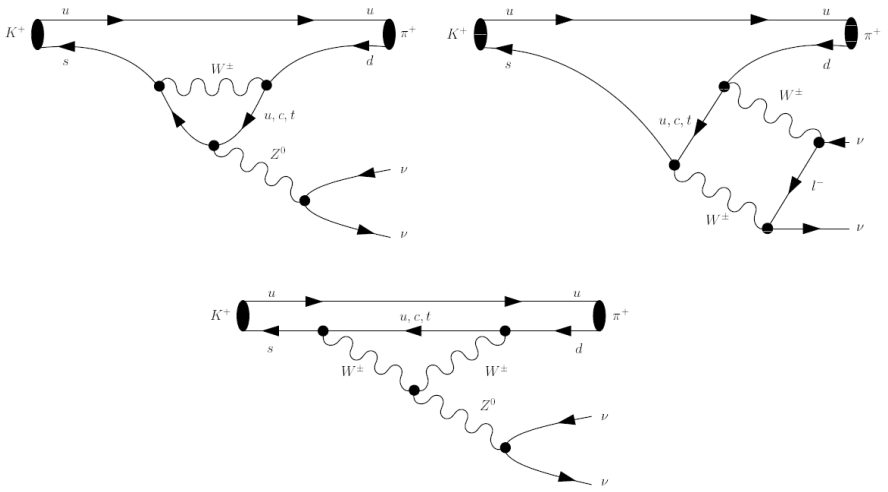

Figure 1.2: The penguin and box diagrams contributing to $K^+ \to \pi^+ \nu\overline{\nu}$.

- α is the electromagnetic coupling constant,
- θ_W is the weak mixing angle,
- X^l are functions describing the contribution of the c-quark to the amplitude A_l (with $l = e, \mu, \tau$),
- $X(x_t)$ is a function describing the contribution of the t-quark, $x_t = m_t^2/M_W^2$ where m_t and M_W are the masses of the top-quark and W boson respectively,
- $(\bar{s}d)_{V-A}$ and $(\bar{\nu}_l\nu_l)_{V-A}$ are the quark and lepton neutral weak currents with vector - axial vector structure.

The u-quark contribution is not present in this formula because it is negligible (the contribution depends on m_u^2/M_W^2). Indeed, because of its mass, the top-quark contribution is dominant and the $s \to d$ transition is described by short-distance quark dynamics.

Starting from the effective Hamiltonian (the amplitude is $A = -iH_{eff}$), the branching ratio can be written as

$$B(K^+ \to \pi^+ \nu\overline{\nu}) = \sum_{l=e,\mu,\tau} \frac{|G_l|^2}{4m_K\Gamma_{tot}} \int |(\bar{s}d)_{V-A}(\bar{\nu}_l\nu_l)_{V-A}|^2 d\Phi(\pi^+\nu_l\overline{\nu}_l)$$

where

$$G_l \stackrel{def}{=} \frac{\alpha G_F}{2\pi \sin^2\theta_W}(V_{cs}^* V_{cd} X^l + V_{ts}^* V_{td} X(x_t))$$

Usually the evaluation of the hadronic matrix element of the FCNC processes limits the precision of the theoretical estimate due to non-perturbative effects. An important property of the $K^+ \to \pi^+ \nu\overline{\nu}$ decay is that the hadronic matrix element can be extracted from the branching ratio of $K^+ \to \pi^0 e^+ \nu$ decay that is well-measured.

$$B(K^+ \to \pi^0 e^+ \nu) = \frac{G_F^2 |V_{us}|^2}{4m_K\Gamma_{tot}} \int |(\bar{s}u)_{V-A}(\bar{\nu}_e e)_{V-A}|^2 d\Phi(\pi^0 e^+ \nu)$$

The $K^+ \to \pi^+ \nu\overline{\nu}$ branching ratio can be written as

$$B(K^+ \to \pi^+ \nu\overline{\nu}) = \sum_{l=e,\mu,\tau} \frac{|G_l|^2}{G_F^2 |V_{us}|^2} 2 r_{K^+} B(K^+ \to \pi^0 e^+ \nu_e)$$

where $r_{K^+} = 0.901 \pm 0.027$ is an isospin breaking corrections[77][30].

Often in literature this expression is written summing over three neutrino flavours as follows [38]

$$B(K^+ \to \pi^+ \nu\overline{\nu}) = k_+ (1+\Delta_{EM}) \left[\left(\frac{Im\lambda_t}{\lambda^5} X(x_t) \right)^2 + \left(\frac{Re\lambda_c}{\lambda} P_c(X) + \frac{Re\lambda_t}{\lambda^5} X(x_t) \right)^2 \right]$$

where

- $k_+ \stackrel{def}{=} r_{K^+} \frac{3\alpha^2 B(K^+ \to \pi^0 e^+ \nu_e)}{2\pi^2 \sin^4 \theta_W} \lambda^8$,
- $\lambda \stackrel{def}{=} |V_{us}|$,
- $\lambda_q = V_{qs}^* V_{qd}$,
- $\Delta_{EM} = -0.15\%$ is a long-distance QED radiative corrections [78],
- $X(x_t)$ is the top-quark contribution,
- $P_c(X)$ is the charm-quark contribution.

If we insert the numerical values of the parameters [84]

$$B(K^+ \to \pi^0 e^+ \nu_e) = (5.07 \pm 0.04)\%, \qquad \alpha = \frac{1}{127.9}, \qquad \sin^2 \theta_W = 0.231,$$

we obtain [69]:

$$k_+ = (5.173 \pm 0.025) \cdot 10^{-11} \left[\frac{\lambda}{0.225} \right]^8.$$

The top-quark contribution can be expanded as

$$X(x_t) = X^0(x_t) + \frac{\alpha_s(m_t)}{4\pi} X^1(x_t) + \frac{\alpha}{4\pi} X^{EW}(x_t)$$

where α_s is the strong coupling constant, $X^0(x_t)$ is the leading-order (LO) contribution[67], $X^1(x_t)$ is the next-to-leading order (NLO) QCD correction[79] and $X^{EW}(x_t)$ is a two-loop electroweak correction[37]. With the recently computed two-loop electroweak correction the value of the top-quark contribution [37] is

$$X(x_t) = 1.469 \pm 0.017 \pm 0.002.$$

The first error corresponds to the uncertainty on the QCD corrections, instead the second error is due to the uncertainty of the electroweak corrections.

The charm-quark contribution $P_c(X)$ is composed of a short-distance and a long-distance part:

$$P_c(X) = P_c^{SD}(X) + \delta P_{c,u}.$$

The short-distance part can be written as

$$P_c^{SD}(X) = \frac{1}{\lambda^4}\left[\frac{2}{3}X^e + \frac{1}{3}X^\tau\right]$$

where X^l are functions describing the contribution of the c-quark already seen in the eq. 1.4. While the distinction of the lepton flavour in the box diagrams is irrelevant in the top contribution due to the large mass of the top-quark ($m_t >> m_l$), it is relevant for the charm contribution because $m_\tau > m_c$. The QCD correction to the short distance charm contribution has been calculated up to the NNLO with a residual uncertainty of $\pm 2.5\%$[39]. After the recent inclusion of QED electroweak corrections[36], the current value of the short-distance contribution [36] is

$$P_c^{SD}(X) = 0.372 \pm 0.015.$$

In [68] we can find a computation of the long distance contributions:

$$\delta P_{c,u} = 0.04 \pm 0.02.$$

Finally the current theoretical prediction for the $K^+ \to \pi^+\nu\overline{\nu}$ branching ratio in the SM is [37].

$$B(K^+ \to \pi^+\nu\overline{\nu}) = (7.81^{+0.80}_{-0.71} \pm 0.29) \times 10^{-11}.$$

The first error is due to uncertainties of the input parameters: V_{cb} (56%), $\bar{\rho}$ (21%), m_c (8%), m_t (6%), $\bar{\eta}$ (4%), α_s (3%), $\sin^2\theta_W$ (1%), etc. The second error is due to the remaining intrinsic theoretical uncertainties: $\delta P_{c,u}$ (46%), $X(x_t)(QCD)$ (24%), P_c (20%), k_+ (7%), $X(x_t)(EW)$ (3%), etc.

In a similar way the branching ratio of the neutral partner decay $K_L \to \pi^0\nu\overline{\nu}$ is computed to be [37]

$$B(K_L \to \pi^0\nu\overline{\nu}) = (2.43^{+0.40}_{-0.37} \pm 0.06) \times 10^{-11}.$$

1.5 $K^+ \to \pi^+\nu\overline{\nu}$ and the unitarity triangle

The previous equations is computed the dependence of the $K^+ \to \pi^+\nu\overline{\nu}$ branching ratio on the CKM matrix elements ($V_{cs}^*V_{cd}$ and $V_{ts}^*V_{td}$). Expressing them in the Wolfenstein parametrisation

$$Re\lambda_c = Re[V_{cs}^*V_{cd}] = -\lambda + \frac{\lambda^3}{2} + \frac{\lambda^5}{8} + A^2\lambda^5(1-\bar{\rho}) + O(\lambda^7),$$

$$Re\lambda_t = Re[V_{ts}^*V_{td}] = -A^2\lambda^5(1-\bar{\rho}) + O(\lambda^7),$$

$$Im\lambda_t = Im[V_{ts}^*V_{td}] = -A^2\lambda^5\bar{\eta} + O(\lambda^7),$$

we obtain

$$B(K^+ \to \pi^+\nu\overline{\nu}) = k_+(1+\Delta_{EM})X^2(x_t)A^4[\bar{\eta}^2 + (\rho_0 - \bar{\rho})^2],$$

where

$$\rho_0 \stackrel{def}{=} 1 + \frac{P_c(X)}{A^2 X(x_t)}.$$

In a similar way the branching ratio of the neutral process $K_L \to \pi^0 \nu\overline{\nu}$ can be written as:

$$B(K_L \to \pi^0 \nu\overline{\nu}) = k_L X^2(x_t) A^4 \bar{\eta}^2$$

where k_L is a parameter (like k_+) that allows to extract the hadronic matrix element from the branching ratio of the $K^L \to \pi^{\pm} e^{\mp} \nu_e$ decay.

Observing the equations, we can notice that branching ratio of the neutral decay $K_L \to \pi^0 \nu\overline{\nu}$ determines the height of the Unitarity triangle, being directly related to the parameter $\bar{\eta}$ (see figure 1.3). The $K^+ \to \pi^+ \nu\overline{\nu}$ branching ratio is instead proportional to the square of the hypotenuse of the right-angled triangle having as other sides the height $\bar{\eta}$ of the Unitarity triangle and the length $\rho_c = \rho_0 - \bar{\rho}$.

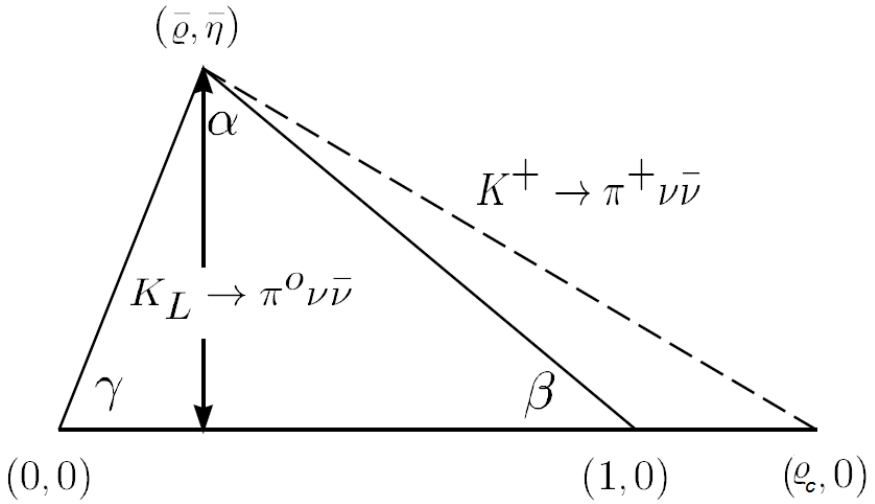

Figure 1.3: Unitarity triangle related to the unitary condition $V_{ud}V_{ub}^* + V_{cd}V_{cb}^* + V_{td}V_{tb}^* = 0$ and to the branching ratios of $K^+ \to \pi^+ \nu\overline{\nu}$ and $K_L \to \pi^0 \nu\overline{\nu}$ decays.

The measurement of both the $K \to \pi\nu\overline{\nu}$ Branching Ratios allows to eliminate the considerable uncertainty due to the $|V_{ub}/V_{cb}|$ parameter and gives to a more complete determination of the unitarity triangle, obtaining a clean measurement of the β and γ angles independent from b-decay measurement.

This shows how the $K^+ \to \pi^+ \nu\overline{\nu}$ process (with its neutral partner) can be used for an independent and complementary test of the Standard Model consistency.

1.6 Beyond the standard model

In SM extensions the effective Hamiltonian becomes generally much more complex: indeed new complex phases, new one-loop short distance functions and generally new flavour-violating couplings can be present.

The effective Hamiltonian for the $K \to \pi\nu\overline{\nu}$ processes in almost all the SM extensions is simply equal to the SM one but replacing $X(x_t)$ with $|X|e^{i\theta_X}$ [41].

The new physics modifies the magnitude of the $X(x_t)$ function and introduce a new complex phase θ_X.

Minimal Flavour Violation (MFV) models are the simplest extensions of the SM: in those models $\theta_X = 0$ or π and $|X|$ is only modified by loop diagrams with new particles exchanges [40]. The correlations between $K \to \pi\nu\overline{\nu}$ and other K and B processes remains valid in the MFV: so the bounds on rare B decays do not allow a large departure of $K \to \pi\nu\overline{\nu}$ from the SM in this model.

It is possible to obtain larger deviations from the Standard Model in other models like the Minimal Supersymmetric extension of the Standard Model (MSSM) [69], Littlest Higgs model with T-parity (LHT) [31], the Randall-Sundrum model with custodial protection [32] and the Standard Model with a sequential fourth generation [42].

Figure 1.4 shows the correlation between the branching ratios of $K^+ \to \pi^+\nu\overline{\nu}$ and $K_L \to \pi^0\nu\overline{\nu}$ in MVF and other new physics models [89].

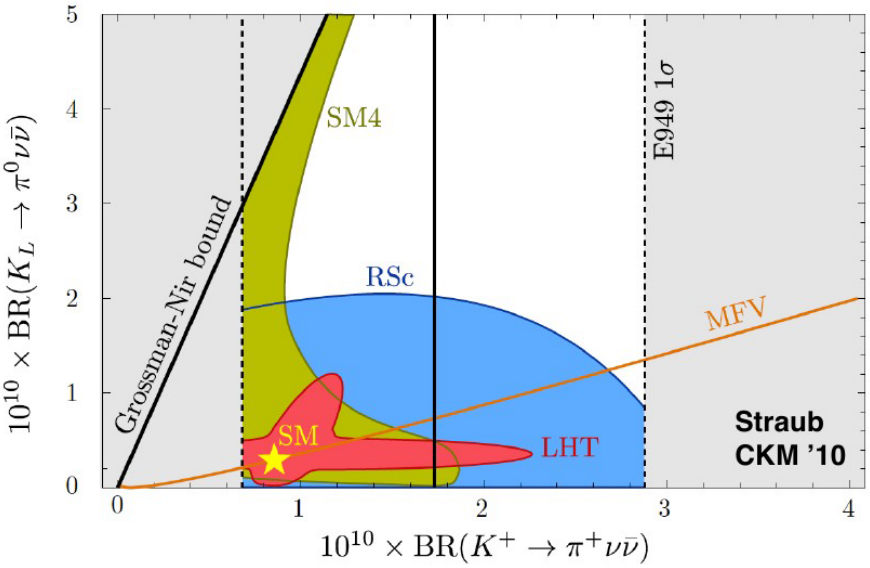

Figure 1.4: Correlation between the branching ratios of $K^+ \to \pi^+\nu\overline{\nu}$ and $K_L \to \pi^0\nu\overline{\nu}$ in new physics models [89]. The Grossman-Nir bound arises from the fact that the imaginary part of a complex number has to be smaller than or equal to its absolute value, corrected by the lifetime differences and isospin breaking effects [62].

1.7 Experimental status

The interest for the $K^+ \to \pi^+\nu\overline{\nu}$ decay started in 1969 with experiments that used stopped-kaon beams.

The first experimental search used a heavy-liquid bubble chamber at the Argonne Zero Gradient Synchrotron [45], and obtained an upper limit to the branching ratio of 10^{-4} at 90% confidence level (CL).

At the Berkeley Bevatron in 1973 a spark chamber experiment reduced the limit down to 5.6×10^{-7} [44].

This limit was further improved to $B(K^+ \to \pi^+\nu\overline{\nu}) < 1.4 \times 10^{-7}$ in 1981 at the KEK Proton Synchrotron [23].

To obtain the first observation of the decay we have to wait for 1997 [3] and the experiment E787 at Brookhaven National Laboratory (BNL). The combination of its measurement with the one of its upgraded version, E949, gives the best measurement currently available [21]. E787 and E949 studied the process by using decays from kaons at rest.

The signature of the $K^+ \to \pi^+\nu\overline{\nu}$ decay was a pion of momentum P $<$ 227 MeV/c without other particles. This required a strong backgrounds suppression and a reliable estimate of residual background. The main background sources are $K^+ \to \mu^+\nu_\mu$ (64% branching ratio), $K^+ \to \pi^+\pi^0$ (21% branching ratio), the beam pions scattering processes and K^+ charge exchange processes resulting in decays of the K_L.

In the E787 experiment the kaons were produced with a momentum between 710 MeV/c and 790 MeV/c depending on the runs and with a rate of 7×10^6 per spill of 1.6 s.

A central drift chamber, a plastic scintillator cylindrical range stack, a double-layer straw chambers and a magnetic field were used to measure the momentum (P), range (R) and kinetic energy (E) of charged decay products. Pions were distinguished from muons by kinematics and by identifying the pion decays (to muons and electrons) in the range stack.

A CsI Endcap Photon Detector [48] was used to detect the photons produced by π^0 decays allowing to suppress $K^+ \to \pi^+\pi^0$ background events; the inefficiency for photon energies above 1 MeV was 10^{-6}.

The signal was selected by looking for an identified kaon stopping in the target together with a single charged particle track unaccompanied by other decay products. That charged particle should be identified as a π^+ using the measured values of momentum, range, energy together with the observation of the decay sequence $\pi \to \mu \to e$ that provided further rejection against $K^+ \to \mu^+\nu_\mu$ events.

Residual backgrounds could be due to mis-identified scattered beam pions and charge exchange processes (if K_L were produced at low enough energy to remain in the target for the required time and if the charged lepton decay products were unobserved).

The momentum spectrum of the $K^+ \to \pi^+\nu\overline{\nu}$ decay was divided in two signal regions on both sides of the π^+ momentum of the $K^+ \to \pi^+\pi^0$ decay (see figure 1.5).

The E787 experiment observed 2 events in region 1 (pion momentum between 211 MeV/c and 229 MeV/c) with an estimated background of 0.15 ± 0.05. This observation leads to $B(K^+ \to \pi^+\nu\overline{\nu}) = 1.57^{+1.75}_{-0.82} \times 10^{-10}$ obtained from a total sample of 5.9×10^{12} stopped kaons[5]. In region 2 (pion momentum 140 MeV/c $<$ P $<$ 195 MeV/c) one candidate event was found, consistent with the background estimate of 0.73 ± 0.18. The upper limit obtained in this region was $B(K^+ \to \pi^+\nu\overline{\nu}) < 4.2 \times 10^{-9}$ (90% confidence level) consistent with the measurement in the other region[4].

The experiment E949 [21] was an upgrade of E787 studied to increase the sensitivity of a factor 5. They upgraded the photon veto calorimeter, replaced one third of the Range Stack and improved the trigger system and data analysis,

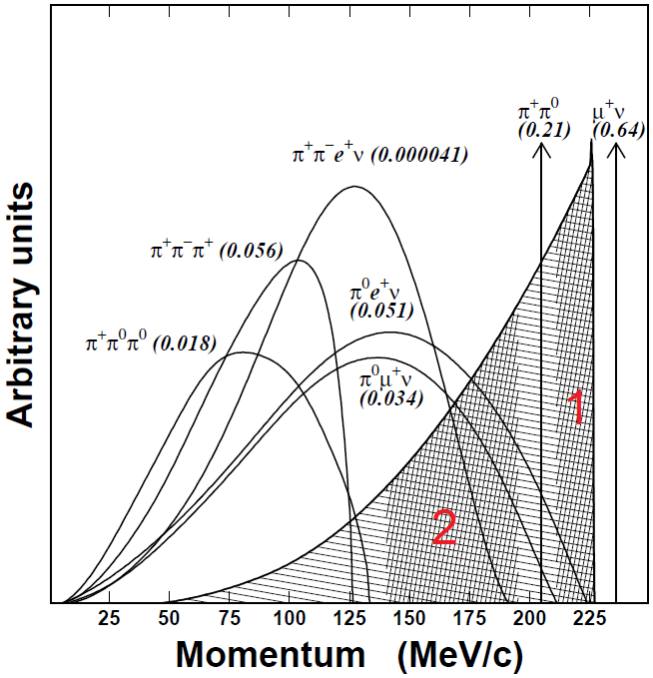

Figure 1.5: Expected momentum spectra of charged particles from K^+ decays in the rest frame. The values in parentheses represent the Branching Ratios of the corrisponding decay modes. The hatched area represents the π^+ spectrum from $K^+ \to \pi^+\nu\overline{\nu}$ decay. The densely hatched regions are the signal regions 1 and 2.

achieving a comparable acceptance even at twice the rate of E787. Figure 1.6 shows the E949 detector layout.

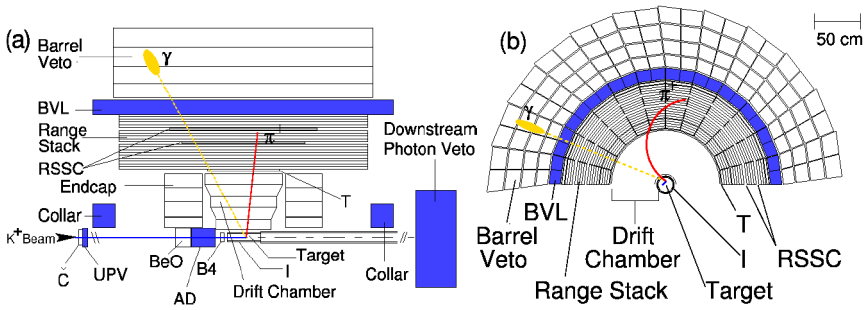

Figure 1.6: Schematic layout of the E949 apparatus: side (a) and front (b) views.

As for E787, E949 performed the data analysis diving the kinematic regions in 2 parts. E949 observed one event in region 1 over an expected background of 0.30 ± 0.03 and a stopped kaon sample of 1.8×10^{12}. Combining the data of the two experiments (E787 and E949) a branching ratio of $B(K^+ \to \pi^+\nu\overline{\nu}) = 1.47^{+1.30}_{-0.89} \times 10^{-10}$ was obtained in the region 1 [19]. Three events were instead observed in the region 2 from a sample of 1.71×10^{12} stopped kaons and with an estimated total background of $0.93 \pm 0.17(stat.)^{+0.32}_{-0.24}(syst.)$ events. This observation led to a branching ratio of $B(K^+ \to \pi^+\nu\overline{\nu}) = 7.89^{+9.26}_{-5.10} \times 10^{-10}$[21].

The combined final measurement[22] of the two experiments is based on 7 observed candidate $K^+ \to \pi^+\nu\overline{\nu}$ events (see figure 1.7) and the resulting branching

ratio is $B(K^+ \to \pi^+\nu\overline{\nu}) = 1.739^{+1.15}_{-1.05} \times 10^{-10}$. This measurement is within one standard deviation from the SM prediction.

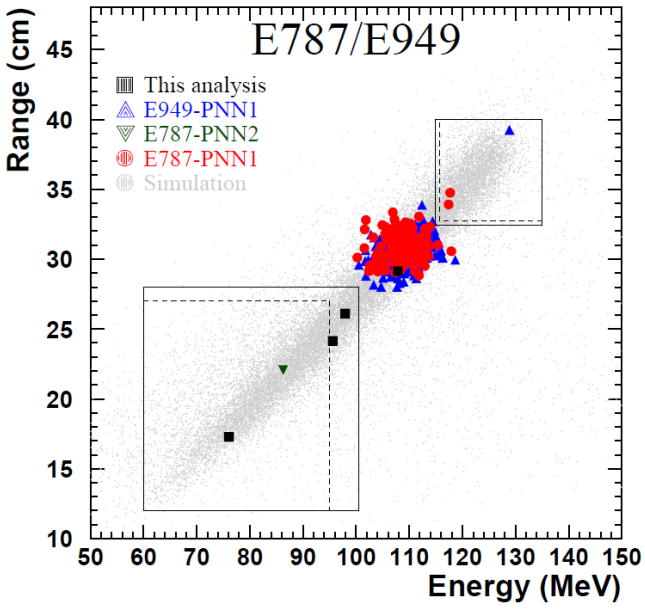

Figure 1.7: The kinetic energy and range of the 7 $K^+ \to \pi^+\nu\overline{\nu}$ candidates, observed in the E787+E949 experiments. The two signal regions are delimited by solid lines, the dashes lines show the Signal Regions of earlier analyses. The grey points are obtained by a MC simulation of the signal. The cluster of events between the two Signal Regions is due to $K^+ \to \pi^+\pi^0$ events with an undetected π^0.

Figure 1.8 shows a summary of all the experimental limits and measurements of the Branching Ratio of the $K^+ \to \pi^+\nu\overline{\nu}$ decays.

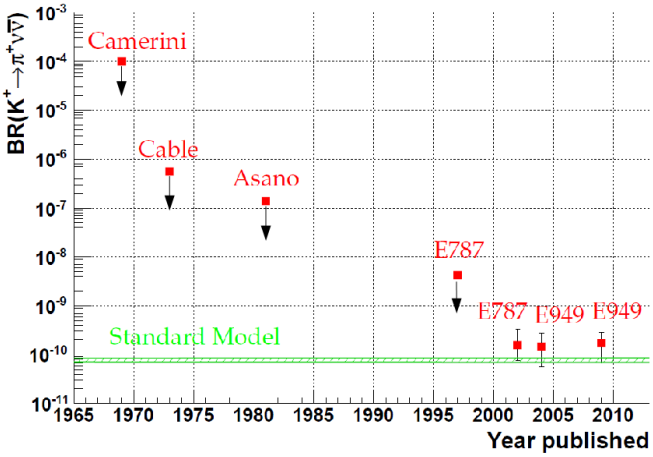

Figure 1.8: Summary of experimental measurements and upper limits (squares with no errors) at 90% confidence level for the $K^+ \to \pi^+\nu\overline{\nu}$ branching ratio shown along a time line indicating the year of publication [45][44][23][3][21].

1.8 NA62 experimental strategy

Unlike previous experiments, NA62 uses a decay-in-flight technique to measure the branching ratio of the $K^+ \to \pi^+\nu\overline{\nu}$ decays. The experiment uses a primary 400 GeV/c proton beam extracted from the SPS CERN and steered to a Beryllium target to generate a secondary beam of kaons, pions and protons, with a momentum of 75 GeV/c, selected in a beam line long 100 m.

There are two principal advantages to use a high energy beam:

1. the K^+ production cross section increases with the proton energy so we have a greater K^+ flux with the same proton flux;

2. the detection of photons from background decays is easier at high energy. NA62 will study the kinematic region where the laboratory π^+ momentum is lower than 35 GeV/c; so the photons, from the dominant background decay $K^+ \to \pi^+\pi^0$, have at least 40 GeV of energy to be detect by veto detectors.

The high energy beam has also some disadvantage: protons and pions can't be separated efficiently from kaons of the secondary beam, so the upstream detectors, that measure K^+ direction and momentum, are exposed to a seventeen times larger flux than the kaon flux alone. In fact the total beam rate at the end of the beam line is of the order of 750 MHz but kaons are only about 6% of the flux. Downstream detectors should not be interested by this large flux because the undecayed particles remain inside the beam pipe; the integrated rate over these detectors is of the order of 13 MHz. Upstream detectors as the GTK (see section 2.2.2) were developed to cope with this very high beam rate.

The downstream detectors start about 100 m after the Beryllium target and are distributed along 170 m; the fiducial region for decays extends from 105 m to 165 m after the target. Detectors have an approximate azimuthal symmetry around the beam axis, with an inner hole to let the high flux of undecayed particles pass through without hitting the downstream detectors. In the next chapter, a detailed description of the experimental setup is presented.

To reach its goal, the NA62 experiment needs to collect at least 10^{13} K^+ decays, corresponding to about 100 $K^+ \to \pi^+\nu\overline{\nu}$ events assuming a signal acceptance of 10% and the SM Branching Ratio (eq. 1.1). For this purpose a rejection factor of the order of 10^{12} is required for the common kaon decay modes, to keep the systematic uncertainty small enough to measure the $\pi^+\nu\overline{\nu}$ Branching Ratio with a precision of 10%.

The $K^+ \to \pi^+\nu\overline{\nu}$ signature is one track in the final state matching in time with one K^+ track upstream the decay region and nothing else, because the two neutrinos are undetectable. Backgrounds can originate from all the kaon decays that result in a single detected charged track with no other particles, or from beam particles interacting with detectors or residual gas, if they accidentally match in time an incoming kaon. Kaon decays with more charged particles can mimic the signal if there are undetected tracks due to detectors inefficiencies or acceptances. In particular the rejection of the most frequent decays, with Branching Ratio 10^{10} times that of the signal, is crucial: for example

$$B(K^+ \to \pi^+\pi^0) = (20.66 \pm 0.08)\%,$$
$$B(K^+ \to \mu^+\nu_\mu) = (63.55 \pm 0.11)\%.$$

The detector design focused on four main requirements to minimize the background: an accurate kinematic reconstruction, a precise time measurement, an efficient veto system and particle identification system.

Kinematic reconstruction, together with particle identification, is a useful rejection technique for some decays when π^0 photons of $K^+ \to \pi^+\pi^0$ decay aren't detected or when the μ of $K^+ \to \mu^+\nu_\mu$ is mistaken for a π^+.

Figure 1.9 shows the $K^+ \to \pi^+\nu\overline{\nu}$ decay kinematics: only the K^+ momentum $\overrightarrow{P}_K$ and the π^+ momentum $\overrightarrow{P}_\pi$ can be measured.

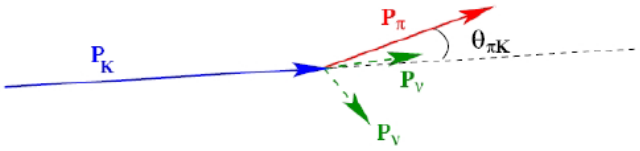

Figure 1.9: $K^+ \to \pi^+\nu\overline{\nu}$ kinematics.

The kinematics of the decay can be described by the variable $m^{2(\pi)}_{miss}$ defined as the square of the difference between the kaon candidate 4-momentum and the pion candidate 4-momentum. In the computation, the detected particles are supposed to be a K^+ and a π^+.

$$m^{2(\pi)}_{miss} \stackrel{def}{=} (P_K - P_\pi)^2 = m_K^2 + m_\pi^2 - 2E_K E_\pi + 2|\overrightarrow{P}_K||\overrightarrow{P}_\pi|\cos\theta_{\pi K}$$

Where $\theta_{\pi K}$ is the angle between the K^+ momentum and the π^+ momentum, $E_K = \sqrt{|\overrightarrow{P}_K|^2 + m_K^2}$ and $E_\pi = \sqrt{|\overrightarrow{P}_\pi|^2 + m_\pi^2}$.

The missing mass has different distributions for the signal and the main K^+ decays:

- $K^+ \to \pi^+\nu\overline{\nu}$ is a three-body decay so it has a continuous distribution in $m^{2(\pi)}_{miss}$. We have that $m^{2(\pi)}_{miss} = (P_\nu + P_{\bar{\nu}})^2$ because $P_K = P_\pi + P_\nu + P_{\bar{\nu}}$ and $m^{2(\pi)}_{miss} = (P_K - P_\pi)^2$. The lower value of the distribution is reached when the two neutrinos have the same momentum, so that $m^{2(\pi)}_{miss} = (m_\nu + m_{\bar{\nu}})^2 \approx 0$. The maximum value is obtained when the π^+ is at rest in he kaon rest frame: $P_K = (m_K, \overrightarrow{0})$, $P_\pi = (m_\pi, \overrightarrow{0})$ and $m^{2(\pi)}_{miss} = (m_K - m_\pi)^2$.

- $K^+ \to \pi^+\pi^0$ is a two-body decay so from the relation $P_K = P_{\pi^+} + P_{\pi^0}$ follows that the result is a peak at $m^{2(\pi)}_{miss} = m^2_{\pi^0}$.

- Even the decay $K^+ \to \mu^+\nu$ is a two-body decay but the pion candidate is actually a muon: the muon energy E_μ is wrongly estimated assuming the pion mass, and the result is that the $m^{2(\pi)}_{miss}$ is always negative and 0 is the upper limit.

- $K^+ \to \pi^+\pi^+\pi^-$ is a three-body decay so it has a continuous distribution in $m^{2(\pi)}_{miss} = (P_{\pi^+} + P_{\pi^-})^2$. It is analogous to the $K^+ \to \pi^+\nu\overline{\nu}$ decay so the minimum value is $m^{2(\pi)}_{miss} = 4m^2_\pi$ and the maximum is $(m_K - m_\pi)^2$ (same as the signal).

The distribution of the $m^{2(\pi)}_{miss}$ for the signal and the main decay modes led to define two signal regions where the main backgrounds should be limited by the kinematic constrains (see figure 1.10):

- **Region I**: $0 < m^{2(\pi)}_{miss} < m^2_{\pi^0} - (\Delta m)^2$
- **Region II**: $m^2_{\pi^0} + (\Delta m)^2 < m^{2(\pi)}_{miss} < min[m^{2(\pi)}_{miss}(K^+ \to \pi^+\pi^+\pi^-)] - (\Delta m)^2$

where $(\Delta m)^2$ is the resolution on the squared missing mass.

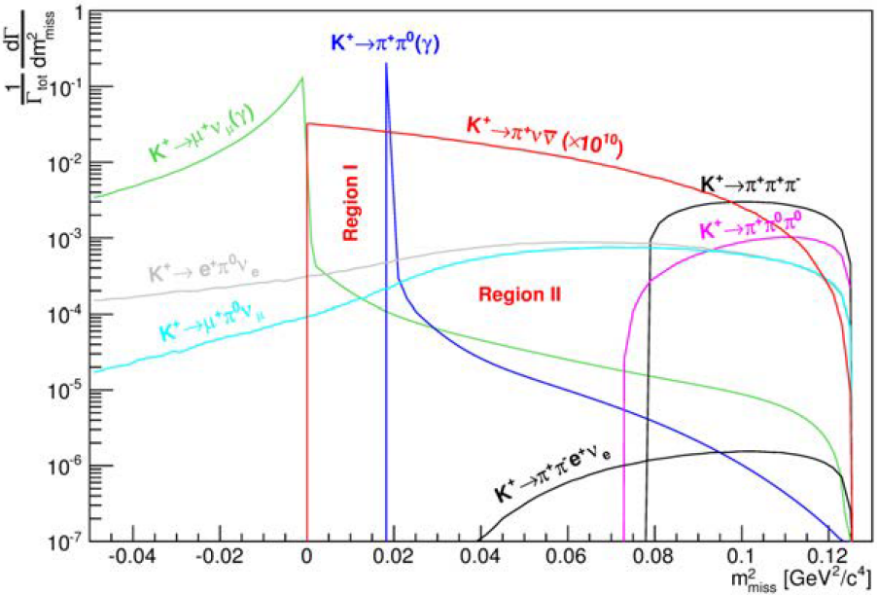

Figure 1.10: $m^{2(\pi)}_{miss}$ distributions for signal and backgrounds from the main K^+ decay modes. The backgrounds are normalized according to their branching fraction; the signal is shown multiplied by a factor 10^{10}.

In this way the $m^{2(\pi)}_{miss}$ variable can be used to reject the main decay modes backgrounds that are the 92% of K^+ decays. However the total background in these regions is several order of magnitude larger then the signal, because of resolution effects on the measured quantities of the main decay modes, radiative tails, semi-leptonic decays and even rare decays (for example $K^+ \to \pi^+\pi^- e^+\nu_e$). The kinematics of these other decays cannot be constrained by the missing mass variable. Moreover other sources of single-track background could be the beam interactions with the material along the beam line and the residual gas in the vacuum region.

8% of the K^+ decay width is due to radiative and semi-leptonic decays that can't be rejected kinematically because they overlap the signal regions in the $m^{2(\pi)}_{miss}$ variable (see figure 1.10); so for these decay modes, particles identification

and veto systems are the only tools to fight the background. To suppress all the decays that can mimic the signal, hermetic detectors are required, especially for photons from π^0 originating in the fiducial region. The detectors system should provide a total angular coverage for angles below to 50 mrad to have an inefficiency on the $\pi^+\pi^0$ rejection below to 10^{-8}.

The first requirement for signal selection is the presence of one track reconstructed in the downstream spectrometer matching in time and space with one track reconstructed in the beam spectrometer. A Čerenkov counter upstream the decay region ensures the presence of a kaon and gives a time to match the tracks in the beam spectrometer with those in the downstream spectrometer. This allows to suppress events due to interactions of the beam with the residual gas in the vacuum region and the material along the beam line. A photon veto system is used to veto decays with photons in the final state. To identify charged pions and to achieve the suppression of the decay modes with muons and positrons, a set of criteria based on detector as the RICH and hadronic calorimeters is established. The same criteria, together with a complete tracks reconstruction in the downstream spectrometer, are useful to reduce backgrounds with more than one charged track in the final state. Finally two requirements are imposed:

- The decay must have the vertex between 105 and 165 m from the target;
- The measured π^+ momentum has to be between 15 GeV/c and 35 GeV/c.

The rejection strategy for some decay modes is described below:

- The $K^+ \to \pi^+\pi^0$ decay is mainly rejected by the kinematic selections of the two signal regions: the tracking system allows a 10^{-3} GeV$^2/c^4$ resolution on $m^{2(\pi)}_{miss}$ that corresponds to a kinematic rejection factor of about 5×10^3. The principal limiting factor to the rejection power is due to the pileup in the beam spectrometer and the non Gaussian tails induced e.g. by multiple scattering. To reach the final rejection factor, photon rejection must provide a π^0 suppression factor of order 10^8. The NA62 photon veto system (including electromagnetic calorimeters) ensures an angular coverage between 0 to 50 mrad for photons with an energy down to 100 MeV. The percentage of $K^+ \to \pi^+\pi^0$ events with one photon out of acceptance at large angle is about 0.2%, but the other photon should be detected because it travels in the forward direction and has an energy above 10 GeV.

- The $m^{2(\pi)}_{miss}$ of the $K^+ \to \mu^+\nu$ decay is negative because of the pion mass hypothesis, and approaches zero at increasing pion momenta. So the $m^{2(\pi)}_{miss}$ cuts allow a strong suppression of this background. The situation is similar to that of $K^+ \to \pi^+\pi^0$ and the kinematics rejection factor is about 1.5×10^4. Additional suppression comes from the pion identification method which uses the information from the RICH detector and calorimeters. The inefficiency of the muon-pion separation is of the order of 10^{-5} and is due to the absorption of muons undergoing Bremsstrahlung energy loss.

- The rejection of $K^+ \to \pi^+\pi^+\pi^-$ events by the one track requirement in the downstream spectrometer is about the 99%. The residual 1% (when

one π^+ and the π^- are not reconstructed in the spectrometer or out of acceptance) is strongly suppressed with the kinematics $m^{2(\pi)}_{miss}$ cut, and the lower momentum cut at 15 GeV/c helps for this goal. The overall rejection factor from kinematics is 1.5×10^6. The only residual background is due to events entering in region II, because of the tails of the reconstructed $m^{2(\pi)}_{miss}$ due to multiple scattering.

The table 1.1 shows a summary of the main kaon decay modes together with the strategy used to reject them.

Decay	Branching Ratio	Rejection strategy
$K^+ \to \mu^+\nu$	63%	μ-ID + kinematics
$K^+ \to \pi^+\pi^0$	21%	γ-veto + kinematics
$K^+ \to \pi^+\pi^+\pi^-$	6%	multi tracks veto + kinematics
$K^+ \to e^+\pi^0\nu_e$	5%	e-ID + γ-veto
$K^+ \to \mu^+\pi^0\nu_\mu$	3%	μ-ID + γ-veto
$K^+ \to \pi^+\pi^0\pi^0$	2%	γ-veto + kinematics

Table 1.1: Main kaon decay modes with their Branching Ratios and rejection strategy.

Chapter 2

NA62 apparatus overview

The NA62 experiment is located at the ECN3 zone in the CERN North Area Intensity Facility (see figure 2.1) and uses the SPS extraction line already used by the NA48 experiment.

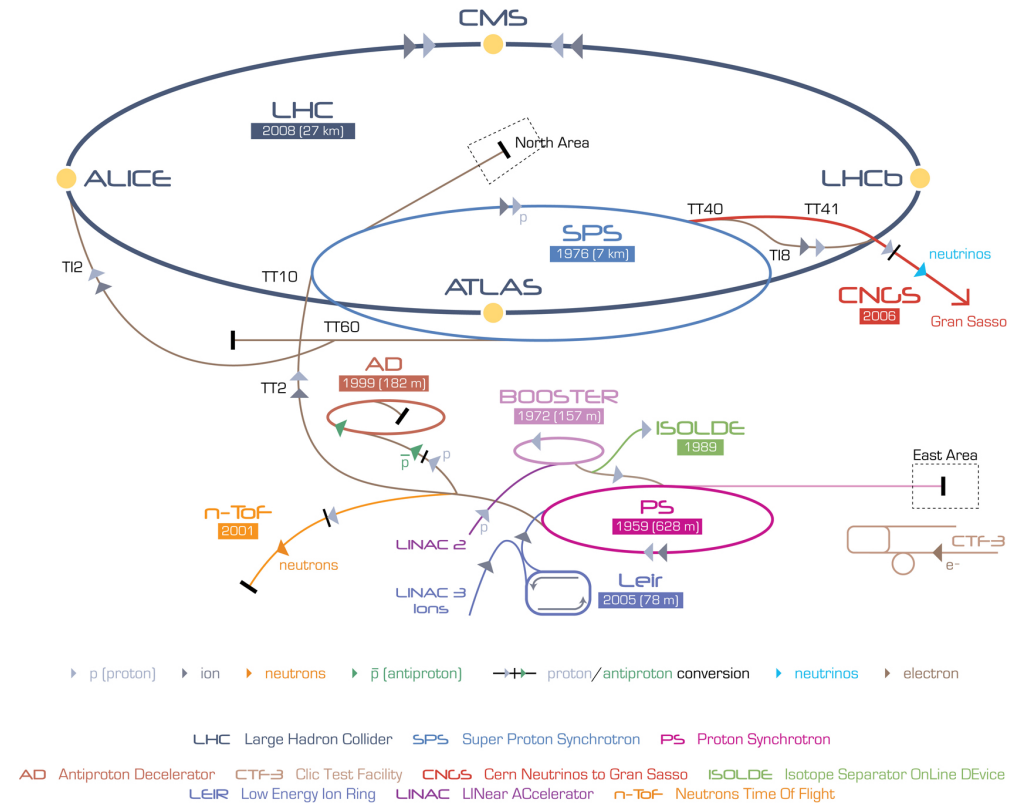

Figure 2.1: Schematic view of the CERN accelerator complex (not to scale). The NA62 experiment is located in the North Area SPS extraction line.

As mentioned in section 1.8 the detectors used to detect the kaon decay products are spread along a 170 m long region starting about 100 m downstream of the target. The fiducial decay region is 60 m long and starts 105 m after the target. The largest detectors have an approximately cylindrical shape around the beam axis with a diameter up to about 2 m and down to 10 cm in order to let the very intense flux of undecayed beam particles pass through without affecting

the active area.

The experimental setup (see figure 2.3) consists in:

- the Kaon TAGger (KTAG) that uses a Čerenkov Differential counter with Achromatic Ring focus (CEDAR) to identify K^+ in the hadron beam;
- the Gigatracker (GTK), a tracking detector for beam particles upstream the decay region and composed of three silicon micro-pixel stations and a set of achromatic magnet;
- the CHarged ANTIcounter (CHANTI) a set of six stations of plastic scintillator detectors useful for vetoing charged particles generated in the last station of the GTK.
- a photon veto system that guarantees an angular coverage from 0 mrad up to 50 mrad through 12 Large Angle Veto (LAV), a Liquid Krypton electromagnetic calorimeter (LKr), an Inner Ring Calorimeter (IRC) to cover the annular region around the beam and a Small Angle Calorimeter (SAC) located at the end of the experimental hall to cover the small angle region;
- the STRAW magnetic spectrometer for charged particles originating in the decay region;
- a Ring Imaging Čerenkov (RICH) to separate π^+ from μ^+ in the momentum region between 15 GeV/c to 35 GeV/c, which can also measure particle direction and velocity;
- the Charged Hodoscope (CHOD), a segmented plastic scintillator detector conceived for triggering purpose.
- a muon veto system composed of three stations.

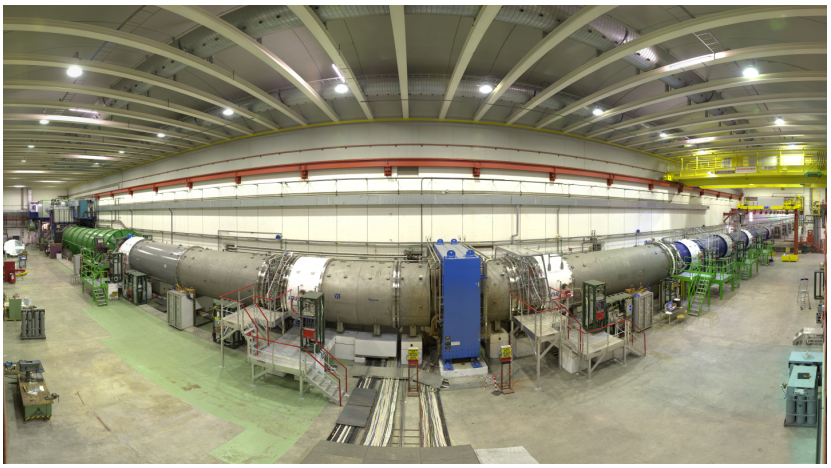

Figure 2.2: Gigapanorama of the NA62 cavern, in which all detectors can be roughly seen.

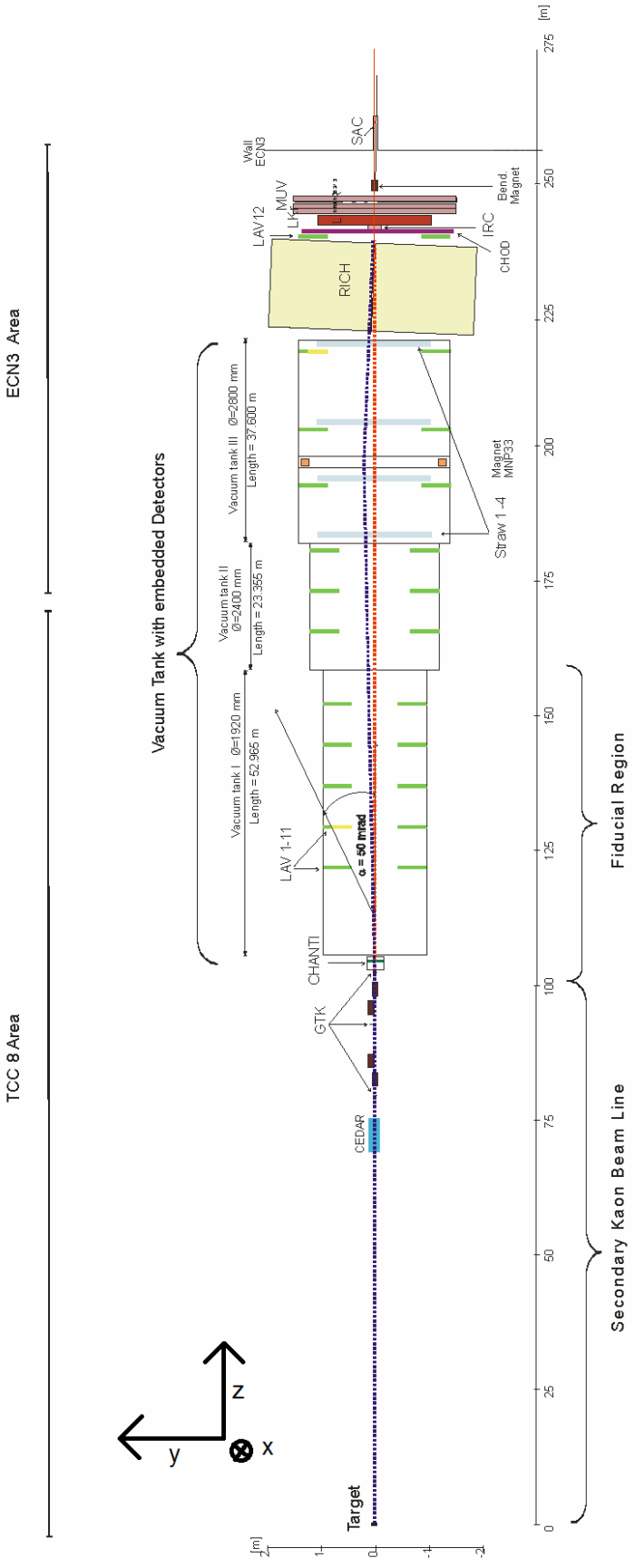

Figure 2.3: Schematic longitudinal view of the NA62 experimental setup.

2.1 The beam line

The NA62 experiment uses a 75 GeV/c secondary hadron beam composed by K^+ (6%), π^+ (71%) and protons (23%) [50]. This secondary beam is produced by steering a 400 GeV/c primary proton beam to the T10 Beryllium target. The primary beam is delivered by the SPS in spills (also called *bursts*) with a 4.5 s flat top and $\sim$ 6 s of period; it is transported via the P42 beam line, focused and directed at zero angle onto the 400 mm long, 2 mm diameter, Beryllium target. The secondary beam is shaped by a collimator, which selects only outgoing particles within an angle of 6 mrad; the beam is focussed by three quadrupole magnets and bent vertically by the first of two front-end achromats, each formed of four dipole magnets. The first two dipoles bend the beam downwards and then upwards, in this way selecting only the particles in a narrow momentum band $\Delta p/p$, centred around 75 GeV/c: particles with a momentum outside the momentum band are deflected by different angles and are dumped by a set of collimators. The selected beam passes through a tungsten radiator (1.3 X_0 thick) making the positrons lose enough energy via Bremsstrahlung radiation to be rejected after a second pair of dipole magnets. The second two dipoles work in a similar way to the first and restore the initial beam trajectory. After the first achromat, another three quadrupole magnets refocus the beam. At this stage the beam has an average momentum of 75 GeV/c, a spread of 0.8 GeV/c (RMS) and is composed only of positively-charged particles. Two pairs of quadrupole magnets are placed before and after the KTAG to optimise the kaon identification: the first pair makes the beam wider and more parallel while the second pair refocuses the beam to make it convergent. Finally, just before the decay region, the beam passes through the second achromat, composed of two pairs of dipole magnets. The three stations of the GTK are placed before, between and after the dipole pairs, to measure the beam momentum. Finally, the beam is bent horizontally by an angle of 1.2 mrad (see figure 2.4) in order to compensate for the deflection induced by the magnet MNP33 used in the STRAW spectrometer downstream the decay region. The beam profile and the beam divergence at the entrance of the decay region are 55.0×22.8 mm^2 ($\pm$ 2 RMS) and 90 μrad respectively[50].

At the end of the experimental hall, the residual beam is deflected by +21.6 mrad by a final dipole magnet and sent to a beam-dump, in order to avoid the SAC calorimeter (which vetoes photons).

A choice of a positive rather than negative beam is motivated by the fact that, at 75 GeV/c, the ratio of production rates $K^+/K^- \sim 2.1$ for 400 GeV/c proton and the ratio $\frac{K^+/\pi^+}{K^-/\pi^-} \sim 1.2$.

2.2 Detectors upstream the decay region

2.2.1 KTAG

The kaon component is about the 6% of the beam, which has a total rate of 750 MHz. Since the separation in flight of the kaon from the other beam particles is not possible at this beam momentum (75 GeV/c), a particle flux 17 times

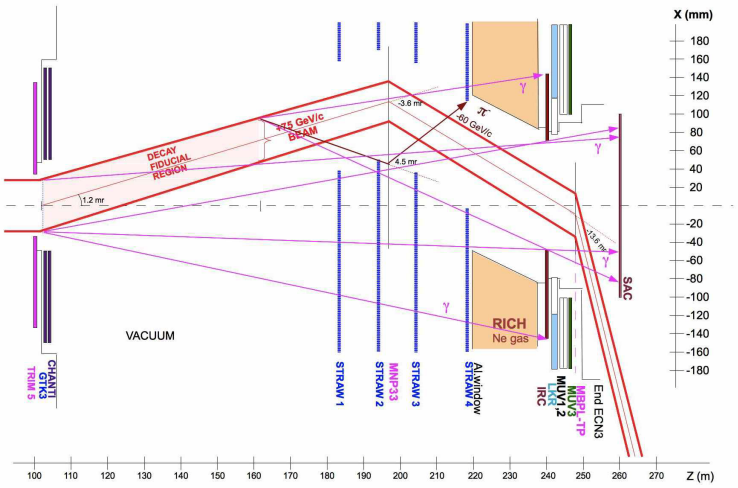

Figure 2.4: Schematic layout of the downstream part of the beam on the horizontal plane.

greater than the kaon one passes through the NA62 detector, interfering with the measurements and generating accidental events. In particular beam pions, interacting with the material upstream of the decay volume (e.g. the GTK3) or with the residual gas in the vacuum tank, may be scattered and misidentified as part of $K^+ \to \pi^+\nu\overline{\nu}$ events: kaon identification is necessary to reduce the beam π^+ contribution to the background.

A detector called Kaon TAGger (KTAG) was built to identify the kaons in the beam and to measure their time with good resolution. The KTAG is a NA62 upgrade of a ChErenkov Differential counter with Achromatic Ring focus (CEDAR) [34][35]. A schematic view of a standard CERN SPS CEDAR is shown in figure 2.5.

The CEDAR is a steel vessel of 55.8 cm external (53.4 cm internal) diameter and 4.5 m length, was used at CERN since the early '80s for SPS secondary beam diagnostics, and is designed to identify particles of a given mass by making the detector blind to the Čerenkov light produced by particles of different masses. The Čerenkov angle of the light, emitted by a charged particle traversing a gas of a given refraction index n, is a function of the gas pressure, the beam momentum and the mass of the particle. The CEDAR is filled with nitrogen gas ($0.03X_0$), whose refractive index n is set by choosing the gas pressure (see figure 2.6), for the kaon mass and the beam momentum (75 GeV/c). The CEDAR could be even filled with hydrogen to minimise material on the beam line, and hence reduce multiple Coulomb scattering.

At the end of the CEDAR vessel, a spherical mirror reflects the Čerenkov light onto a ring-shaped diaphragm of 100 mm radius, located at the vessel entrance. The aperture width of the diaphragm is adjustable to optimize the selection of the kaons. A chromatic corrector lens, designed to match the dispersion curve of the gas, is positioned between the mirror and the diaphragm: it ensures that light of all wavelengths arrives at the same radius on the diaphragm plane. After the

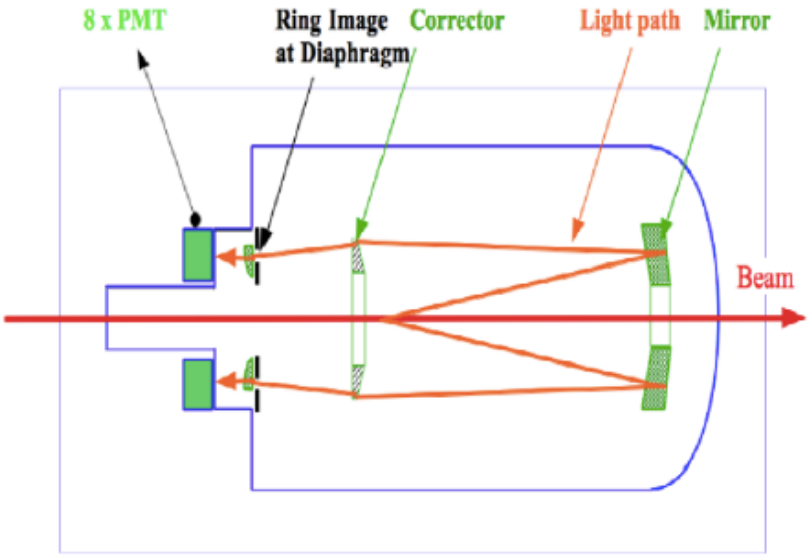

Figure 2.5: Schematic layout of the optical system located inside the CEDAR.

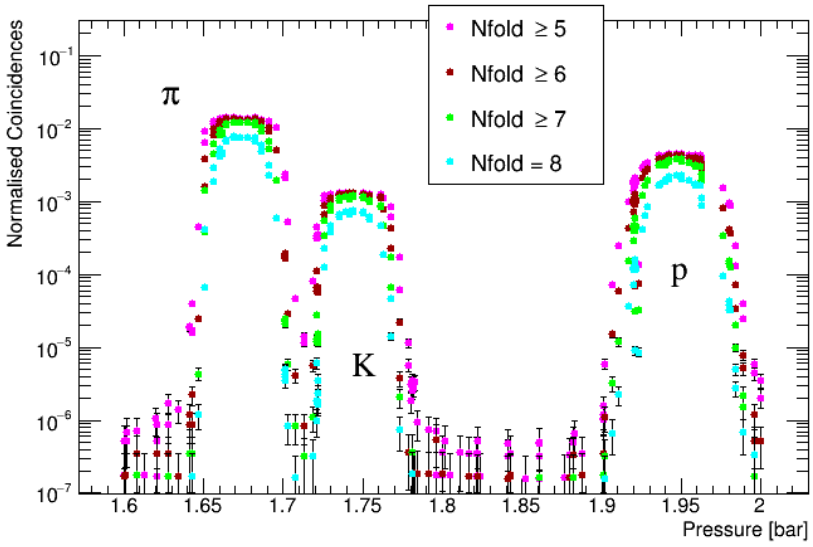

Figure 2.6: Pressure scan, done during the 2015 run, with different requirements on the number of sectors coincidences: the 1st peak corresponds to the pion peak, the 2nd to the kaon peak, and the 3rd one to the proton peak.

diaphragm, 8 PMTs are placed behind 8 annular slits to detect the light. Light from other beam components hits the diaphragm plane at a different radius and does not pass through the aperture and in this way it does not contribute to the detector rate.

The upgrade of the CEDAR, the KTAG, was built to cope with the challenging 45 MHz kaon rate and to achieve the required time resolution. The KTAG replaced the original 8 PMTs with 384 PMTs divided in 8 sectors with an average

rate of about 4 MHz on a single PMT.

The efficiency in kaon tagging required for the KTAG is above 95% with a kaon time resolution of the order of 100 ps, and the pion mis-identification probability has to be below 10^{-3}. The front-end electronics system is based on 8 boards (one per sector) using 8 ultra fast NINO amplifier/discriminator chips[18], to benefit from the fast PMT response. The CEDAR uses the common TDC-based readout system TDCB+TEL62 described in chapter 3.

2.2.2 GigaTracker

The GigaTracker (GTK) is an essential detector in the NA62 experimental strategy which allows to reconstruct the kaon track. This information is needed to compute the missing mass that is the basis for the kinematic rejection of the background. Figure 2.7 shows the importance of GTK in the missing mass resolution.

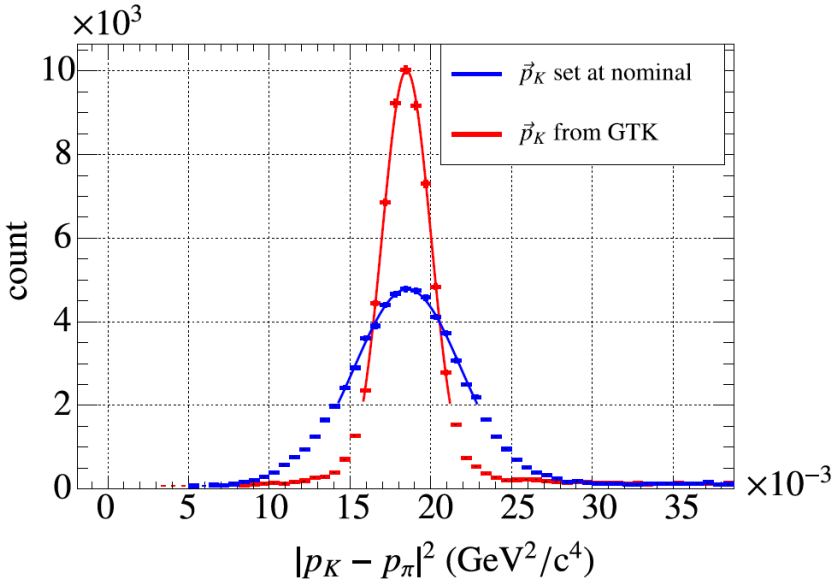

Figure 2.7: The squared missing mass distributions for $K^+ \to \pi^+\pi^0$ decays computed without (blue line) and with (red line) the GTK track information (d)ata obtained in the 2015 run.

The GTK is a spectrometer composed of three stations (see figure 2.8) situated between the four magnets of the second achromat, just before the fiducial decay region.

The measurements of the particle momentum and direction are obtained through the bending due to the magnetic field. Each GTK station is made of one hybrid silicon pixel detector of 63.1×29.3 mm^2 size containing 18000 pixels (300×300 μm^2 each) arranged in a matrix of 90×200 elements. The requirement on the direction resolution ($\sigma_\theta = 16$ μrad with a beam divergence of about 90 μrad) puts constraints on the choice of a sensor thickness of 200 μrad (corresponding to $0.22\%X_0$), because the material crossed by the particles at each station influences the angle measurement. Moreover the pixel thickness also affects the

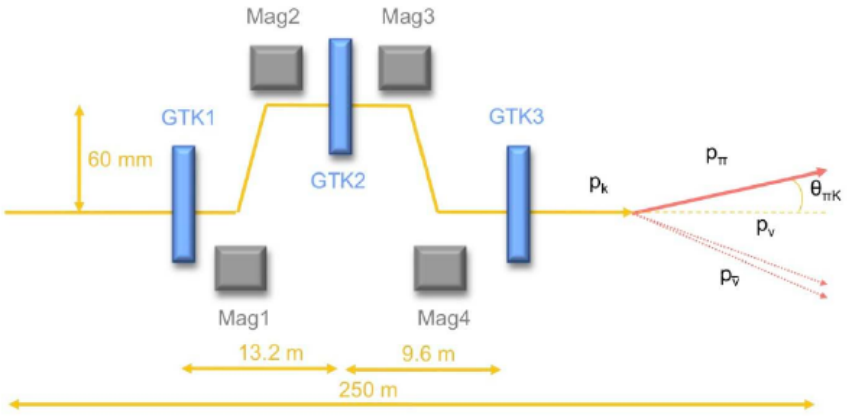

Figure 2.8: Sketch of the Gigatracker stations.

rate of hadronic interactions of the beam particles with the GTK material; including the material budget for the pixel readout and cooling, the total amount per station remains below $0.5\%X_0$.

The most challenging aspect of the GTK development was to cope with a very high rate of particles: it has to sustain a non-uniform beam rate of 0.75 GHz total, with a peak of 1.4 MHz/mm^2 around the centre[15] (see figure 2.9).

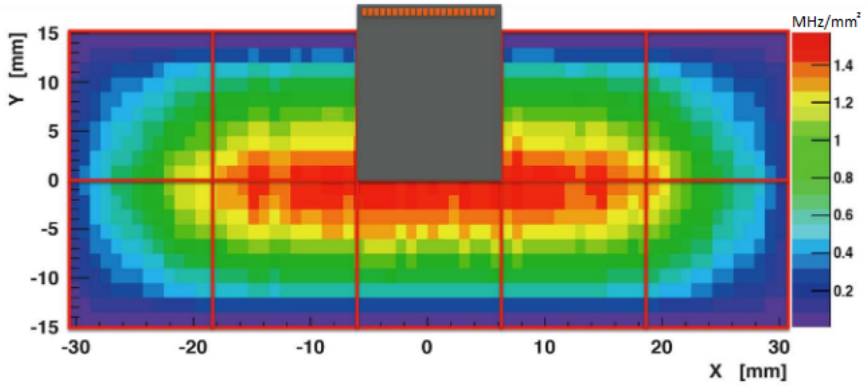

Figure 2.9: Beam intensity distribution on GTK3 station (expressed in MHz/mm^2). In grey is shown one of the 2 X 5 readout chips.

In order to reduce the kaon-pion misidentification to a negligible level, the required track time resolution using all three stations must be 150 ps (RMS). To meet this requirement each silicon sensor is bump-bonded to 2 X 5 TDC based read-out ASICs called TDCPix[71] (see figure 2.9), each of which delivers a time resolution of about 200 ps for a single pixel hit (see figure 2.10).

2.2.3 CHANTI

The GTK material can induce inelastic interactions of the beam particles. When this occurs in GTK3, the scattered particles (pions or muons) can enter the straw acceptance and mimic a kaon decay in the fiducial region. If no other tracks

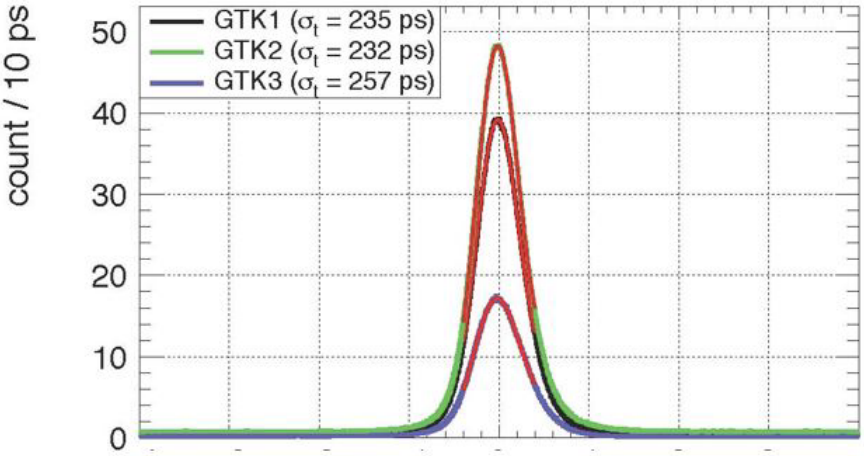

Figure 2.10: Time resolution for the GTK stations. Data obtained in the 2015 run.

are detected, such events look like $K^+ \to \pi^+\nu\overline{\nu}$ events. The probability of kaon inelastic scattering in the GTK3 is about 10^{-3}, so, to achieve the required signal over background ratio, a combined (analysis cuts and veto efficiency) rejection factors of at least 10^{-8} is needed on the beam scattering background.

The CHANTI detector was built for this purpose (see figure 2.11) and is composed of six stations of scintillator bars arranged all around the beam and located inside a vacuum vessel together with the GTK3 station.

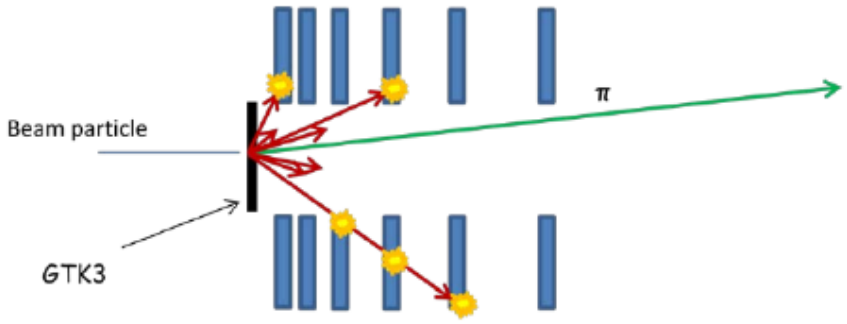

Figure 2.11: Sketch of an inelastic interaction in the GTK material. The scattered particles are detected in the CHANTI stations (blue).

Each station has an outer square side length of 300 mm and a rectangular hole of 90 X 50 mm^2 for the beam passage. The 6 stations, placed longitudinally at 27 mm, 77 mm, 177 mm, 377 mm, 777 mm and 1577 mm from the GTK3, allow an angular coverage from the centre of the GTK3 between 34 mrad and 1.38 rad. Each station is made of two layers (bars along the x and y directions) with 22 and 24 parallel triangular prism bars. Inside each bar a wavelength-shifting fibre collects the light that is detected by a silicon photomultiplier device.

The CHANTI is also sensitive even to the muon halo around the beam. The total expected event rate is about 2 MHz, so a time resolution below 2 ns is required to keep the random veto at a low level (2%). The CHANTI could veto

about 95% of kaon inelastic interactions in GTK3; this fraction increases up to 99% if we restrict only to signal-like events: the kaon either does not survive the inelastic interaction or does not decay in the fiducial volume together with only one track reconstructed in the STRAW spectrometer.

The CHANTI uses the LAV front-end electronics boards[20] to produce a Time-over-Threshold (ToT) signal output that is sent to the common TDCB + TEL62 readout system.

2.3 Detectors downstream the decay region

2.3.1 Photon veto system

The photon veto system is needed to reduce the background events coming from kaon decays and interactions before the decay region. The most challenging background is $K^+ \to \pi^+\pi^0$: the analysis requirement of π^+ momentum below 35 GeV/c guarantees that the two photons from the π^0 have more than 40 GeV of total energy. So considering a missing mass rejection power of 10^4 we need a photon detection inefficiency less then 10^{-8}. A photon veto covering an angle from 0 to 50 mrad from the decay volume satisfies such requirement. With this coverage only 0.2% of the selected $K^+ \to \pi^+\pi^0$ events (π^+ momentum between 15 and 35 GeV/c) have a photon escaping at larger angles while the other photon is within the detector acceptance.

The system consists of four detectors that cover different angle θ regions:

- the Large Angle Vetoes (LAV) are 12 stations covering the polar region 8.5 mrad $< \theta <$ 50 mrad;
- the LKr calorimeter covers the forward region (1.5 mrad $< \theta <$ 8.5 mrad);
- the Inner Ring Calorimeter (IRC) is a ring calorimeter surrounding the beam pipe to cover the area close to the central hole of the LKr;
- the Small Angle Calorimeter (SAC) is the last detector of the experiment and covers the region $\theta <$ 1.5 mrad

LAV

The Large Angle Vetoes are 12 stations (LAV1-12, see figure 2.12): the first eleven LAV are installed in the NA62 vacuum tank, while the last one is located in air outside of the tank between the RICH and the CHOD.

LAV stations are made of rings of lead-glass blocks (see figure 2.12) that were recovered from electromagnetic calorimeter barrel of the OPAL experiment[6]. Each block is a trapezoidal Čerenkov counter exploiting lead-glass[1] as active material; it is read out at one side by a PMT coupled via a 4 cm long cylindrical light guide of the same diameter as the PMT (see figure 2.12). The front and

[1]This material is about 75% lead oxide by weight and has a density $\rho = 5.5$ g cm^3 and a radiation length $X_0 = 1.50$ cm; its index of refraction is $n \approx 1.85$ at $\lambda = 550$ nm and $n \approx 1.91$ at $\lambda = 400$ nm.

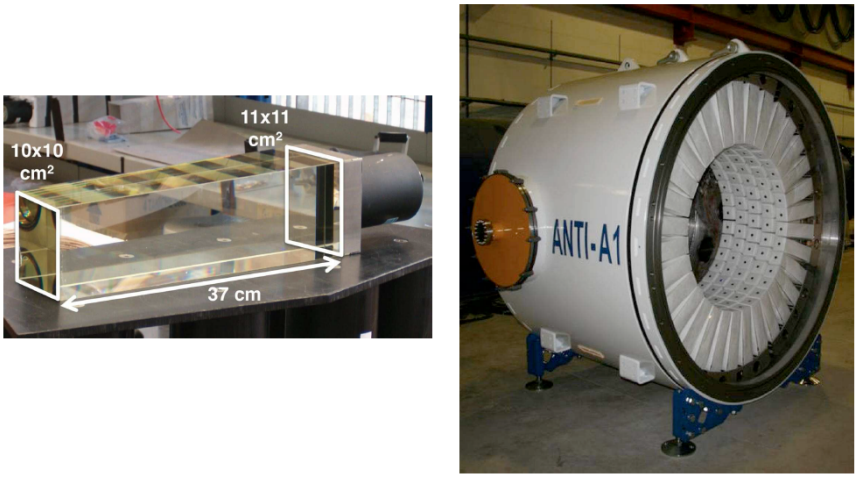

Figure 2.12: A LAV block (left). The LAV1 station, with 32 X 5 lead glass calorimeter blocks (right).

rear faces of the blocks measure about 10 X 10 cm^2 and 11 X 11 cm^2 respectively and the blocks length is 37 cm. A LAV station is made by arranging these blocks around the inside of a segment of vacuum tank: the blocks are aligned radially to form a ring. Multiple rings are used in each station to provide total minimum effective depth of 21 radiation lengths for incident particles. The blocks in successive rings are staggered and the rings are spaced longitudinally by about 1 cm.

The LAV provide time and energy measurements using the time-over-threshold (ToT) technique. The time resolution obtained for a single block is

$$\sigma_t = \frac{220\text{ps}}{\sqrt{E(\text{GeV})}} \oplus 140\text{ps}.$$

The front-end electronics is a custom discriminator board (called LAV front-end[20]) which converts the analog signals to low-voltage differential signals (LVDS). These signals sent to the common TDCB+TEL62 system which is used for read-out and trigger purpose.

LKr

The NA48 LKr calorimeter (see figure 2.13) is mainly used as a photon veto in the forward angle region (1.5 mrad $< \theta <$ 8.5 mrad). The LKr is also an important element for the L0 trigger reduction of $K^+ \to \pi^+\pi^0$ decays. The NA48 experiment [54] needed an electromagnetic calorimeter with good energy, position and time resolution, precise charge calibration, long-term stability and a fast read-out to study direct CP violation. The experiment chose a liquid Krypton almost homogeneous ionisation chamber to meet these requirements [54].

When a photon or an electron enters the calorimeter active volume, it produces an electromagnetic shower via pair production and Bremsstrahlung processes until the energy of the particles falls below the critical energy. The charged particles of the shower can ionise Krypton atoms producing a number of electron-ion pairs

proportional to the deposited energy. The produced electrons drift towards the anode where are collected before they can recombine. A liquefied noble gas was chosen to obtain a good resolution and energy linearity, with absence of ageing problems. Furthermore the relative short radiation length of the liquid Krypton allows a compact design without the need of passive material typical of sampling calorimeters.

The low boiling temperature of Krypton (120 K) entails that the whole detector has to be kept inside a cryostat: only temperature variations of few per mille are allowed not to have big variations of the drift velocity.

The LKr is octagonal, containing a circle of 128 cm radius, 127 cm thick and has a hole at the centre of 9 cm radius for the beam pipe. The total active volume of about 7 m^3 liquid Krypton (about 27 radiation lengths) is divided into 13248 cells 2 x 2 cm^2 by 18 mm wide, 40 μm thick copper-beryllium ribbons (see figure 2.13). The ribbons are distant 1 cm from each other, with no longitudinal segmentation, and are used as electrodes to collect the ionisation signal. A cell consists of a central anode, to which a voltage of 3 kV is applied, and two cathodes, one at each side, so that each cathode is in common between two cells.

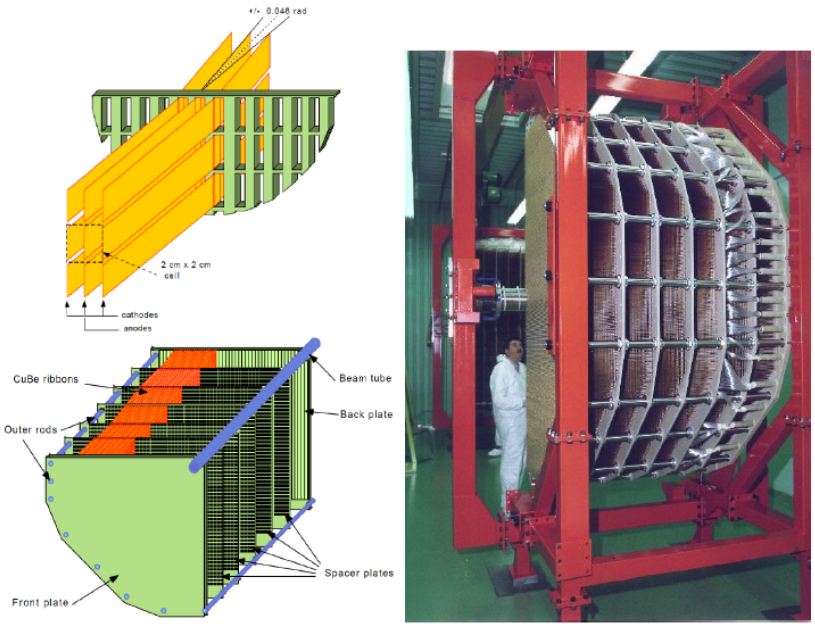

Figure 2.13: The LKr electrode structure and a detail of the LKr cells showing the ribbons structure (left). A picture of the LKr (right).

The energy resolution of the calorimeter, measured using a momentum scan of an electron beam with 0.1% momentum bite, can be parametrised as

$$\frac{\sigma_E}{E} = \frac{3.2\%}{\sqrt{E(\mathrm{GeV})}} \oplus \frac{9\%}{E(\mathrm{GeV})} \oplus 0.42\%.$$

where the first contribution is the term related to stochastic fluctuations, the second is mostly due to electronic noise and Krypton radioactivity, and the last one comes from the non perfect inter-calibration of the cells.

The space resolution, measured by comparing electron track extrapolation at the the LKr with the reconstructed centre of energy deposition, is

$$\sigma_{x,y} = \left(\frac{0.42}{\sqrt{E(\mathrm{GeV})}} \oplus 0.06 \right) \mathrm{cm}.$$

where the first term is due to the statistical fluctuations of the number of particles in the shower and the second one is due to the size of the cells. The time resolution on a single shower is of the order of 500 ps.

The LKr is read-out in a current-sensitive mode: the initial induced current is proportional to the ionisation generated by the electromagnetic shower and so to the energy of the crossing particle. The signal is sampled and digitized every 25 ns by a flash ADC-based calorimeter readout module (CREAM)[46]. To reduce the number of read cells and the output bandwidth, a zero suppression is applied to the cells with pulse height below a certain threshold.

IRC

The IRC is a ring-shaped calorimeter with an inner radius of 60 mm, an outer radius of 145 mm and 21 cm thick (see figure 2.14). It is placed in front of the LKr

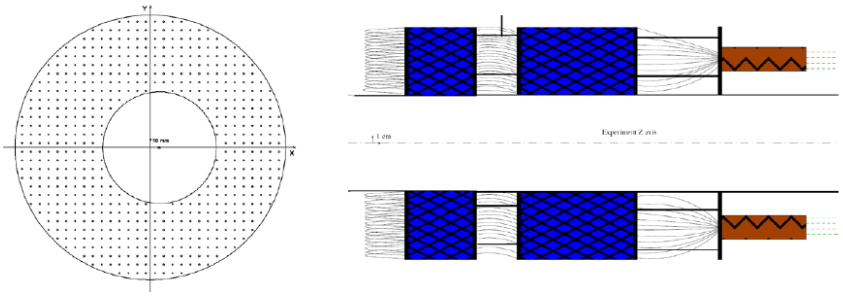

Figure 2.14: Layout of the IRC detector. The distribution of the fibre holes can be seen in the frontal view (left).

electromagnetic calorimeter and around the beam pipe to cover small angles but not too close to have high rate due to the beam halo. The detector is segmented into 4 parts each representing a 90° sector.

It uses the shashlyk design, that is based on consecutive lead and plastic scintillator plates (see figure 2.15). The crossing photon interacts with the lead and develops an electromagnetic shower that produces scintillation light inside the plastic material. The light reaches the photomultiplier via wavelength-shifting fibres. The attenuation length of the emitted scintillation light is much longer than the actual size of the IRC.

The photons of $K^+ \to \pi^+\pi^0$ decays give a rate of about few hundreds of kHz, which is a small fraction of the total rate of about 6 MHz to which the detector is exposed, that is mostly due to the beam halo.

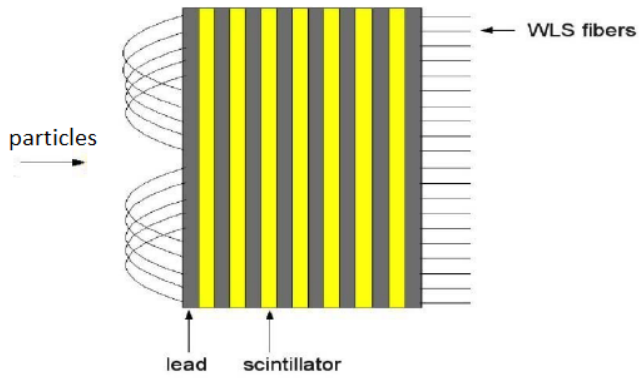

Figure 2.15: Shashlyk technology with lead and scintillator plates.

SAC

The SAC (see figure 2.16) is a shashlyk calorimeter with a square cross-section of 20.5 X 20.5 cm^2 and a thickness of 21 cm (17 radiation lengths). It is the last

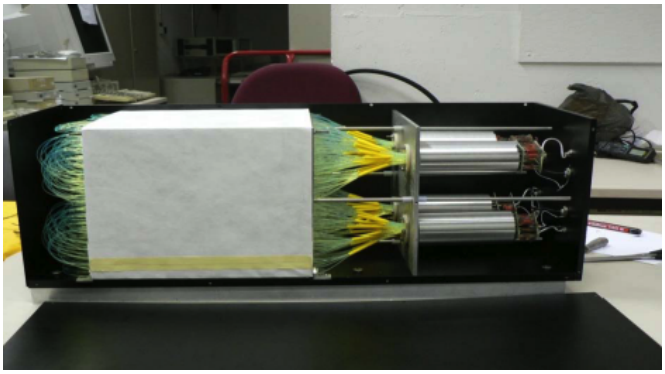

Figure 2.16: A picture of the SAC.

detector of the experiment, placed at the end of the experimental hall, behind the last magnetic dipole which further deflects the charged component of the beam by 13.6 mrad towards the beam dump. The SAC detects the remaining undeflected photons, in this way it covers the region down to 0 mrad corresponding to the beam pipe.

The rate on the detector is of the order of 100 kHz due to the remaining $K^+ \to \pi^+\pi^0$ decay.

The 480 WLS fibres are divided into four channels and read by four photo-multipliers.

The IRC and SAC read-out uses a CREAM module.

2.3.2 RICH

A Ring-Imaging CHerenkov counter (RICH) is the main particle identification detector of NA62; it is employed to obtain $\pi - \mu$ separation and to achieve a precise time measurement of the pion candidate. Because of its good time

resolution, it is one of the reference detectors in order to tag the passage of a charged particle and partially reject the multi-track events.

The RICH consists of a 17 m long vessel (see figure 2.17), with 3.8 m diameter, filled with Neon gas at atmospheric pressure (5.6% of a radiation length) and crossed by the beam pipe that allows the beam to pass through.

Figure 2.17: A picture of the RICH installed in the NA62 cavern.

The internal optics is made of a mosaic of 20 hexagonal spherical mirrors (see figure 2.18a) that reflects and convoys the Čerenkov light towards the upstream part of the detector where the photomultipliers are placed. The mirrors are divided into two spherical surfaces with centre of curvature respectively on the left and on the right of the beam pipe, in this way the absorption of reflected light by the beam pipe is avoided. In the the upstream part of the detector, two flanges (see figure 2.18b) host 960 photomultipliers each to collect the Čerenkov light. Each flange has a diameter of about 0.7 m and its centre is at a transverse distance of 1.2 m from the beam pipe axis. The active area of each PMT has a diameter of 8 mm and a Winston cone is used to collect the light from a pixel of 18 mm diameter.

A charged particle, traversing a medium of refraction index n, with a velocity

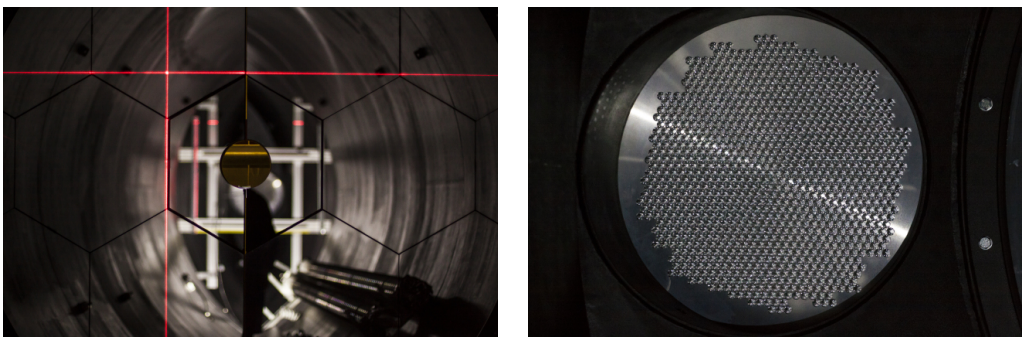

(a) . (b) .

Figure 2.18: The RICH mirrors (a), a laser was used to calibrate the mirrors alignment. One PMT flange (b).

βc higher than the speed of light in the medium, emits a e.m. radiation at an angle $\cos\theta_c = 1/(n\beta)$. The light cone is reflected by the mirrors toward the PMTs placed on the mirror focal plane where the cone image is a ring of radius $r = f\tan\theta_c \sim f\theta_c$ (f is the focal length). In this way the ring radius depends only on the particle velocity: this means that, for a particle of momentum p, the radius r depends only on its mass m

$$r \approx f\sqrt{\frac{2(n-1)}{n} - \frac{m^2}{np^2}}.$$

Using this information it is possible to obtain a pion-muon separation in the momentum range between 15 GeV/c and 35 GeV/c. Figure 2.19 shows the Čerenkov ring radius as a function of momentum (measured by the STRAW spectrometer) obtained with data of 2015 run and without any selection on particle type: electrons, muons, charged pions and scattered charged kaons can be seen. Cutting on the reconstructed mass, charged pions can be selected and muons

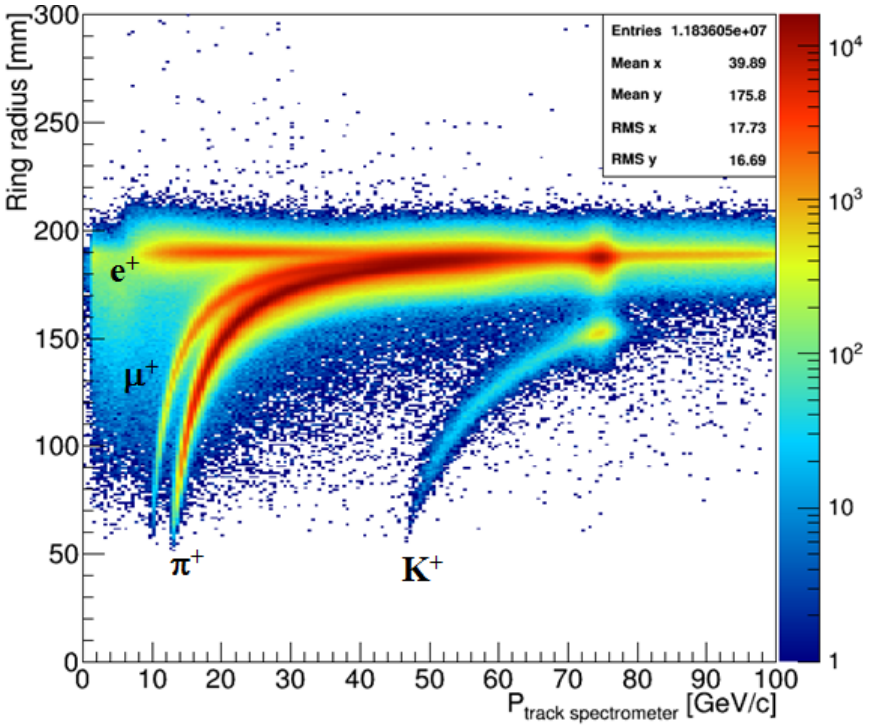

Figure 2.19: Čerenkov ring radius as a function of particle momentum; electrons, muons and charged pions can be seen; charged kaons from the scattered beam can also be seen. Particles with momentum higher than 75 GeV/c are due to background muons from the experiment target. Data obtained in the 2015 run.

can be rejected: with 2015 data a 86% pion efficiency and a 1.3% muon survival probability were measured. It must be noted that in 2015 the RICH mirrors alignment was not optimal and the need for better pion-muon separation was the main reason for detector maintenance carried out during the 2015-2016 winter shutdown.

The measured RICH time resolution was 65 ps and this leads to the choice of the RICH as one of the possible reference positive detectors for the L0 trigger (see section 3.3.1).

The front-end electronics uses the same NINO chip[18] as for the CEDAR to process the PMT signals; the readout of the about 2000 channels is done through the TDCB+TEL62 common system.

2.3.3 CHOD

During the first two run (2014-2015) NA62 reused the charged hodoscope (CHOD) of the NA48 experiment[54]. In the next data taking (run 2016) it will be used together a new version called NEW CHOD (see next section).

The CHOD is placed between the RICH and the LKr with the main purpose of detecting possible photo-nuclear reactions due to the crossing of particles through the RICH mirrors (about 20% of radiation length) that can produce low energy hadrons. This might reduce the photon veto power of the LKr, so the CHOD function is to re-establish this veto performance.

The CHOD consists of two planes, respectively with vertical and horizontal slabs (see figure 2.20), made of BC408 plastic scintillators. The distance between

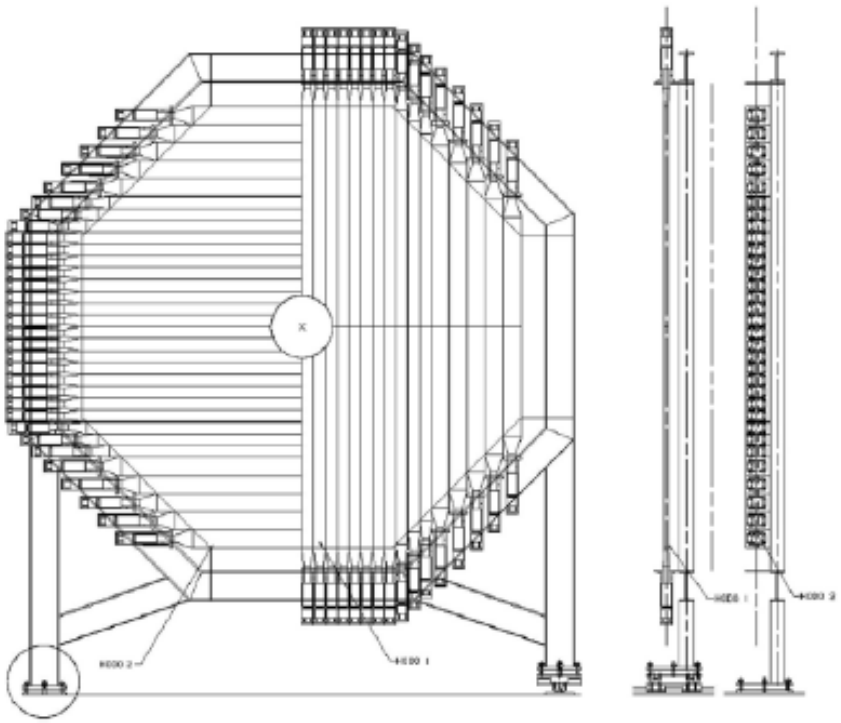

Figure 2.20: Sketch of the CHOD (front and side). One can see the horizontal and vertical planes.

the two planes is about 30 cm; each plane has 64 scintillator slabs of different length (from 60 cm to 121 cm) and width (from 6.5 cm to 9.9 cm), divided in 4 quadrants (16 slabs per quadrant). The thickness is the same for each slab and is

2 cm, corresponding to 0.05 radiation lengths. The beam pipe passes through a central hole with a radius of 10.8 cm. The passage of a charged particle produces scintillation light that is collected at the edge of the slab by a plexiglass fishtail shaped light guide connected to a photomultiplier.

The particle is identified through a time matching between hits in slabs of corresponding quadrants of the two planes. A cut in the time separation of the hits is useful to reduce fake coincidences due to back-splash from the calorimeter surface; when some particles of an electromagnetic shower go back to the hodoscope.

To avoid the effect due to the propagation time of the light inside the scintillator slabs towards the PMT, an impact point correction is applied during the reconstruction: in this way the CHOD can reach a time resolution of about 200 ps (see figure 2.21). With this time resolution the CHOD is another possible

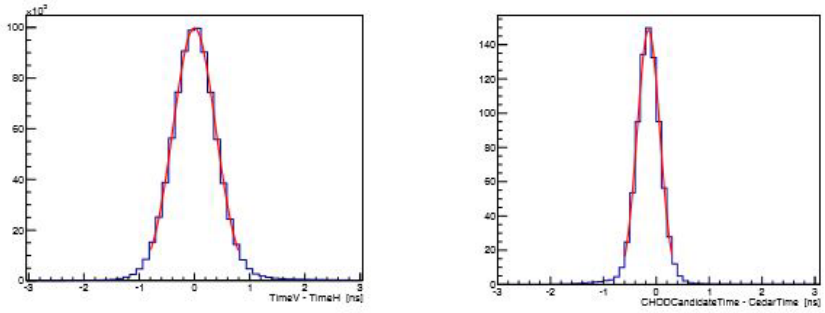

Figure 2.21: Left: distribution of the time differences between one horizontal and one vertical slab hit by a particle (data of 2015 run). A Gaussian fit with 400 ps sigma is superimposed to the data. Right: distribution of the time differences between CHOD candidates and KTAG kaon signals (data of 2015 run). A Gaussian fit with 215 ps sigma is superimposed to the data.

reference positive detector for the main L0 trigger (see section 3.3.1).

The detector uses the LAV front-end electronics[20] and is read-out by the common TDCB+TEL62 system.

2.3.4 NEW CHOD

A new charged hodoscope was designed and will be used for the first time in the 2016 run together with the old CHOD. The main reason to build the NEW CHOD is the high hit rate at which the long slabs (1 m) of the CHOD are exposed. The intrinsic dead time and the light transit time inside the scintillator are not compatible with the expected overall rate on the detector above 10 MHz.

The NEW CHOD is a two-dimensional array of 152 scintillator tiles (see figure 2.22) installed after the LAV12. In each quadrant, a 30 mm thick plastic scintillator is divided into 38 tiles. The scintillation light is collected and transmitted by 1 mm diameter wavelength shifting fibres to be detected by arrays of 3 X 3 mm^2 silicon photomultipliers (SiPMs) on mother-boards located on the periphery of the detector. A maximum rate of the order of 500 kHz is expected on the tiles close to the beam pipe.

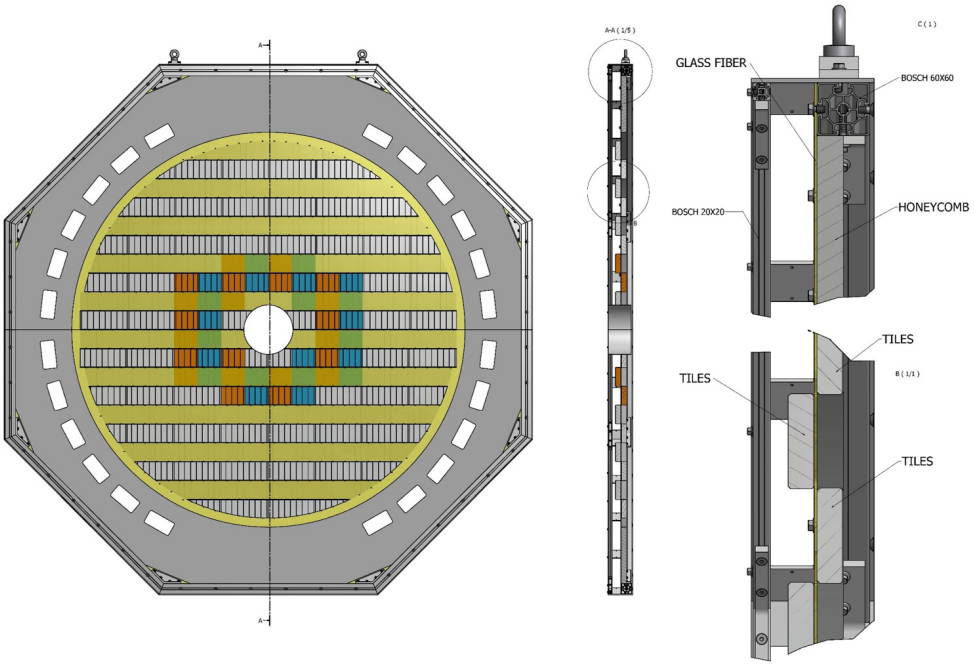

Figure 2.22: Sketch of the NEW CHOD, front and side views.

The signals are shaped using constant fraction discriminators to improve the time resolution, and read out by the common TDCB+TEL62 system.

2.3.5 The muon veto system

A further reduction of the $K^+ \to \mu^+\nu_\mu$ background is achieved by the muon veto system, composed of three detectors (MUV1, MUV2, and MUV3). The first two modules (MUV1 and MUV2) are downstream of the LKr calorimeter and work as hadronic calorimeters measuring the deposited energies and the shower shapes of incident particles, the MUV3 is instead located behind a 80 cm thick iron wall and is employed as a fast muon veto in the lowest trigger level (L0) and for offline muon identification (see figure 2.23).

MUV1 and MUV2

The MUV1 module is a detector built for NA62, while the MUV2 detector is the front module of the former NA48 hadron calorimeter[54] (HAC). The MUV2 is mounted backwards with respect to NA48 to allow a better servicing access to the PMTs. Both are iron-scintillator sandwich calorimeters; they have 24 (MUV1) and 22 (MUV2) layers of plastic scintillator strips alternated with iron plates. The plates have dimension 2600 X 2600 X 25 mm^3; a central hole of diameter 212 mm allows the beam pipe passage. The scintillator strips of both modules are alternately horizontal and vertical.

The MUV1 consists of 48 X 24 strips (1152 in total) of about 6 cm width. light is read by two wavelength-shifting fibres per scintillator strip. The fibres of one longitudinal row of scintillators are bundled together to direct the light to one single PMT, therefore no longitudinal segmentation exists.

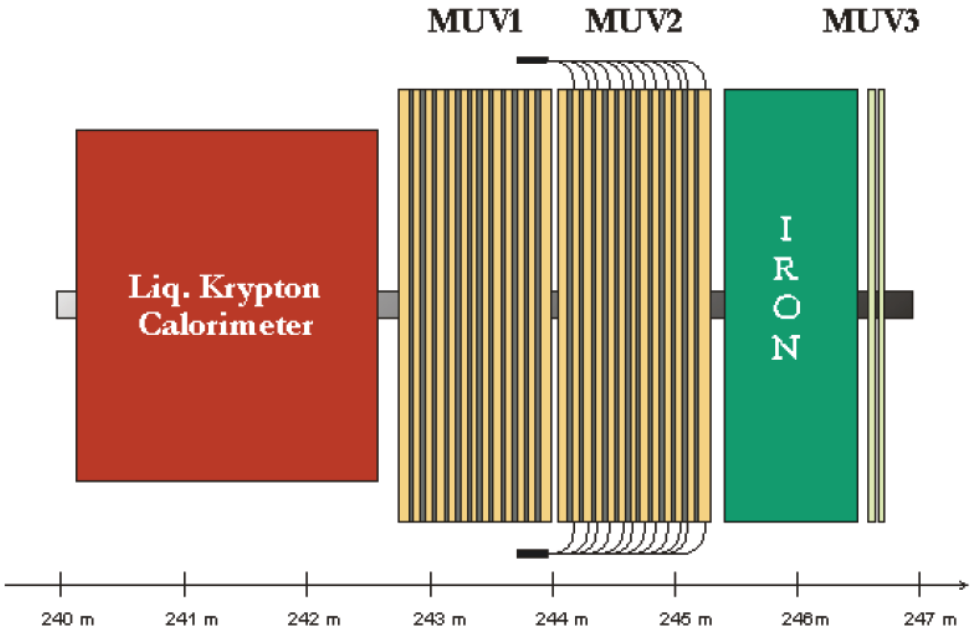

Figure 2.23: Sketch of the Muon Veto System.

The MUV2 is composed of 44 strips of about 11 cm width, each one spanning half of the transverse size of the detector. Consecutive strips with identical transverse positions are coupled to the same photomultiplier using plexiglass light-guides.

These two detectors are read-out with the CREAM modules[46] used by the LKr calorimeter.

MUV3

The MUV3 detector (see figure 2.24) consists of an array of 12 x 12 plastic scintillator tiles, 5 cm thick, with a transverse area of 22 x 22 cm^2. Eight smaller tiles are mounted around the beam pipe to cover the region with a higher rate.

The light produced by traversing charged particles is collected by two photomultipliers positioned about 20 cm downstream. The maximum time jitter between photons produced is below 250 ps, in this way the required time resolution is preserved. The only error in the time measurement could be due to particles traversing the PMT windows: these particles produce Čerenkov photons who arrive earlier than those produced in the scintillators, with typical time differences of about 2 ns. To overcome this problem each scintillator tile is read out by two PMTs. The output time of the two PMT signals coincidence, corresponds to the time defined by the PMT which is unaffected by the Cerenkov photons. The time resolution of the MUV3 is below 500 ps, sufficient to keep the random veto probability at a low level.

The PMT output signals are sent to constant fraction discriminators (CFD) which are then read-out through the common TDC-based system TDCB+TEL62.

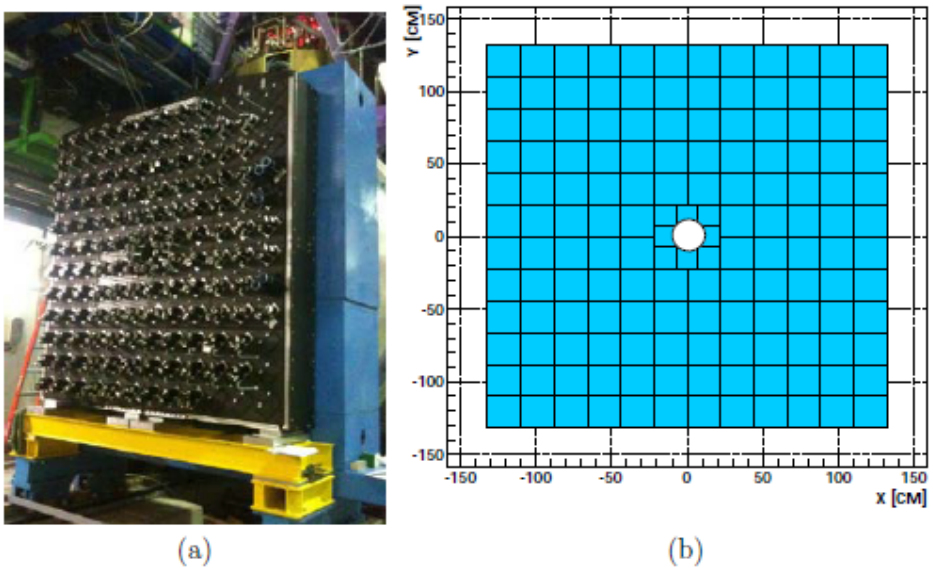

Figure 2.24: MUV3 detector picture (a) and layout (b).

2.3.6 The STRAW tracker

The STRAW Tracker is a magnetic spectrometer which has the purpose of measuring the momentum, position and direction of the charged particles originating in the decay region. It is used in the offline analysis and in the next run (2016) it will also enter in the software L1 trigger to reject multi-particle events together with events decaying out of the fiducial region and undecayed beam particles.

The spectrometer consists of 4 straw chambers and a dipole magnet with a momentum kick of 270 MeV/c (the magnetic field integral is about 0.86 Tm) placed between the second and the third chamber (see figure 2.25 and 2.26).

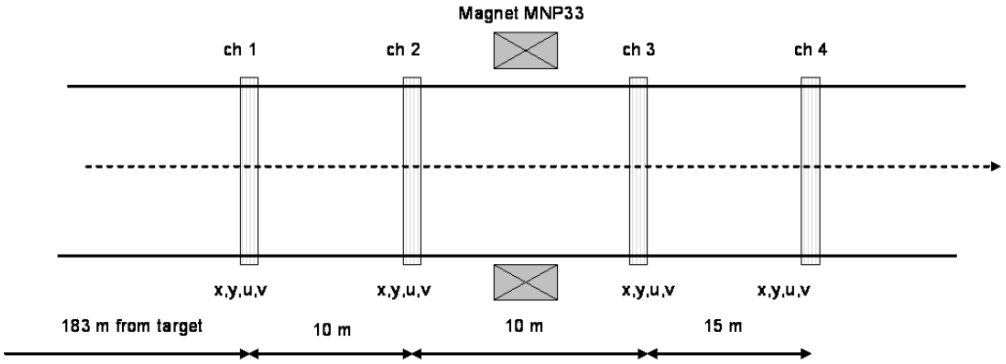

Figure 2.25: Schematic view of the STRAW Tracker.

Every chamber hosts 1792 light straw tubes arranged on 4 different orientations (called views: X(0°), Y(90°), U(-45°) and V(+45°) see figure 2.27) that are orthogonal to the beam axis [15].

The active area of the detector is octagonal with diameter 2.1 m. The central region, 12 cm wide, of each view has no straws to allow the beam crossing,

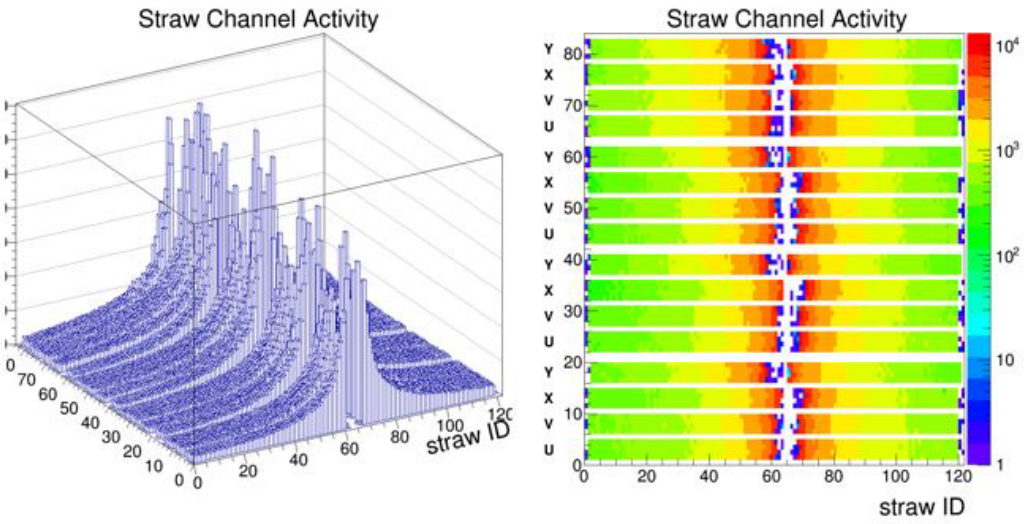

Figure 2.26: Online plot showing the straws hit activity in all four chambers during the 2015 run. The histogram shows triggered data as it is sent to the PC farm.

resulting in a loss of about 10% in acceptance. The existence of a central zone without straw entails a subdivision of the transverse plane in four different zones depending on the number of views covering it (see figure 2.28 and 2.29). Indeed there are zones covered only by 1 view while others are covered by 2, 3 or 4 views;

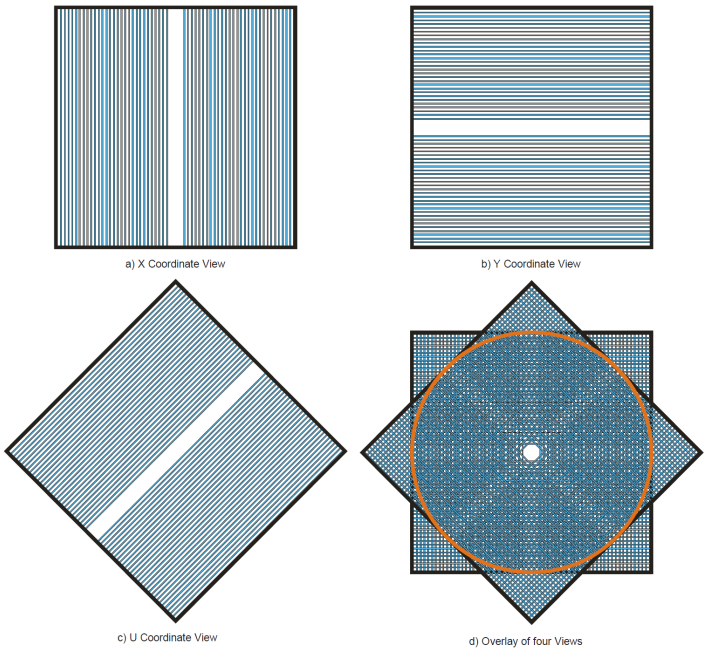

Figure 2.27: Drawing of the four views of each straw chamber: a) vertical straws for the x-coordinate; b) horizontal straws for the y-coordinate; c) 45° oriented straws for the u-coordinate (the v-coordinate is obtained from straws orthogonal to c); d) full chamber with all four views.

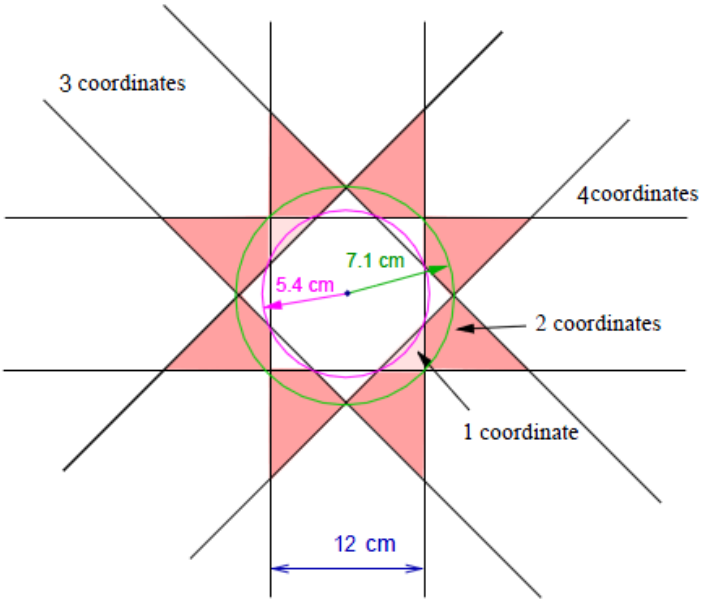

Figure 2.28: Sketch of the division of the x,y plane in four different zones depending on the number of views covering it.

this is an important point to keep in mind in the development of a reconstruction algorithm because for example the 1-view zone does not allow to know both coordinates of the particle crossing. A Monte Carlo simulation shows that the fraction of signal events in the fourth chamber crossing only 1 view is 2%, 2 views is 10%, 3 views is 50% and 4 views is 38%.

Each view is made of four planes of 112 straw tubes, staggered to solve the left-right ambiguity (see figure 2.30); the distance between the straws in one layer is 17.6 mm. The straws are 2.1 m long, 9.8 mm in diameter and are fabricated from 36 μm thick PET foils coated inside with two thin metal layers (0.05 μm of Cu and 0.02 μm of Au) to provide electrical conductance on the cathode. The anode wire has a diameter of 30 μm and is made of gold-plated tungsten. The straws are filled with a gas mixture of Argon (70%) + CO2 (30%). The total amount of material ($< 0.5\%$ X_0 for each chamber) is low in order to minimize multiple Coulomb scattering along the particle trajectory. The space resolution on a single view obtained is about 130 μm and the expected track momentum resolution is

$$\frac{\sigma_p}{p} = (0.32 \oplus 0.008 \cdot p)\%.$$

where p is the momentum expressed in GeV/c. The first term of the momentum resolution is due to multiple scattering while the second one depends on the points[2] spatial resolution.

In order to develop the offline tracks reconstruction or the online trigger algorithm, it is important to understand how the STRAW spectrometer works in detail. A charged particle traversing the straw ionizes the gas on the way. The

[2]The points are obtained from two clustering steps, one to merge the hits inside the same view and obtain view clusters and the other to merge the view clusters of the chamber; see chapter 5 for details.

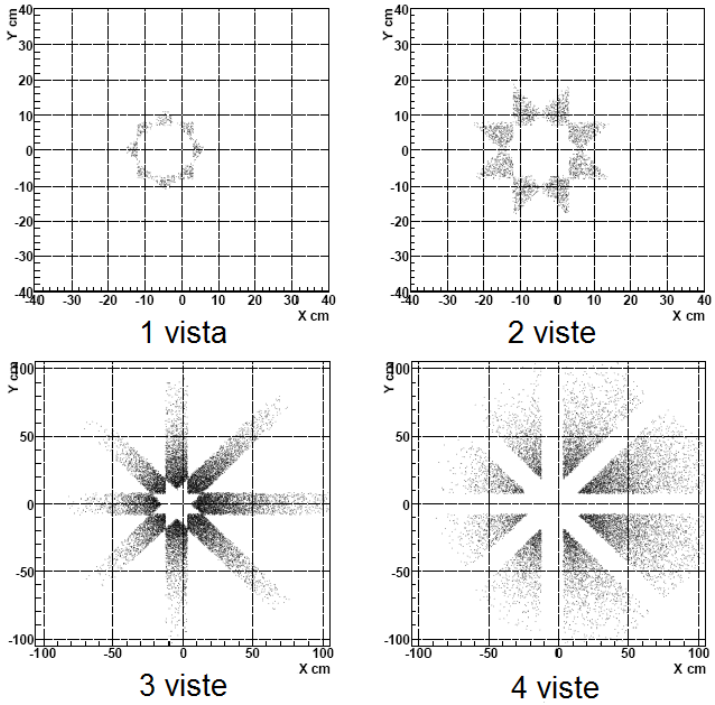

Figure 2.29: Impact point distribution in the 4th chamber for a signal event, for different number of hit views.

electrons created by the particle move toward the anode with a drift velocity of about 3 cm/μs. Electrons arriving inside 300 μm from the wire have enough energy to ionize the gas molecules producing avalanches. The straw signal starts with the first avalanches formation, generated by electrons less distant from the wire, and end after the arrival of the last avalanches due to electrons regions near the tube edge. The time difference between the time arrival of the first avalanches and the particle crossing is called *leading time*, while the difference with arrival of the last avalanches is called *trailing time* (see figure 2.31). The value of the *leading time* depends on the minimum distance of the particle crossing from the wire and its value is between 0 ns and about 160 ns. The *trailing time* is instead fixed to about 160 ns, depending only on the straw radius and the *trailing time* resolution.

The read-out electronics was designed in order to cope with an overall particle rate of about 15 MHz and a single straw maximum rate of 700 kHz. The front-end electronics called COVER is placed directly on the detector, sealing the gas volume [24]. A COVER can read-out 16 channels using 2 8-channel CARIOCA chips developed for LHCb [80]. The chip amplifies, shapes and discriminates the current signal induced on the wire chamber electrodes. The discriminator output is sent to the LVDS driver that provides the CARIOCA output signal. The time measurement is performed on an FPGA located directly on the COVER board. Leading and trailing are treated in parallel and the TDC time resolution is of 0.78 ns. After the digitization of the signals and the time measurements, the data are sent to the Straw Read-out Board (SRB). Each SRB can read-out 16 COVERs (256 channels), it selects and packages the data to send it to the PC Farm.

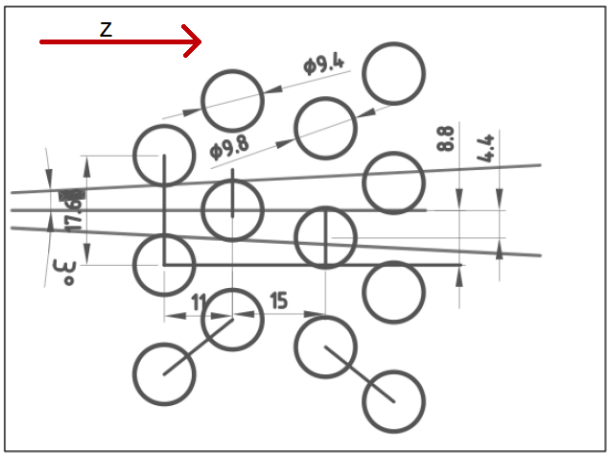

Figure 2.30: Straw layout in one view.

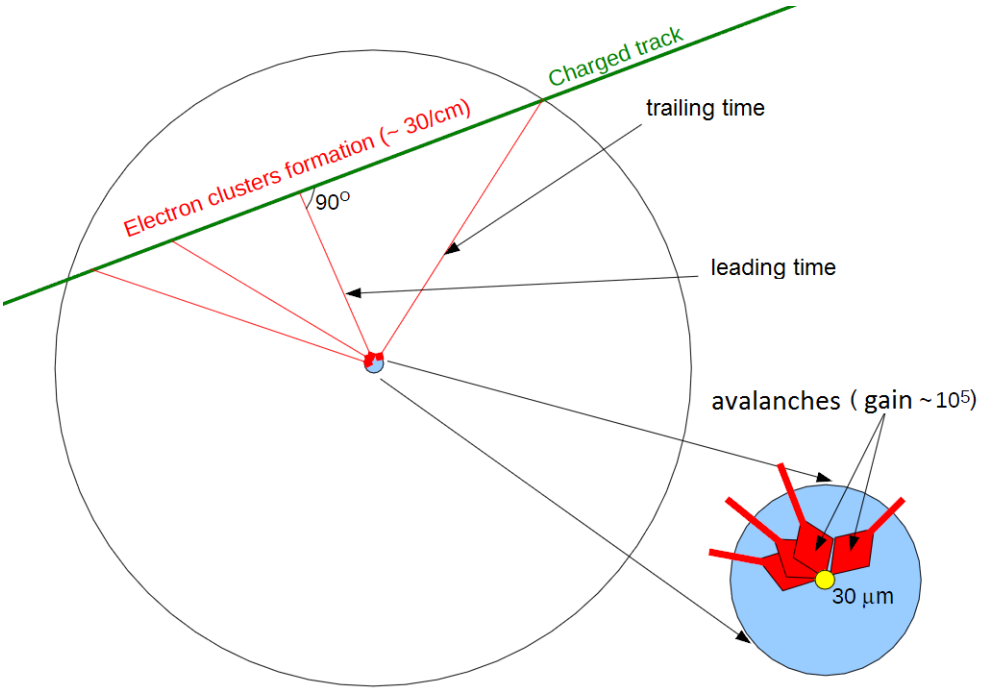

Figure 2.31: Sketch of the straw signal formation.

Chapter 3

TDAQ system

3.1 Introduction

The high event rate (about 13 MHz) and the number of detectors in NA62 result in a large amount of output data ($\sim$ 30 GB/s) that is difficult to store without filtering. The total number of channels in NA62 is above 80000: considering the detector rate and size of each subdetector packet, the system produces a raw data bandwidth of the order of 2 TB/s. The number of channels and the typical hit rates of the detector are presented in table 3.1. A high performance trigger and data acquisition (TDAQ) system is therefore necessary, which must minimize dead time and maximize data collection rate. To do that, NA62 developed an unified trigger and data acquisition system: trigger is integrated inside the DAQ system, allowing to have a good control of the trigger, that use the same data available at readout, and a excellent flexibility. The trigger system is organised in three levels: the lowest-level trigger (L0) is hardware and is followed by two software high-level triggers (L1 and L2) implemented in a PC farm.

Sub-detector	**Total channels**	**Hit rate (MHz)**
CEDAR	240	50
GTK	54000	2700
LAV	4992	11
CHANTI	276	2
STRAW	7168	240
RICH	1912	11
CHOD	128	35
NEWCHOD	304	45
IRC	20	4.2
LKr	13248	40
MUV	432	30
SAC	4	2.3

Table 3.1: Number of channels and typical hit rates of NA62 sub-detectors

The common clock of the experiment is provided by the Timing, Trigger and Control (TTC) system used in LHC experiments[26], its frequency is close to 40

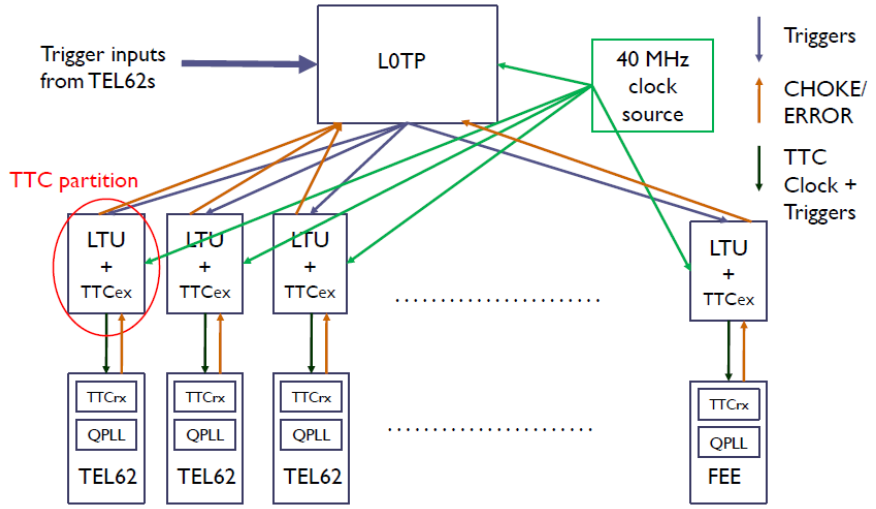

Figure 3.1: The NA62 TTC system.

MHz and is the common unity reference for all time measurements, which are defined by a 32-bit timestamp, with 25 ns LSB (least significant bit), plus 8 bit of fine time with 100 ps LSB covering the duration of an entire SPS spill (which is of the order of 10 s).

3.2 The TTC system

The Timing, Trigger and Control (TTC) system [26], developed for the LHC experiments, provides the timing of the experiment with a common, centrally generated, free-running synchronous 40.079 MHz clock. This clock is the unique reference for time measurements of all the experiment. The above frequency is the exact bunch-crossing frequency of the LHC but in NA62 the kaon beam is unbunched, and this is just the reference clock frequency of a free running clock. The clock produced by the TTC system is distributed all over the experiment through optical fibres to detectors' DAQ and the L0 trigger processor. The NA62 TTC system (shown in figure 3.1) is composed of a central clock source and many sets of LTU + TTCex modules. These modules encode and send clock and triggers to the readout electronics of the detectors. A back pressure system of CHOKE and ERROR signals is implemented : they are produced in case of exceedingly high rate or errors by the data acquisition boards and the LTU propagates them to the L0TP to momentarily stop L0 triggers. The LTU [70], a 6U VME module, is an updated version of the Local Trigger Unit designed for the ALICE experiment. An on-board FPGA on the LTU receives the clock from the TTCex and is programmed to perform the following tasks: dispatch triggers received from the L0TP (L0 Trigger Processor, see the next section) to the TTCex for optical encoding, in the form of a trigger signal and a trigger message containing 8 bits; propagate the back pressure CHOKE and ERROR signals to the L0TP; deliver synchronously to the readout systems the start of burst (SOB) and end of burst (EOB) signals, received from the SPS, as special

trigger messages: these signals respectively start and end the data acquisition operations inside a single burst synchronously to the entire system. In the trigger messages the lowest two LSBs bits are reserved to encode SOB and EOB signals, the remaining 6 bits represent the Level 0 trigger type (up to 63 different types).

The TTCex module [91] is a 6U board: it receives the main clock which drives an internal QPLL, and is linked to the LTU to receive trigger signals and trigger information messages. The module provides several optical fibre outputs in which clock, trigger signals and trigger messages are encoded together.

All the subdetectors front-end subsystems are endowed with a TTC interface containing an optoelectronic receiver and a TTCrx chip [8] which decodes the L0 trigger information.

The trigger word can encode several physics triggers belonging to different conditions and subdetectors, as well as some service triggers, e.g. signal useful to synchronize all the detector together, to monitor the the noise or the background in the detectors and the CHOKE/ERROR signals which represent a warning or a problem in the general data acquisition and they says to the read-out board to pause or stop the data acquisition.

3.3 The trigger system

The general TDAQ structure of a modern high energy experiment is organized on more levels: the detectors data are stored if they satisfy some requirements established by several sequential trigger levels. The NA62 trigger system is structured in 3 levels that have to reduce the event rate from about 13 MHz to some kHz. The number of detectors channels and their high rates led the NA62 collaboration to choose for the first level (called L0) a fully hardware trigger; after the L0 trigger, the sub-detectors transfer the data to a pc farm where the L1 and L2 trigger are implemented. The L1 is based on the information computed by each complete sub-system. The L2 uses assembled and partially reconstructed events with the possibility to use correlations between different sub-detectors. The NA62 trigger hierarchy is shown schematically in figure 3.2.

3.3.1 L0 trigger

The L0 trigger is digitally implemented on hardware in the common TEL62 board, it's based mainly on input from CHOD, MUV, RICH, LKr and LAV12 and with the goal of reducing the event rate from about 13 MHz to 1 MHz. The default L0 trigger algorithm consists in requiring a single charged track in the CHOD and RICH, nothing in the MUV3 and in the LAV12, and an amount of energy in the LKr and in the MUV1 compatible with a charged pion. Together with this main trigger, other L0 trigger could be implemented to acquire a selection of events useful for different physical goals respect to the branching ration measurement of the $K^+ \to \pi^+ \nu\overline{\nu}$ decay. The signals of the CHOD and RICH will allow to tag a charged particle within the detector acceptance, reducing the rate due to K decays downstream of the final collimator. It is possible to use, in addition, the hits multiplicity to select multi-track events. The fast third station

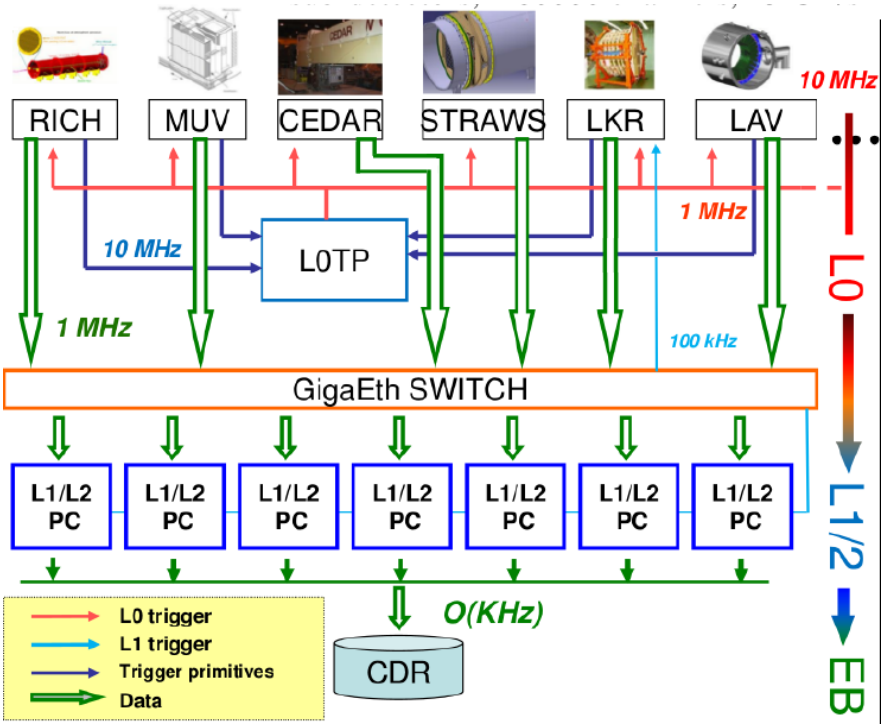

Figure 3.2: Schematic view of NA62 TDAQ system

of the muon veto (MUV3) is used to reject the high rate of muons due to the major background decay $K^+ \to \mu^+\nu_\mu$ (about 63% of Branching Ratio) and the muon halo components from decays upstream of the final collimator. The LKr and MUV1 are useful to suppress the rate due to the other background decay $K^+ \to \pi^+\pi^0$, by requiring the energy released corresponding to the charged pion electromagnetic shower. An online cluster counting with a time resolution of 1 ns can allow a good rejection and at the same time give useful information for several other sets of physics triggers. The RICH is able to contribute by exploiting hits multiplicity, for the reduction of the background due to multi-track events, and giving a very precise time measurement O(300 ps); we are not able to use the particle identification in the L0 trigger because it requires the correlation with the information from other sub-detectors like the measurement of the particles momentum from the slow magnetic spectrometer. The RICH trigger condition is computed in a single TEL62 board, called *RICH MULTI*, that collect the signal of all the detector super-cells (a super-cell is the digital OR of 8 RICH PMs). The last station of the LAV veto (LAV12) is used to reject at the L0 a part of the events with photons in the final state. The other stations are used inside the L1 trigger condition. It is not possible at the moment to use all the LAV station in the L0, but is under development a system that will allow the firmware communication between the LAV TEL62 board to generate a common trigger condition. The new-CHOD detector is been installed for the 2016 RUN; it could be used, simultaneously, with the old CHOD detector to select single charged tracks. For the first run periods will be test its trigger and read-out efficiency.

The electronic boards connected to these sub-detectors inside the trigger system produce L0 trigger primitives with timestamp and fine time to allow the

time matching. The L0 trigger primitives are managed by a central L0 Trigger Processor (L0TP). The L0TP used during the 2015 run is a FPGA system based on the Altera®development DE4 board[10] which accommodates a Stratix®IV FPGA[14], plus a TTC [8] interface card and daughter-cards for 8 Gigabit ethernet ports used for trigger primitives reception. The received primitives are stored in RAMs implemented in the FPGA, with a RAM address depending on the primitive time. The timestamps of a reference (positive element) detector are stored in a FIFO, and subsequently read to search for primitive matching in times from other detectors; different trigger masks coexist for different physics goals, and a look up table is implemented inside the FPGA for this multiple matching purpose. After the matching, if the trigger conditions are satisfied the L0TP generates a L0 trigger signal followed by a trigger type word that is dispatched by the TTC system back to all detectors. When the detector boards receive this signal they read-out the data inside a programmable number of time slots (each one of 25 ns) around the trigger time. The data, waiting for the L0 trigger signal, is stored into some memory buffer (on the TEL62 boards is a DDR2 memory).

The maximum L0 trigger latency was set to 1 ms and it is limited by the memory inside the L0TP indeed the read-out electronics of the detectors can currently store data for more time like the DDR2 memory in the TEL62 ($\sim$ 50 ms) and the memory in the readout board used by the LKr ($\sim$ 10 ms).

3.3.2 L1 and L2 triggers

The sub-detector data, after the L0 trigger signal, are extracted from memories and sent to the PC farm where the L1 and L2 triggers are implemented. The L1 algorithms check data quality conditions and then requires simple correlations between conditions computed by single sub-detectors. The L1 trigger uses the KTAG to cut the non-kaon component of the beam, the LAV stations to reject events with photon and the CHOD to reduce multi-tracks events. A significant part of the rejection power is obtained using STRAW informations that help to cut events with a decay vertex out of the fiducial region, due to beam particles that are inside the detector acceptance and multi-body decays. The L1 trigger is necessary to achieve an overall trigger rate below 100 kHz. In case of positive L1 decision, a complete event reconstruction at L2 will be done.

The L2 takes care of accepting, for the main trigger, events with only a single identified charged pion. These two software level triggers are both implemented inside the same PCs, so useless data transfers are avoided. All the events accepted by the L2 trigger are finally stored on tape. The available bandwidth for data storage is about 100 MB/s, this limits the final output trigger rate to about 10 KHz.

The NA62 Pisa group is developing a parallel fast online trigger system using commercial graphic processors (GPUs)[51]. This system could support some L1 and L2 trigger algorithms acting as a Level 0.5 trigger between the hardware level and the software levels. Two low latency applications under evaluation in NA62 are the RICH online ring-finding, both for L0.5 and L1, and a L1 tracks reconstruction for the STRAW spectrometer.

3.4 Data acquisition system

The high hit rate and the consequent need of a good time resolution to have an efficient selection of the events, led the collaboration to use a TDC-based system for many detectors. A TDC system can also provide pulse-height information using a time-over-threshold approach: both leading and trailing edges of pulses should be measured to utilize this method. Consequently most of the detectors of the experiment (CEDAR, CHANTI, LAV, RICH, CHOD, NEWCHOD and MUV3) adopted a TDC and FPGA-based common readout composed of the TEL62 carrier board[88][17] and the TDCB daughter-card[85]. A part of my PhD work consisted of the firmware development of these two boards; this will be described in sections 3.5.2 and 3.6.1.

Due to specific needs, some detectors chose to adopt a different custom TDC system or an ADC based readout instead and these read-out systems are briefly described in the rest of this section. The readout of the Gigatracker is based on a TDCPix chip that provides, in addition to the hit time, the time-over-threshold self-triggered measurement for 360 channels, the pre-amplification and the discrimination of the signal[71]. The TDCPix time bin size is about 100 ps, the expected rate is about 210 MHits/s and the output is given by 4 3.2 Gbit/s serial links. Taking into consideration the propagation of the signal through the chip and the relative time correction the chip time resolution is about 70 ps. The 4 output serial links send data to a carrier GTK-RO VME 6U board where it is stored waiting for a L0 trigger decision. After the reception of a L0 trigger signal the data inside a 75 ns time windows are sent to the readout PC. There is also on the board a TTC interface to receive triggers from the central L0 Trigger Processor and to send the clock to the TDCpix.

The STRAW spectrometer electronics[24] is based on a 8-channel analogue front-end chip, the CARIOCA chip[80],containing a fast pre-amplifier, semi-Gaussian shaper, a tail cancellation circuitry, base-line restorer and a discriminator. Two CARIOCA chips are integrated in a custom COVER board [75] together with an Altera®Cyclone®III FPGA [9]. The COVER board houses 16 pairs of TDC implemented within the FPGA with de-randomizers and an output link serializer. The full system is composed of 14236 TDCs producing a data rate of order 2 GB/s. The back-end VME 9U Straw Readout Board (SRB) receives data from 16 COVER boards for processing (in FPGAs) and storage in DDR3 memories. A TTC interface is also present, to optically receive the clock and the L0 trigger signal. After receiving a L0 trigger, data are extracted from the buffers and sent to the PC farm.

The LKr, the MUV 1 and MUV2 use a FADC (Flash ADC) based readout. The readout board is a Calorimeter Readout Module (CREAM) [46] developed by CAEN (see figure 3.3). It is a VME 6U board able to digitise 32 LKr channels at 40 MHz using four 8-channel, 14-bit ADCs. 414 such boards are needed to read out the 13248 calorimeter cells. After signal digitisation, samples are stored in a circular buffer built inside a DDR3 module, waiting for the L0 trigger signal. Upon reception of such signal through a custom backplane, data is moved to the L0 buffer, also built in the same DDR3 module, where it waits for a L1 trigger signal. This is one main differences with respect to other detectors: due to the

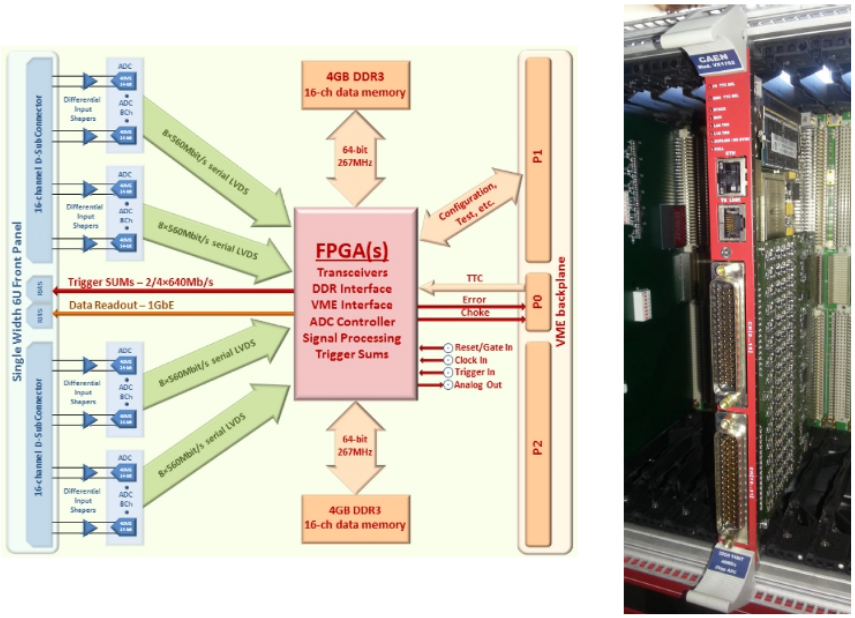

Figure 3.3: Logical scheme and photo of a Calorimeter Readout Module.

high data rate, the LKr is only read out at the reduced L1 trigger rate (below 100 kHz). When such signal is received, the corresponding data is finally sent to the PC farm. The CREAM module also computes digital sums of 4×4 channels, called Super-cells, for L0 trigger purposes: two Super-cells are read out by each CREAM, and digital sums are sent every 25 ns to a system based on 36 TEL62s and custom interface mezzanine boards, where LKr L0 trigger primitives, based on energy deposits and cluster identification, are generated.

At present, the IRC and SAC small angle photon veto detectors use two different readout system together: the TDCB-TEL62 and the CREAM board systems. Both IRC and SAC have only 4 channels, this number is linked to the transversal dimension of an electromagnetic shower indeed a greater segmentation of these detectors would not have diminished the single channel rate.

3.5 The TDC Board

The TDC Board (TDCB) is a high-density (10 layers printed circuit) mezzanine daughter-card for the TEL62 carrier motherboard, designed in Pisa for precision time measurements. The board design (see figure 3.4) was driven by the desire to integrate a high number of channels within the same processing board, in order to ease triggering issues [85]. The desire for a compact and common electronics and the short distance (order of meters) between subdetectors and readout electronics, with no space constraints, led to the choice of having digitizers on the readout board rather than on the detector thus leaving only analog front-end electronics on each individual subdetector in a potentially higher radiation environment and making all digital electronics common and located on the same boards, at the price of having to transmit analog pulses on the 5 m LVDS cables between the two.

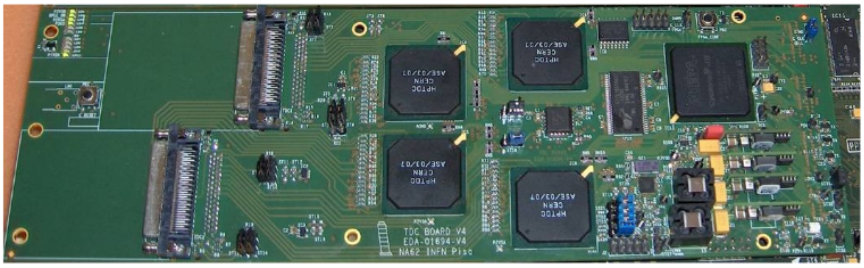

Figure 3.4: The TDC Board.

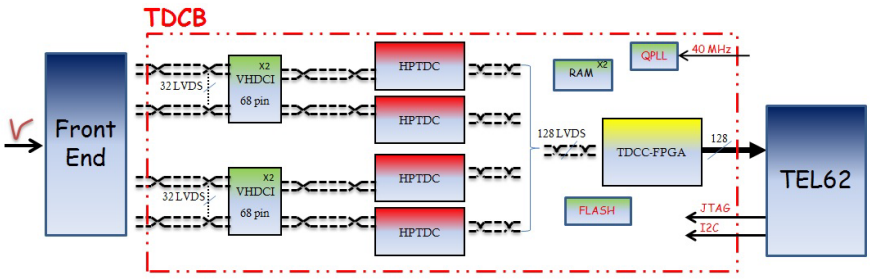

Figure 3.5: Schematic view of the TDCB architecture.

The requirements of a good time resolution and high channel integration led to the choice of the CERN High Performance Time to Digital Converter (HPTDC)[49] as time digitizers (see figure 3.5).

With a fast front-end electronics providing adequately time-stretched LVDS discriminated pulses, the measurement of both the leading and trailing edge times allows obtaining analog pulse-height information by the time-over-threshold method: HPTDCs can indeed digitize the time of occurrence of both signal edges, provided they are separated by a minimum time (about 7 ns); the resulting time measurements (made with respect to clock edges) can be combined into a single word to reduce the required data bandwidth.

The board houses four 68-pin VHDCI connectors for input signals, each of them delivering 32 LVDS signals to one TDC, with two spare pairs being used to provide additional grounding (one pair) and to allow user-defined back communication from the TDCB to the front-end electronics (one pair). This latter feature can be used to trigger the injection of calibration pulses in the subdetector or calibration patterns in the front-end (as two single-ended lines allowing bidirectional communication, or as a LVDS pair towards the front-end). This choice allows in principle the use of high-performance cables, if required by the intrinsic resolution of a subdetector, as well as cheaper solutions.

The TDCB houses a dedicated Altera®Cyclone®III EP3C120 FPGA [9], named TDC Controller (TDCC-FPGA) which can handle the configuration of the four HPTDCs via JTAG, read the data they collect, and possibly pre-process it. A 2 MB external static RAM block is also available and will be used for online data monitoring purposes and low-level checks on data quality.

The TDCC-FPGA can be configured from an on-board flash memory (Altera®EPCS64 [12]), which can be loaded using an external programmer via an on-board connector or through JTAG, either using a JTAG port on the TEL62

board, or through its Credit Card PC (CCPC). Communication between each TEL62 FPGA and the corresponding TDCC-FPGA on the daughter-board proceeds through a 200-pin connector with 4 independent 32-bit single-ended LVTTL parallel data buses (one for each TDC, running at 40 MHz, for a total bandwidth of about 5 Gbit/s) and a few dedicated lines for synchronous commands and resets. The TDCC-FPGA on the TDC daughter-card can also be accessed from the TEL62 CCPC card via a dedicated I2C connection for slow operations.

The individual TDCs are configured via JTAG, with the TDCC-FPGA acting as the JTAG master: the configuration bits are sent to the TDCC-FPGA from the TEL62 CCPC card via I2C, and are then uploaded to the TDCs. A second working mode allows inserting both the TDCC-FPGA and the four HPTDCs into a global JTAG chain which also includes all the TEL62's devices, and which can be driven by the TEL62 CCPC card.

The contribution of the digitizing system to the time resolution ultimately depends on the random jitter of the reference clock against which the measurement is performed. The 40 MHz clock optically distributed by the TTC is received through the TEL62 and is cleaned by the on-board QPLL [81] to reduce the jitter below 50 ps. This clock signal drives the internal logic and is distributed to each TDCB, where it can be configured to go through more jitter-cleaning stages: these are the internal PLL of the TDCC-FPGA and a second on-board QPLL.

3.5.1 HPTDC

The HPTDC[49] can work in an un-triggered mode, in which all available data is delivered at every readout request, or in a trigger-matching mode, in which a readout request follows a trigger pulse, and the TDC only delivers the data which matches in time the trigger occurrence, within some programmable time windows. Trigger-matching mode was implemented to allow HPTDCs to work as front-end buffers, storing data in a buffer (called L1 buffer, but have no relation to the NA62 L1 trigger) while a trigger signal was generated (see figure 3.6); however, in a modern experiment such as NA62, the latency of the lowest trigger level (1 ms) is much longer than the typical time it takes to fill TDCs' buffers (order of tens of μs in our experiment). The TDCBs therefore normally use TDCs in trigger-matching mode just as a way of obtaining properly time-framed data, but triggers are actually sent to HPTDCs in a continuous periodic stream, with no relation whatsoever to the trigger of the experiment (data storage during trigger latency being actually provided on the carrier TEL62 board with much larger buffers). The time-matching parameters in the TDCs have to be properly set in order to allow readout of all hits which occurred since the previous trigger (time-matching window set equal to trigger period): in this way the TDCs are periodically triggered and readout, receiving all hits corresponding to a time frame of length equal to the triggering period, in a continuous sequence. Since the range of time measurement within the TDC chips is limited (to 51.2 μs at most), and therefore a roll-over of the TDC time word frequently occurs, only by exploiting this working mode one can be guaranteed (by the TDCs themselves) that all the data are being read.

Each HPTDC provides 32 TDC channels when operated in fully digital mode

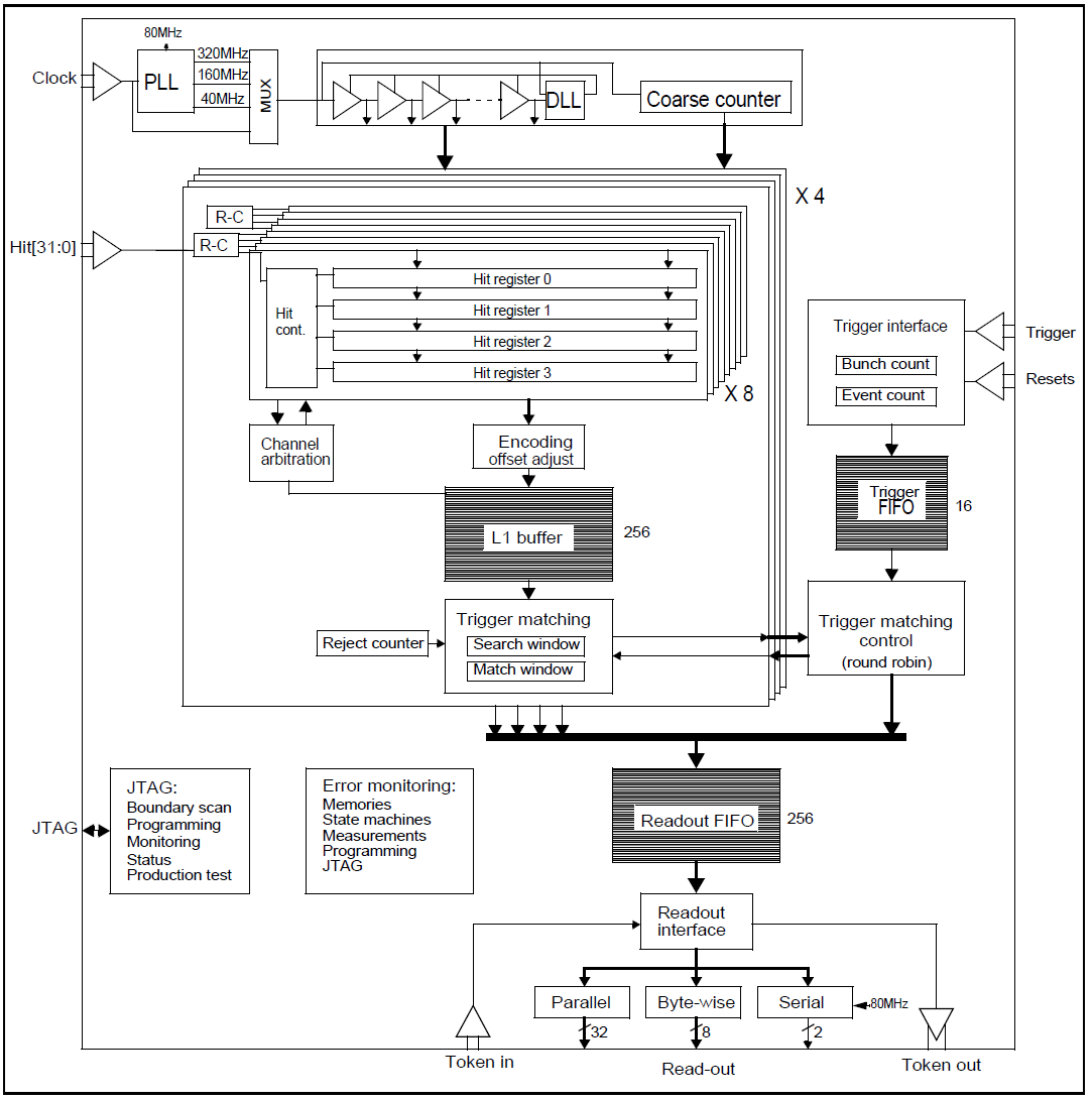

Figure 3.6: Schematic view of the HPTDC architecture. The input for the TDC from the subdetector front-end electronics are at the top left and are called Hit[31:0]. At the bottom there are the link (called in the scheme Read-out) with the TDCC-FPGA.

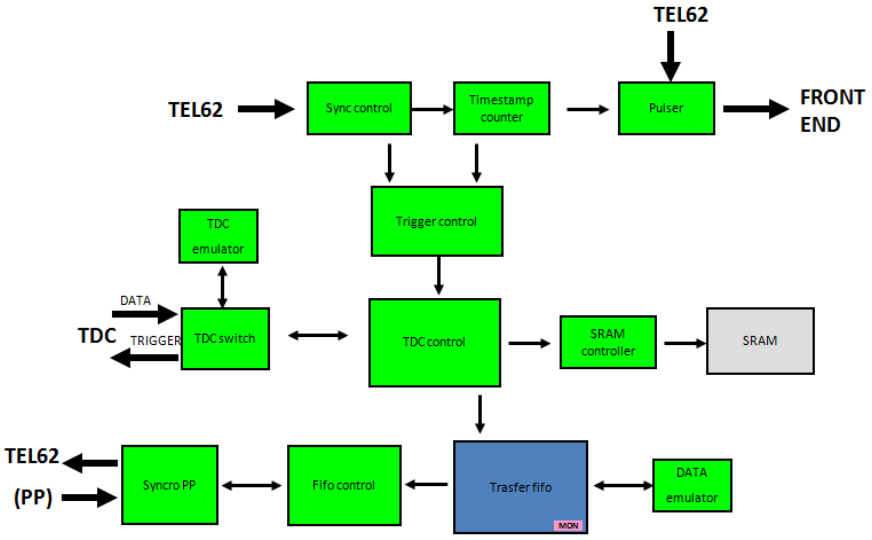

Figure 3.7: Block diagram of the TDCC-FPGA firmware.

at 98 ps LSB resolution, with some internal buffering for multi-hit capability and a trigger-matching logic allowing the extraction of hits in selected time windows. Four such chips, for a total of 128 channels, are mounted on each TDCB, resulting in a grand total of 512 TDC channels per fully-equipped TEL62 carrier-board; as an example, the entire RICH detector can be handled by 4 TEL62 boards only, while most small subdetectors only require a single TEL62 board.

3.5.2 The TDCC-FPGA firmware

We used the software tools HDL Designer®[60], Modelsim®[61] (from Mentor Graphics®) and Quartus®II[11] (from Altera®) to develop the firmware for the TDC Board's TDCC-FPGA (and for the FPGAs of the TEL62 carrier-board). The main TDCC-FPGA firmware[64] parts and functionalities are shown in a block diagram in figure 3.7.

To have a good resolution for the time measurement we have chosen a TDC configuration, in which the chip produces two 32 bit-long words for each signal, one word for the leading and one for the trailing edge. The number of bits dedicated to time measurement are 19 out of 32, the other being used identify the channel (5 bits), the TDC inside the board (4 bits) and the type of data word (4 bits). The possible types of words are 5: leading or trailing edge, error words and TDC frame timestamps and word counters. Inside the FPGA the data are are packed in 6.4 μs frame, each frame have a header word (TDC frame timestamps) and a trailer word (word counters).

The TDCC-FPGA firmware performs several operations:

- **Packing the data stream from the TDCs.** The TDCC-FPGA receives the data sent by the HPTDCs through a 32-bit parallel block writing protocol. The TDC time measurement rolls over every 51.2 μs, while the SPS spill is several seconds long. To cope with these different time scales, in the *TDC control* block we add a timestamp to the data in such a way that

the TDC time measurement is unambiguously associated to an "absolute" time for the whole length of the spill. This is achieved by periodically triggering the TDCs with a period shorter than the TDC's roll-over (we chose a period of 6.4 μs) and adding a frame timestamp at the beginning of the data stream associated with each frame. Then at the end of the frame data stream we add a word counter indicating the number of words received by the TDC plus the frame timestamp itself. The roll-over of the frame timestamp (whose least significant bits corresponds to 400 ns) is $2^{28} \times 400\text{ns} \approx 107$ s, much longer than the SPS spill duration.

In the *TDC control* block 2, of the 4 bits that identify the TDC inside the board, are replaced with 2 parity bits. These parity bit are useful to verify if the data were altered (e.g. corruption or bit-flips) during the data flow. A mathematical function returns a 2 bits result for each data word (usually a the XOR of the data word bits); these 2 bits can be checked off-line to test the integrity of the each data word.

- **Configuring TDCs and communicating with the CCPC on the motherboard.** As mentioned before, configuration data is sent to the TDCB from the CCPC on the TEL62 through I2C. An I2C slave controller has been implemented in the firmware, through which internal registers are both written and read. A JTAG master controller is implemented in the TDCC-FPGA to transmit and receive the configuration to and from the TDC chips.

- **HPTDC emulator.** Two different HPTDC emulators are contained in the TDCB firmware: one was developed to send some simple repeating pattern on selected TDC channels (called *single-channel TDC emulator*), the other allows to load some amount of data words from a file into memory and repeatedly send it (called *data emulator*).

  The *data emulator* generates data packets containing a variable number of words per frame as required by the user, sending one data packet for each frame to which the header (timestamp) and trailer (word count) are automatically added; This emulator is directly linked to the TDCC output FIFO (called *transfer FIFO*). The data words are read from four (one for each TDC) 32-bit wide and 1 K deep pattern memories and modified so that the upper bits of the TDC time field do match the current frame timestamp (so the data words will not repeat exactly). The *data emulator* read from the memory and puts in each frame a number of words as read from a 9-bit wide and 1 K deep count memory (0 value in a line of this memory will generate an empty frame with only the header and the trailer). It is even possible to set the *data emulator* to repeat the same sequence continuously. The *data emulator* is used to test parts of the firmware of the TDCB or of the TEL62, using patterns written ad hoc to stress the firmware and the electronics, such ad the TEL62 output links.

- **The on-board RAM.** The data stream can be optionally split and sent to the TDCB's on-board static RAM during the acquisition, to possibly store

a fraction of it for reading it and analysing it off-line. This can be useful for debugging or monitoring purposes. The RAM space is equally subdivided among the four TDCs. In the final implementation, it will be possible to choose between filling the RAM with the data from the first part of the spill, the last one or only with the frames that exceed same defined rate.

- **Front-end pulser.** The TDCC-FPGA can drive a spare output LVDS pair of the TDC connector, that allows to trigger the front-end boards for sub-detectors' calibration. Some front-end boards can send data signals to the TDCs in response to that stimulusS: this is useful for debugging purposes and to test the hardware connections. The *Front-end pulser* is driven by a mask register which is compared with a timestamp counter. An alternative working mode generates the output signal when the TDCC receives a special command from the motherboard.

3.5.3 TDCB test

Once the TDCB design was finalized various tests were performed in order to verify that the system complies with the experiment's requirements. These tests were performed in the laboratory of Pisa INFN, using a test setup which may reproduce conditions similar to the experiment environment, and at CERN during a test beam[85].

Time resolution

An important figure is the intrinsic contribution of the board to the time resolution. It was evaluated in the laboratory by pulsing TDC channels with signals of fixed duration generated by an FPGA-based test board working on the same clock used by the TDCB, and by measuring the time differences between the trailing and leading times of a LVDS pulse with nominal 25 ns duration. In a first test we pulsed 32 TDC channels at a time: we observed that the RMS of the measured pulse width on a single channel was 61 ps (figure 3.8 left) and the average was 25.18 ns on a sample of 10^5 pulses. In a second test we pulsed simultaneously only 1 every 4 TDC channels (8 in total) with the same signals of the previous case (figure 3.8 right) and found comparable results.

No spurious hits were detected on channels which were not pulsed, over a sample of 10^7 events. We checked other possible cross-talk effects by comparing the channel time resolution in the previous two tests: all the 32 TDC channels pulsed with signals of constant width (25 ns) or only 8 TDC channels (1 every 4) pulsed. We didn't observe differences in the time resolution (see figure3.8) when other channels were pulsed, concluding that no significant cross talk effects are present.

Channel efficiency

Hit losses are expected at high rates due to the limited amount of buffering present in the HPTDC. In the HPTDC the 32 channels are divided in four independent groups of 8 channels each, and hits are buffered at different stages: per channel,

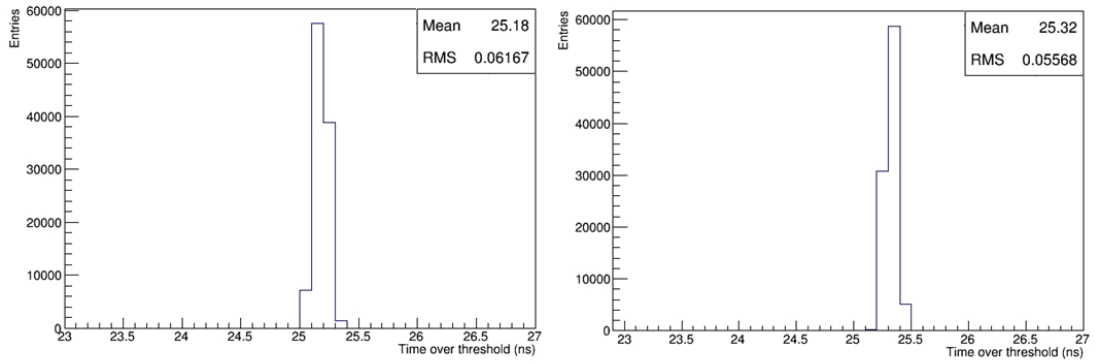

Figure 3.8: Distribution of times-over-threshold for digital 25 ns wide signals as measured by the TDCB, with 32 channels pulsed (left) and 8 channels pulsed (right).

per group of 8 channels, per full chip (respectively Hit registers, L1 buffer and Readout FIFO in figure 3.5); apart from the first buffering stage, the other ones are monitored for overflow conditions.

The data transfer efficiency is defined as the ratio between the number of hits delivered by the system and the number of input pulses. It was measured in the laboratory both using only one single channel (1 of every group of 8 for a total of 4 TDC channels) and using two neighbouring channels (channels 0 and 1 of every group of 8 for a total of 8 TDC channels). We use these configurations because inside the HPTDC every group of 8 channels shared a 256 words deep level 1 buffer [49]. When several hits are waiting to be written inside the level 1 buffer an arbitration between pending requests is performed. Arbitration between channels in the active request queue is done with a simple hard-wired priority (channel 0 highest priority, channel 7 lowest priority). In this way the first channels in each group of 8 are serviced faster than the last ones. At high rates this gives an advantage to the low-numbered high-priority channels which can use their channel de-randomizers more efficiently, while in such conditions lower-priority channels appear like they have smaller de-randomizing capability and therefore slightly higher data losses. The results of the measurement and different channels efficiency are shown in figure 3.9.

No data losses were observed for input rates below 17.5 MHz in the first case (single channel). In the case of two adjacent channels being pulsed, no data losses were observed for input rates below 8.5 MHz per channel; above such value data losses start to appear at slightly different levels depending on the pulsed channel.

Test beam results

In November and December 2012 a test run with beam was performed at the CERN SPS. The main measurements performed during of this test run were the response of the detector and the front-end, the rates and efficiencies of the detectors and the TDAQ system, the time and space correlations between the detectors. The setup in the test beam was similar to the experiment, with the

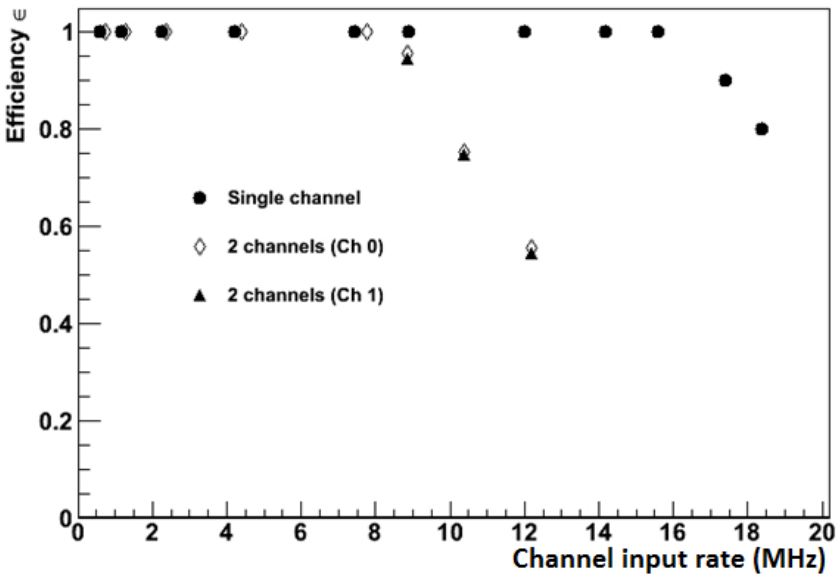

Figure 3.9: TDCB hits efficiency pulsing one and two channels.

secondary kaon beam of 75 GeV/c produced by protons from the SPS. The test was carried out with a low intensity beam (1/50 of nominal rate foreseen for NA62). Figure 3.10 shows the event time difference distribution between the fast and high-resolution detectors CHOD and CEDAR, which had a fitted standard deviation of 410 ps. This value is compatible with the intrinsic detector resolutions, confirming a negligible contribution from the electronics and the read-out board.

Run 2014

During the 2014 Run it became evident that, even at low beam intensities (about ~ 12 % of the nominal), intensity peaks are present in the beam time structure. These peaks can reach and exceed the DAQ design limit (~ 39 Mword per second per TDC) and the initial version of the firmware was not able to sustain this rate. We measured a firmware limit of ~ 34 Mword per second per TDC and when this limit was reached the TDC board was not able to recover smoothly. So we made some improvements to the firmware to reach the design limit and prevent failures when this limit is exceeded. A reshaping of the *TDC control* block allowed to reach the limit of ~ 39 Mword per second per TDC and the addition of two new blocks gave the possibility of managing the data frame when the limit is surpassed. This two blocks (which can be enabled via registers) approach the problem in different way:

- **Data limiter** This block limits the number of words written in TDCC output FIFO for a single frame. The maximum value is set by a register; any words (excluding header and trailer) exceeding such value are thrown away, an error word is inserted in the frame and the frame is completed with the correct word count.

- **Data suppressor** When this block is active and one of the input FIFOs

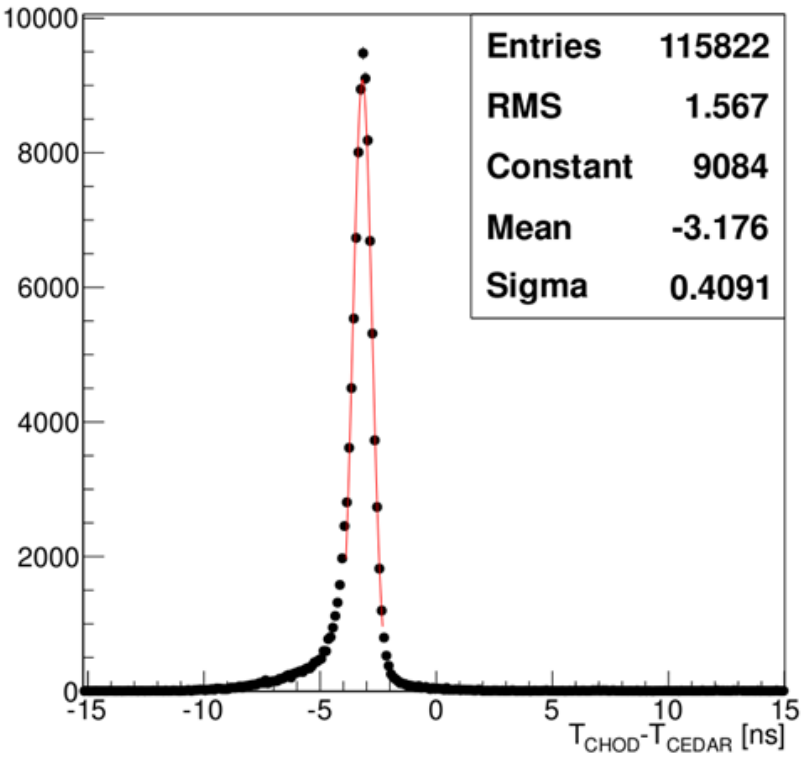

Figure 3.10: Distribution of event time differences between CHOD and CEDAR detectors (2012 test beam).

storing TDC data becomes almost full (at a pre-defined level), further data from TDCs will be ignored (although TDCs are still read) and an error word is written into the FIFO until the filling of both such input FIFOs falls below a (lower) threshold.

Using either of this two blocks we are able to prevent blocking failures in the TDC Board.

3.6 The TEL62 board

The TEL62 board (see figure 3.11) is the common multi-purpose FPGA-based motherboard [88][17]; it is used in the NA62 experiment both for trigger primitive generation and for data acquisition. It is used by several NA62 detectors with a total number of about 100 installed card.

This board has been developed in Pisa and it is a highly-improved version of the TELL1 board designed by EPFL Lausanne for the LHCb experiment at CERN [65]. The design exhibits a similar overall architecture, but the board is based on much more powerful and modem devices, resulting in more than eight times the computation power and more than twenty times the buffer memory of the original, plus several other improvements in terms of connectivity.

While a large number of TEL62 board are used for the implementation of the calorimetric trigger (see section 4.3.1), we mostly focus here on their use when equipped with TDCB boards.

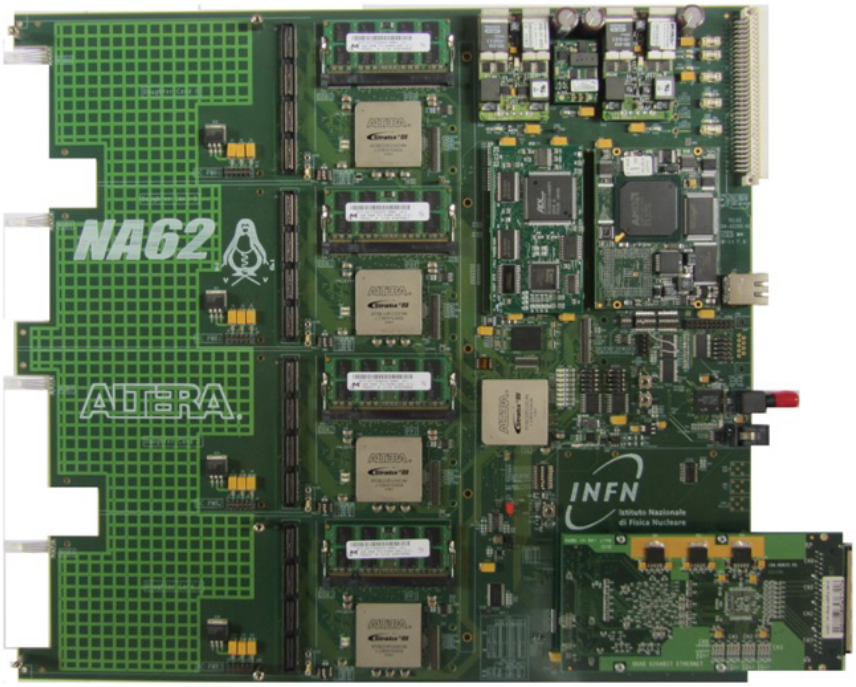

Figure 3.11: The TEL62 motherboard.

The TEL62 is a standard 9U Eurocard, with a 16 layers printed circuit with all lines impedance (50Ω) controlled and the clock tree routing done with special care to avoid introducing signal jitter. This motherboard can handle up to 4 mezzanines (like the TDCB), for a total of 512 input channels and houses 5 FPGA of the same type. The 4 *Pre-Processing* (PP) FPGAs are connected to a single *Sync-Link* (SL) FPGA; each PP is directly connected to one of the TDCB mezzanine (see figure 3.12). Depending on the subdetector, the TDCs can send an amount of data up to some tens of MB/s per channels. Data are organized in packets, each one related to time frames of 6.4 μs duration. The 4 PP-FPGAs have the role of collecting and merging the data and later organizing them on the fly in a 2 GB DDR2 memory, where each time *slot* corresponds to a single 25 ns time window. Data are stored in the DDR2 memory waiting for a L0 trigger request; at the trigger arrival, the data within a programmable number of 25 ns time windows around the trigger timestamp are read from the DDR2, packed and sent to the SL-FPGA. In the SL-FPGA, the data from the 4 PP are merged, synchronized and stored in a 1 MB QDR SDRAM temporary buffer. Later, the data are extracted for formatting into Ethernet data packets and sent through 4 Gigabit Ethernet links hosted on a custom daughter-card to a computer farm. The board can sustain, by design, 1 MHz of L0 trigger rate for standard-size events.

The fundamental components of the board (see figure 3.13) are shown below:

- The 4 PP FPGA are Altera®Stratix®III FPGAs EP3SL200F1152 [13], each one containing an embedded memory of 9396 kbit and 198 900 equivalent logic elements. Each PP elaborates the data from the 4 TDCs of one

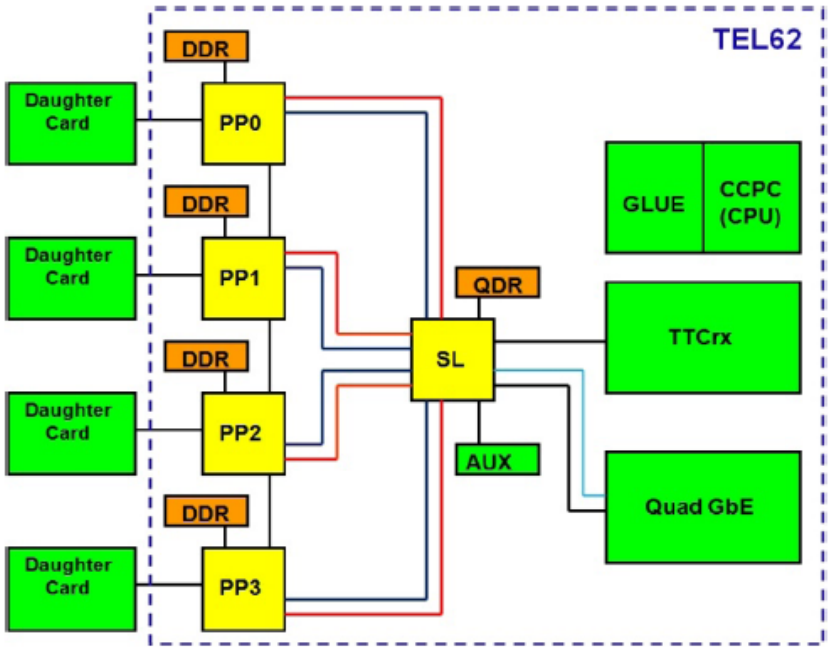

Figure 3.12: Layout of the TEL62 board architecture. FPGAs are shown in yellow, memory buffers in orange, other chip and daughter-card connectors are in green. Lines represent data bus links between devices.

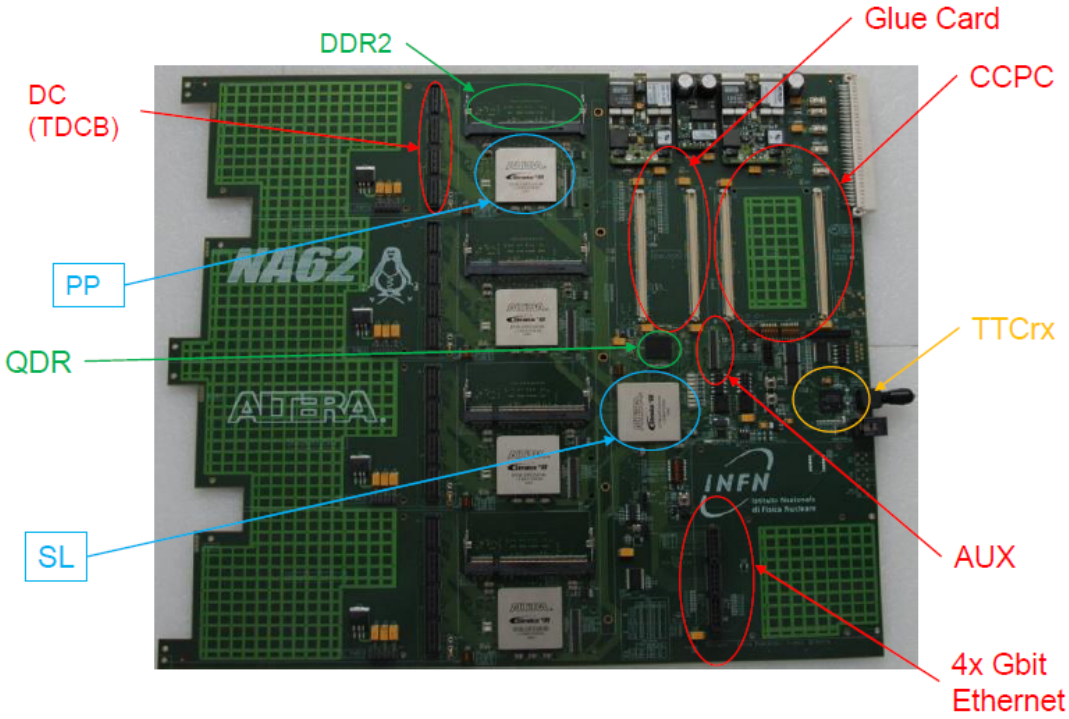

Figure 3.13: Main components of the TEL62.

TDCB that is connected through a 200-pin connector, using 4 32-bit wide data buses. Each bus transmits data from one TDC, at 40 MHz for a total bandwidth of about 5 Gbit/s. Each PP is also linked to a DDR2 memory buffer of 2 GB with a 64 bit bus with a clock frequency of 640 MHz, resulting in a memory bandwidth of $\sim$ 41 Gbit/s. Furthermore the 4 FPGA are interconnected in a row (see figure 3.12) with 2 x 16 bit buses (input and output).

- The SL FPGA is also an Altera®Stratix®III FPGAs EP3SL200F1152 [13] with the same hardware characteristics of the PP-FPGA. It is connected to each of the 4 PPs through two independent data and trigger primitives buses, 32 bits wide and operating at a clock frequency of 160 MHz, for a total bandwidth of about 10 Gbit/s per connection. All signal lines are properly terminated and equalized in length to handle this clock speed; moreover we added in the firmware a set of time constraints to guarantee the functionalities of the board. The SL-FPGA is linked to a Quad Data Rate (QDR) Synchronous Pipelined Burst SRAM of 1 MB, read and written at 120 MHz clock frequency and used like temporary buffer in the data flow. The data packets generated in the SL are sent to a custom Gigabit Ethernet (GbE) mezzanine.

- The custom mezzanine is a Quad GbE [82] (the same card used in the TELL1); this card hosts four 1 Gbit Ethernet channels used to send data packets to the PC farm, trigger primitives to the L0 Trigger Processor (L0TP) or data packets to other TEL62s in a daisy chain configuration.

- A standard optical TTC link distributes the main 40 MHz clock and the L0 triggers, which are then decoded by a TTCrx chip[8].

- An on-board QPLL [81] reduces the signal jitter of the input clock to few tens of ps.

- A commercial Credit Card PC (CCPC)[74] is a SM520PC SmartModule produced by Digital-Logic, Inc. running a Scientific Linux operating system mounted from an external CCPC boot server through a dedicated Ethernet link, and a custom input/output interface card named Glue card[55] (same as in the TELL1 board) handle the slow control, the monitoring and the configuration of the TEL62. These two mezzanine cards communicate among them through PCI buses. The Glue card use and distribute to the other devices and connectors three different communication protocols: ECS is a custom parallel bus used to configure or read the FPGAs' internal registers and to control or monitor the board functionalities, I2C is used to control the TDC Board and JTAG allows to configure and program remotely the FPGAs on the TEL62 and on the mezzanines, by loading the firmware on the respective EEPROMs.

- Two 64 Mbit EEPROMs (Altera®EPCS64[12]), one for the 4 PPs and one for the SL, store the FPGA configurations.

- Dedicated auxiliary connectors with two independent 16-bit buses allow to link several TEL62 in a daisy chain: it could be useful to merge the L0 trigger primitives from different TEL62 of a single detector and to use only one Gigabit link, to send them to the L0TP.

3.6.1 The TEL62 firmware

Like for the TDCB, we use HDL Designer®, Modelsim®and Quartus®II to develop the firmware of the PP-FPGAs and the SL-FPGA.

The PP-FPGAs

All the 4 PP-FPGAs use the same firmware, which can be divided in 4 parts: the data flow upstream the DDR (inside the red square in figure 3.14), the one downstream the DDR (inside the blue square in figure 3.14), the trigger primitive flow (inside the green square in figure 3.14) and the part related to testing of the FPGA and the connections (inside the brown squares in figure 3.14).

The upstream data flow. The PP-FPGA receives the data from four buses linked to the TDCB mezzanine card (one per TDC). Each bus fills a dedicated derandomizer IB (Input Buffer) FIFO with a clock frequency of 40 MHz. The data from the TDCB are packed in 6.4 μs data frames. The OB (Output Buffer) block merges, at 160 MHz, data of frames with the same timestamp from the 4 IB buffers; a bigger frame containing all the hits of the daughter-card is created, and is stored in two copies of the Output Buffer (OB) FIFO, one of them reserved used form monitoring purposes. Then the data packets are compressed to be stored inside the DDR2 memory. This is the most complex part of the firmware, indeed it has been the subject of two important revisions during the evolution of the firmware itself. The difficulty consists in packing the data in order to minimize the number of accesses to the DDR2. Each access requires a relatively large time (3 clock cycles for a write access and 33 clock cycle for a read access) that could slow down the data flow; we have to maximize the time efficiency of DDR2 writing and reading operations because the structure must sustain an input data flow of 160 Mword per second and a trigger rate of 1 MHz. The first version (V1) of the firmware organized the data of each 6.4 μs frame in fixed-size area related to 25 ns time slots, for a total of 256 slots. Each time slot was reserved a memory amount equal to 128 x 32-bit words, so each frame required 1 Mbit of memory. We implemented two of these memories to avoid interruptions in the data flow: while one memory was written by the Data Organizer, the other was read by the DDR writer. We reserved 128 words per 25 ns time slot, as a compromise between the need to sustain high instantaneous rates (i.e. up to 2.56 GHz of hit) and the available memory in the FPGA (2 Mbit is about a quarter of the total memory). Half of the DDR2 (1 GB) was reserved for memory data storage and half was used for 8-bit counters, that indicated the actual number of words of each time slot. In the second half of the DDR, the counters were organized 8 DDR locations of 256 bit (16 counters per location) per a frame. The use of data counters optimized the DDR reading because only the relevant part of each time

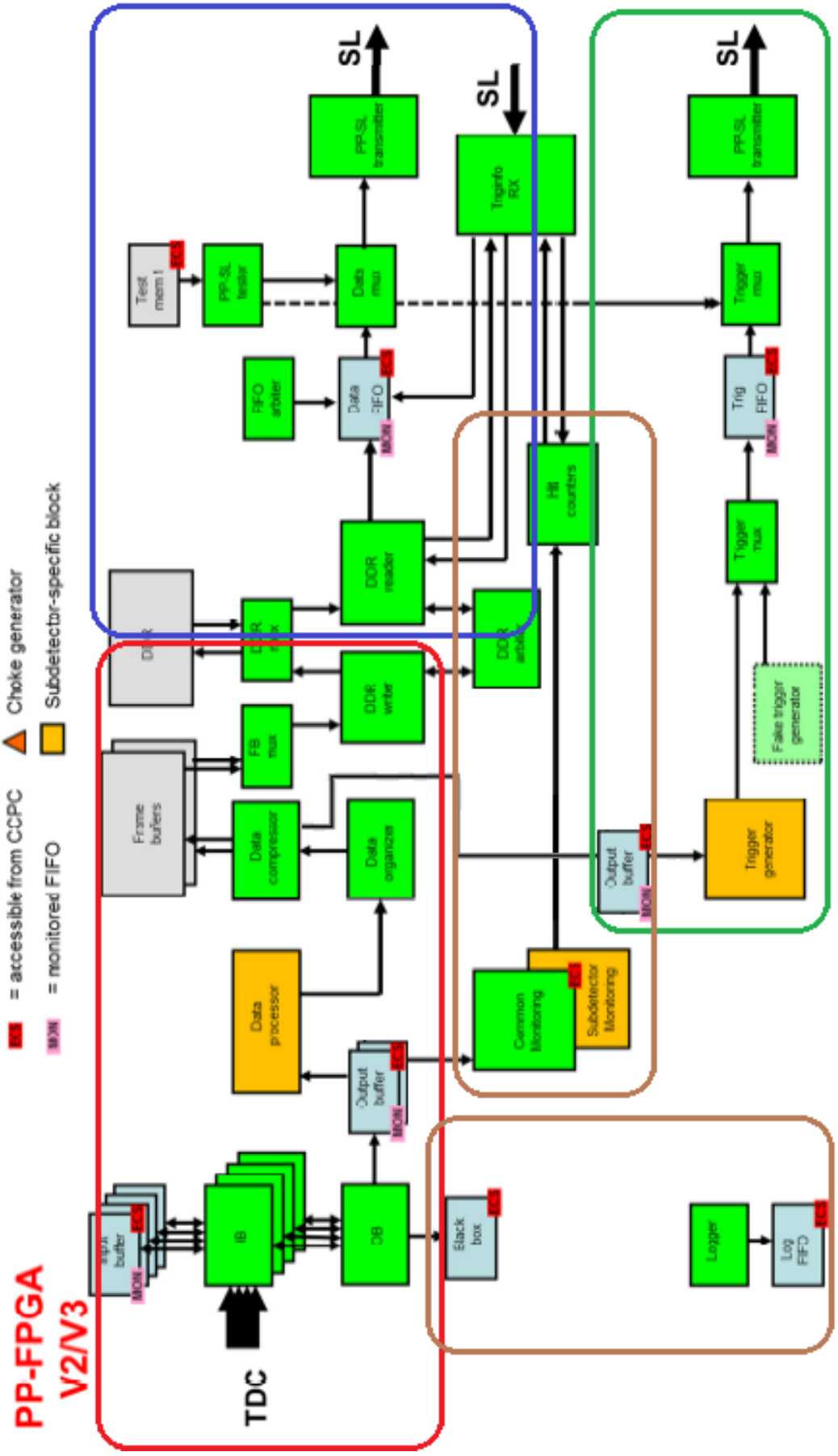

Figure 3.14: Block diagram of the PP-FPGA firmware version 3.

slot was read. These numbers defined the maximum latency of the system, that is the time after that data is overwritten (and lost if a L0 trigger did not arrive).

$$\frac{1\,\mathrm{GB}}{1\,\mathrm{Mbit}\,/\,6.4\,\mu\mathrm{s}} = \frac{8\,\mathrm{Gb}}{1\,\mathrm{Mbit}\,/\,6.4\,\mu\mathrm{s}} = 51.2\,\mathrm{ms}$$

At L0 trigger arrival, a module, the *DDR reader*, read up to three 25 ns slots of data in a single access and packed the data to send them to the SL-FPGA.

After some test we realized that this data organization presented some problem at high trigger rate: the *DDR writer* needed 257 accesses (256 time slots + the counter part) to write one frame and the *DDR reader* module had to perform 2 memory accesses (counter + data) for each trigger. The DDR2 access latency for a write operation is 3 clock cycles (the clock period is 6.25 ns) and it needs 1 clock further cycle per DDR line (8 words of a timeslot) to be written. So for each 6.4 μs frame the total write time was:

$$all\,slots\,empty\ :\ (3\ \times\ 257\ +\ 8\,)\ \times\ 6.25\,\mathrm{ns}\ \sim\ 5\,\mu\mathrm{s}$$

$$design\,rate\,(160\,MHz\,words)\ :\ (3\ \times\ 257\ +\ 256\,)\ \times\ 6.25\,\mathrm{ns}\ \sim\ 6.4\,\mu\mathrm{s}$$

$$all\,slots\,completely\,full\ :\ (3\ \times\ 257\ +\ 4096\,)\ \times\ 6.25\,\mathrm{ns}\ \sim\ 30\,\mu\mathrm{s}$$

The DDR2 access latency for a read operation is 33 clock cycles and it has to read 49 lines (16 line per 3 slot to read the data and 1 line to read the counters). The total read time for a trigger was:

$$empty\,slot\ :\ (33\ +\ 1\,)\ \times\ 6.25\,\mathrm{ns}\ \sim\ 0.2\,\mu\mathrm{s}$$

$$design\,rate\,(160\,MHz\,word)\ :\ (33\ \times\ 3\ +\ 49\,)\ \times\ 6.25\,\mathrm{ns}\ \sim\ 0.9\,\mu\mathrm{s}$$

$$slot\,not\,empty\ :\ (33\ \times\ 3\ +\ 49\,)\ \times\ 6.25\,\mathrm{ns}\ \sim\ 0.9\,\mu\mathrm{s}$$

These values were not compatible with the design trigger rate limit of 1 MHz. Indeed at 1 MHz of trigger rate, the time to write and read an empty frame should be about 6.3 μs (5 μs to write an empty frame and 0.2 μs $\times$ 6.4 trigger in average) that is almost all the available time (6.4 μs) without considering the DDR refresh time and other operation latencies. The L0 trigger limit measured for this first version was about 700 KHz of triggers with empty events (the limit decreased with non-empty events). Another problem of this firmware version was the limited number of slots that could be read for each trigger, because some detectors (for example the LAV) need more than 3 slots to measure the hit time over threshold.

For these reasons we developed a second version of time DDR data organization. We introduced a new block, the *data compressor* (see figure 3.15), to better pack the data frame. In this version, each 25 ns time slot is not allocated a pre-defined space: data was written in adjacent 256 DDR locations with flags pointing to the end of the slot. The memory space allocated for a frame remained the same as in the previous version (1 Mbit for 6.4 μs) but the second area of the DDR2 now contained 8-bit addresses instead of counters. The addresses, related to a time slot, represented the starting address of the next non-empty slot in the DDR2 data area. Figure 3.16 shows an example of the compressor output for a

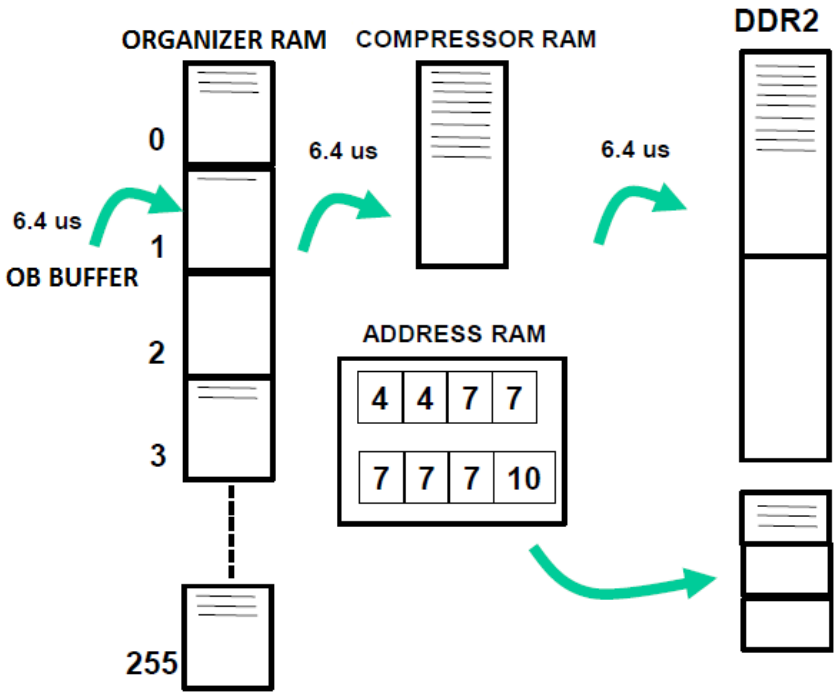

Figure 3.15: Layout of the second version of DDR organization.

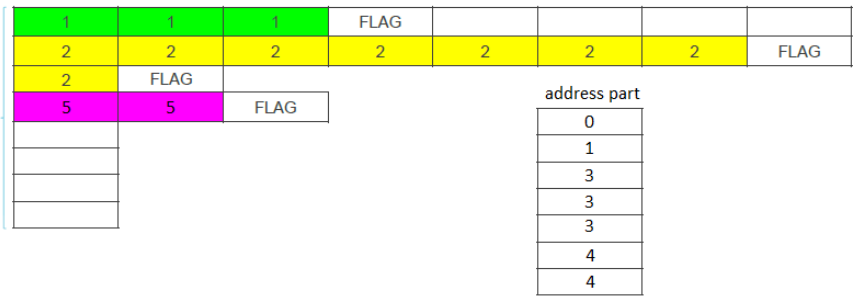

Figure 3.16: Example of data distribution in the DDR2 for a frame with 3 not empty slots, firmware version 2.

frame with 3 non-empty time slots: slot 1 has 3 data words, slot 2 has 9 words and slot 5 has 2 words; slot 0 is empty so the address of the next non-empty slot is 0, instead for slot 2 the next slot address is 3.

This version resulted in a vast improvement because the *DDR writer* block needed only one access to write all the data part and one to write the address part. So for each 6.4 μs frame this version had a total write time of:

$$all\ slots\ empty\ :\ (3\ \times\ 2\ +\ 8\ )\ \times\ 6.25\,\text{ns}\ \sim\ 90\,\text{ns}$$

$$design\ rate\ (160\ MHz\ words)\ :\ (3\ \times\ 2\ +\ 128\ +\ 8\ )\ \times\ 6.25\,\text{ns}\ \sim\ 900\,\text{ns}$$

$$all\ frame\ completely\ full\ :\ (3\ \times\ 2\ +\ 256\ +\ 8\ )\ \times\ 6.25\,\text{ns}\ \sim\ 1.7\,\mu\text{s}$$

The *DDR reader* part was also improved removing 3 slots limit (in this version the limit wa 30 time slots), only 1 access and 2 reads to get all the needed addresses and only one access (in some particular cases 2 accesses) to have all the data words of the time slots triggered. The total read time for a trigger and 3 time slots was:

$$empty\ slot\ :\ (33\ +\ 1\ )\ \times\ 6.25\,\text{ns}\ \sim\ 0.2\,\mu\text{s}$$

$$design\ rate\ (160\ MHz\ word)\ :\ (33\ \times\ 2\ +\ 5\ )\ \times\ 6.25\,\text{ns}\ \sim\ 0.4\,\mu\text{s}$$

$$slot\ not\ empty\ :\ (33\ \times\ 2\ +\ 49\ )\ \times\ 6.25\,\text{ns}\ \sim\ 0.7\,\mu\text{s}$$

Version 2 was able to sustain a trigger rate of 1 MHz.

During the 2014 RUN even this version (V2) was shown to be unable to reach the required rate. The PP should be able to sustain the same rate of the TDC Board i.e. 4×39Mword/s = 156Mword/s while it reached only 116 Mword/s. This high rate could be reached even at intensities below nominal due to the highly non-uniform spill structure (see figure 3.17) that presents a 50 Hz modulation and some high peaks (see figure 3.18).

We re-designed again the core firmware of the TEL62 to obtain the (final) V3 version. To stand rate, the data had to be more compressed in the DDR and we had to remove the end-of-slot flag (it wasted 1 clock cycle per each non-empty time slot). The data words of each slot are now one after the other without empty space or flags and in the address word we added 4 bits to specify the position of the slot first data within the row (see figure 3.19). Having reached this compression, it was even possible to increase the capacity of a frame up to 4096 words compared to the 2048 of the V2.

The 2015 Run showed the design rate achievement for this firmware version.

The downstream data flow. The firmware part after the DDR2 takes care of elaborating the trigger requests from the SL-FPGA and reading the corresponding data from the DDR2. Trigger requests are received by the *Trigger Receiver* (TrigRX) block that decodes the trigger type and the trigger timestamp. The trigger type can be either physics or a special purpose one. In case of physics triggers (32 possible different types), a request is forwarded to the *DDR Reader* which starts to read a programmed number of 25 ns time slots around the trigger timestamp (the centre of these windows with respect to the trigger time can be also chosen by register). In the version 3, the firmware can extract up to 32 time

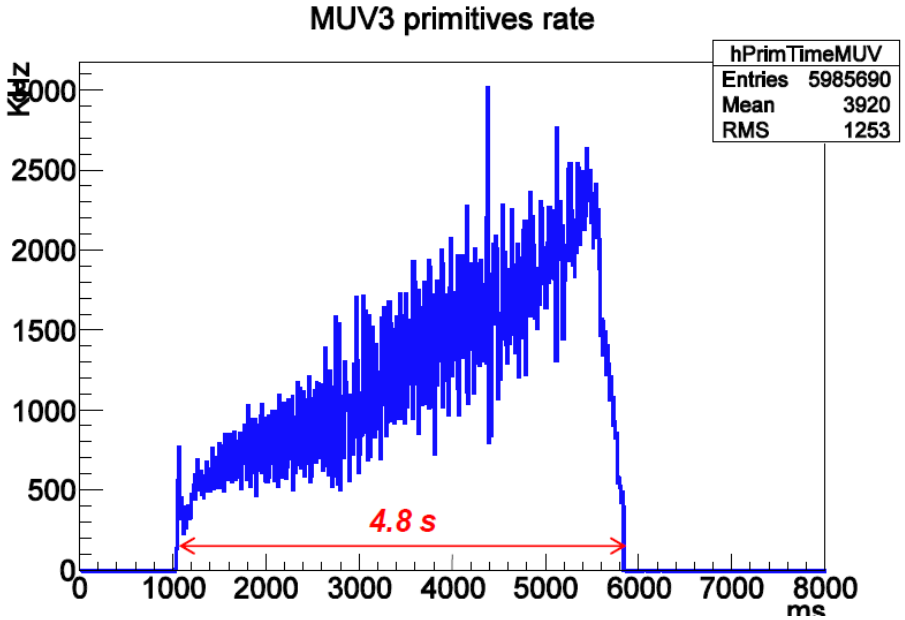

Figure 3.17: Example of burst structure.

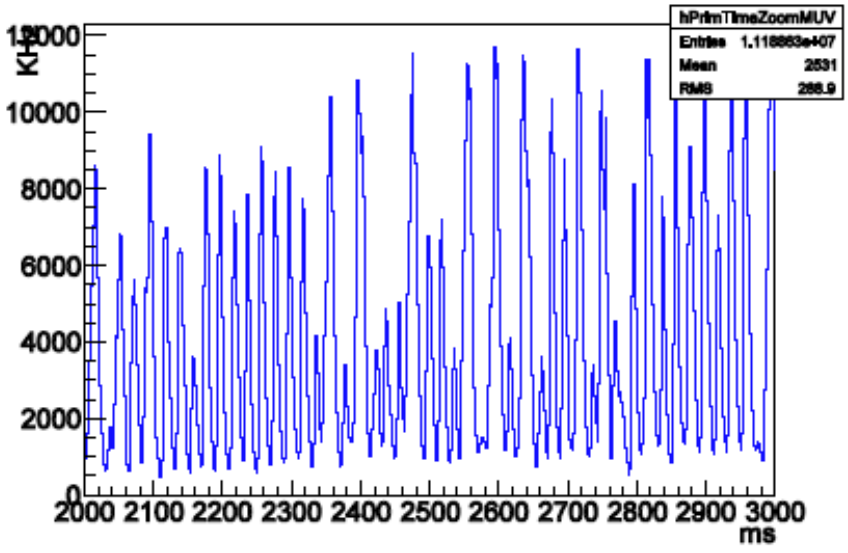

Figure 3.18: Zoom of the burst structure showing the large 50 Hz modulation and the intensity peaks.

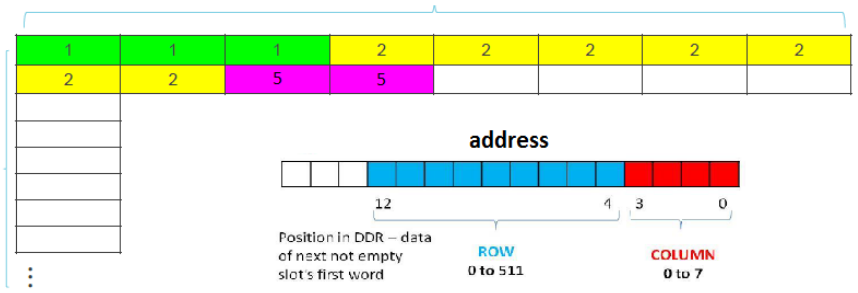

Figure 3.19: Example of data distribution in the DDR2 of a frame with 3 slot not empty, firmware version 3.

slots, for a total of 800 ns: such large window is useful to test and study the detector response. The DDR data read are stored in the *Data Output FIFO* to be transferred to the SL-FPGA.

Monitoring and testing tools. We implemented a lot of debugging and testing tools in the firmware to check its performance during the data acquisition. The CCPC can access the FPGAs via the ECS bus and read the internal registers and the status of FIFOs or memories. An useful tool is the logger system that stores in memory informations about specific error conditions, to be later checked using the CCPC. Time was dedicated to implement and optimize a tool to test the communication between PP-FPGA and TDCC-FPGA or between PP-FPGA and SL-FPGA. It's important to find a perfect coupling between the input and output lines of different FPGA, since a single error can cause some word to be misinterpreted. To test the communication system we implemented random generators using the same seed: the first sends data from the FPGA to another and the second checks the correctness of the arriving data.

Trigger primitive generation The compressor module has a second output toward a FIFO, used to provide data to trigger primitive generators. Since the FIFO is written after the organizer module, in such FIFO all the data of a 6.4 μs frame is organized in a sequence ordered of 25 ns slot. The ordering simplifies the following elaboration because it is easier to work on 25 ns slots of data to obtain more precise clusters (like 3 ns of resolution) or further data sorting. Only detectors involved in the L0 trigger developed this firmware part: RICH, CHOD, new-CHOD, MUV3, LAV12. Some firmware handles channels matching or time slewing correction (see next chapter). After primitive building, these data sent to the SL-FPGA for further processing.

The SL-FPGA

Also the SL-FPGA firmware can be divided in four parts: the trigger and data flow, the trigger primitive generation and the testing tools. Figure 3.20 shows the firmware blocks dedicated to the data flow (red square), the trigger flow (inside the blue squares) and the testing tools (inside the brown squares); figure 3.21 shows the trigger primitive generation flow.

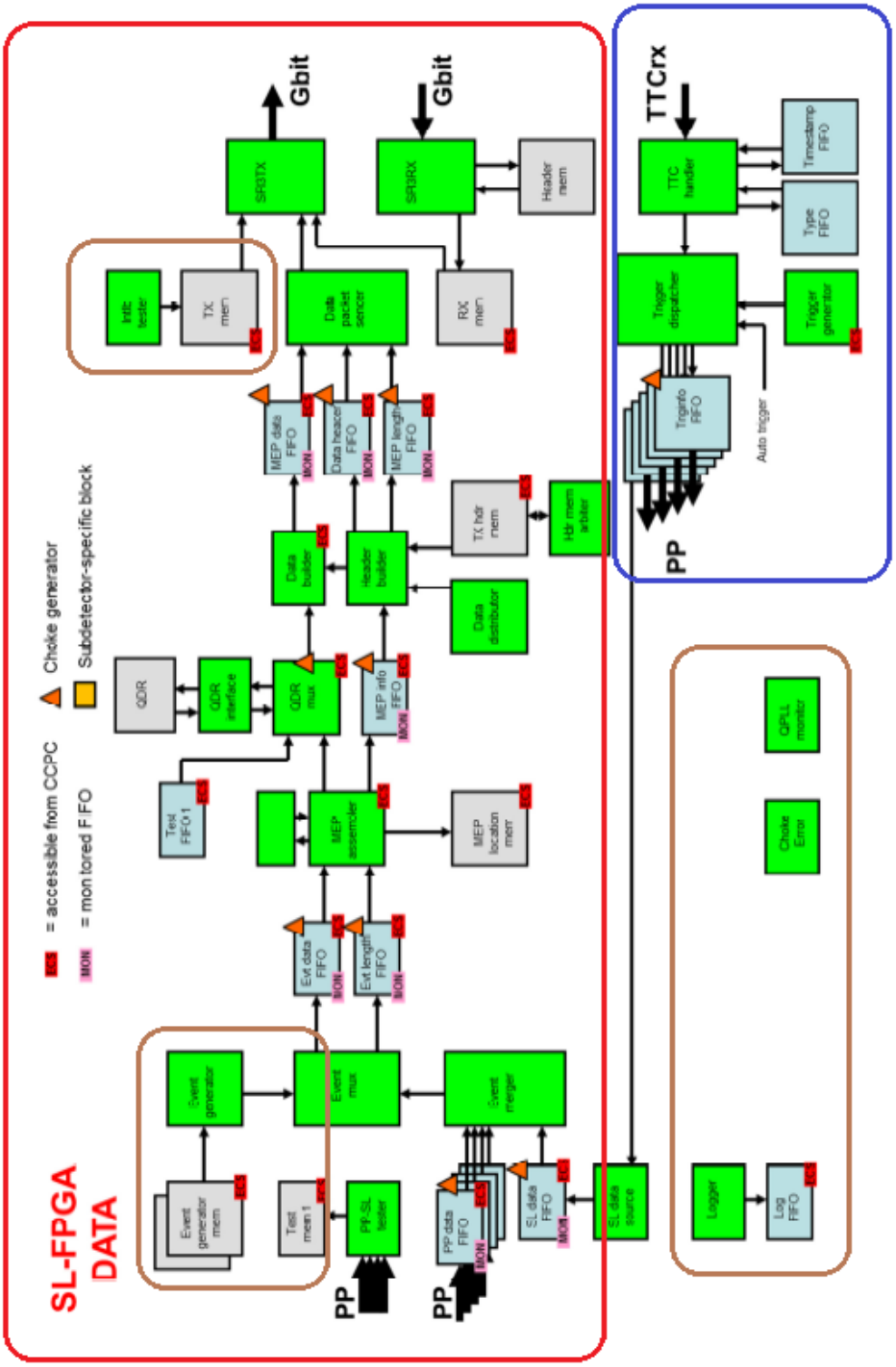

Figure 3.20: Data flow block diagram of the SL-FPGA firmware.

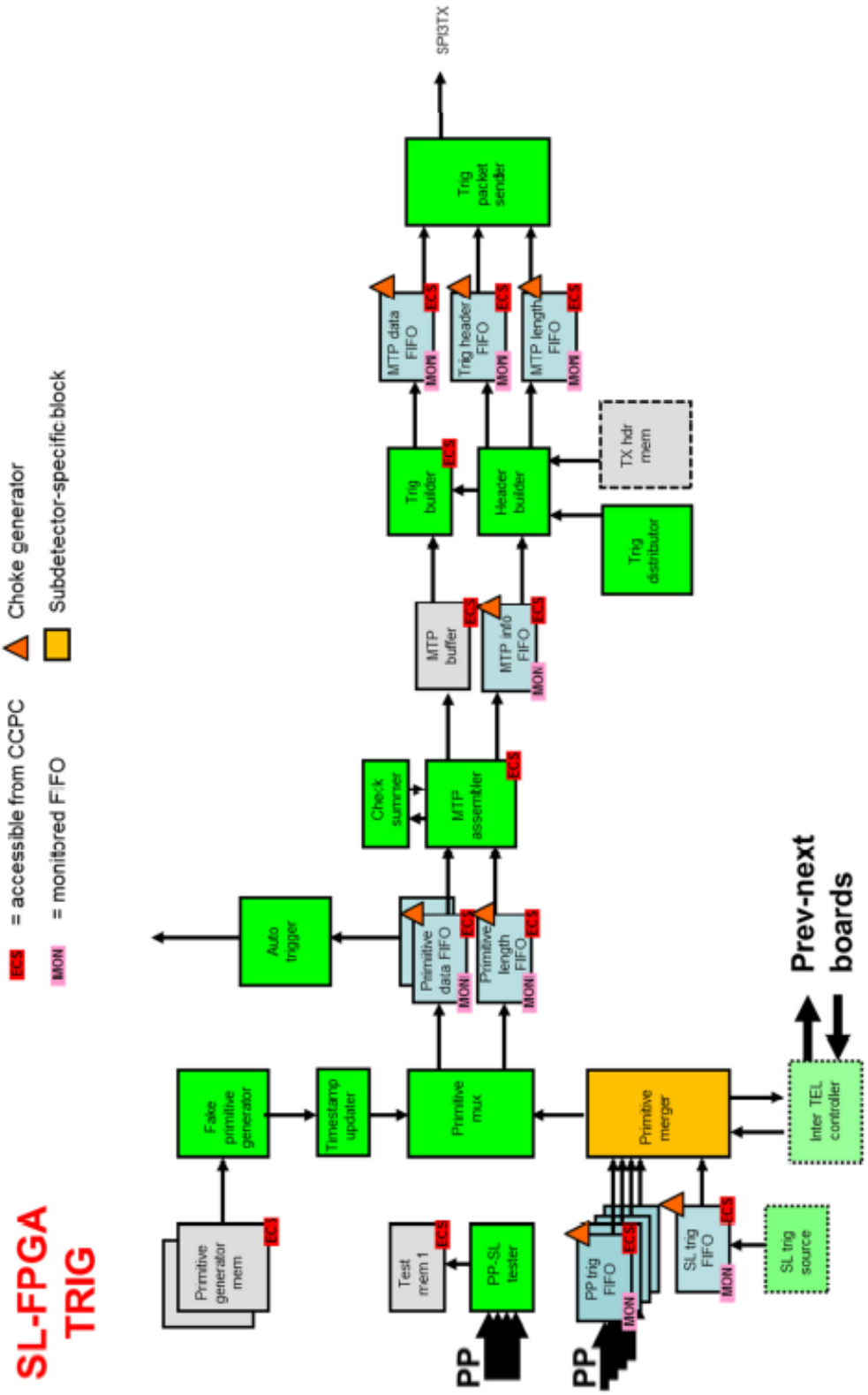

Figure 3.21: Trigger primitive generation flow block diagram of the SL-FPGA firmware.

Trigger and data flow The SL-FPGA receives the trigger, the start of burst (SOB) and the end of burst signals from the on-board TTCrx chip. The *TTC interface* block handles the communication with the on-board TTCrx chip. It decodes the signals and propagates the result to the remaining parts of the board. In this way at the time of SOB all the blocks are reset and the data acquisition starts, while the EOB signal stops the data acquisition. An internal timer, reset with the SOB signal, produces a timestamp that is assigned to each trigger and is used for debug and monitoring reasons. The trigger requests, from the *TTC interface*, are dispatched towards the PP-FPGAs where the corresponding data are read out. The data belonging to a trigger coming from the four PPs are merged in the SL-FPGA *data merger* block, that works in the same way of the OB block in the PP. The resulting event is stored in the *Event Data FIFO*. Multiple events can be packed in a single Multi-Event Packet (MEP) to optimize the output link bandwidth, limiting the fraction used by the packet header (42 B) rather than the payload. After MEP assembly the packets are temporarily stored in the external 1 Mbit QDR memory, written in a circular way: at each time it contains several readable for debugging purposes. The MEP packet is then extracted from the QDR, formatted in a UDP packet and passed to the *SPI3 interface*. This module takes care of the communication with the GbE output mezzanine that finally sends the packet to the PC farm.

Trigger primitive generation The trigger primitives follow a similar path to that of the data. The primitives coming from the PPs are merged by the *primitive merger* block and then they undergo further processing stages like multiplicity counting in the RICH or the cluster identification in the LAV. A communication interface between different TEL62 boards under development: it could be useful for the generation of trigger primitives for detectors that use more than one TEL62 (like LAV, RICH and KTAG).

The triggers, like the data, are packed in Multi-Trigger Packets (MTPs) which are formatted as UDP packets and sent via dedicated Ethernet ports of the GbE to the L0 Trigger Processor.

Monitoring and testing tools. The SL-FPGA, like the PP, has a lot of modules dedicated to testing the board interconnections and to monitoring the data acquisition status. It is possible to generate trigger patterns via CC-PC control to test the trigger and the data readout system. A tool in the SL allows to produce fake trigger primitives, overriding the primitive generation in the PP-FPGA, for the development and testing of the L0 Trigger Processor.

3.6.2 TEL62 tests

The performances of the TEL62 were tested at the end of 2013 during one of the TDAQ commissioning phases. We tested the output data bandwidth of the board (see figure 3.22) with a standalone data acquisition system, using the TDC emulators (inside the TDCC-FPGA) for data production and the LTU standalone

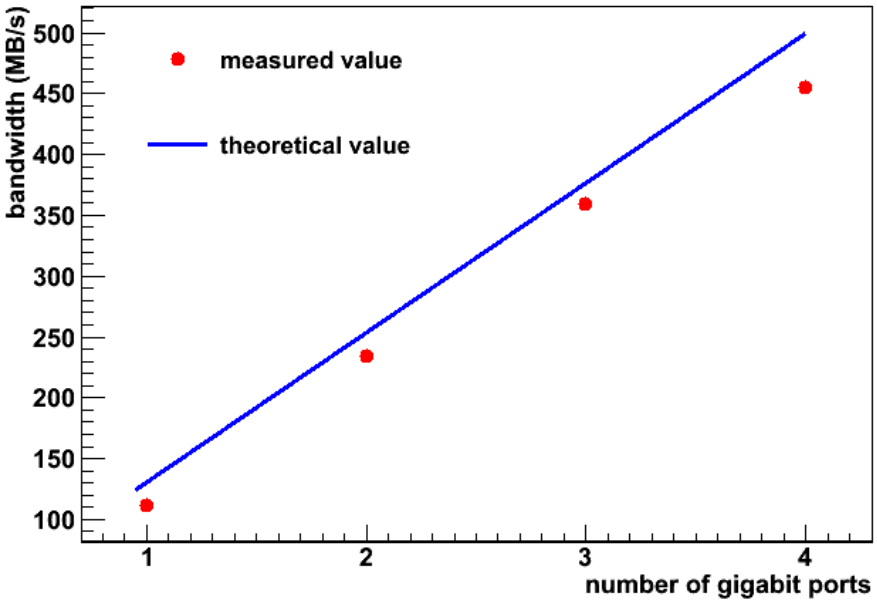

Figure 3.22: TEL62 output bandwidth as function of the number of used Gigabit ports. The blue line indicates the expected upper limit value (1 Gbit/s = 125 MB/s per port), while red points refers to the measured values.

mode[1] as trigger source. Results were in good agreement with expectations: the small gap between the expected upper rate limit value and the measured values indicates that the firmware could be further optimized even if there is some irreducible limitation introduced by the data formatting and other operations that prevents to reach the theoretical link bandwidth.

Figure 3.23 shows the maximum data payload (that is without including IP and UDP packet headers) for a given trigger rate using 4 Ethernet ports and assuming one data packet for each incoming trigger. The measured values lie on a hyperbola: the product between the trigger rate and the payload size is the effective data output bandwidth.

The TDCB+TEL62 system was extensively tested since the 2012 NA62 Technical Run to the 2015 NA62 Run. In the last Run the system still showed some rate inefficiency in the part that selects the Ethernet ports and sends the data packet to the GbE output mezzanine; witch is being addressed.

The measured time resolution is compatible with the intrinsic detector resolutions, with a negligible contribution from the TDCB. The TEL62 reached the design performance in the DDR2 memory data storage (160 Mword per second) and in the data extraction with a trigger rate up to 1 MHz

[1]In the standalone mode, the LTU can emulates the L0TP protocol and generates programmable trigger sequences.

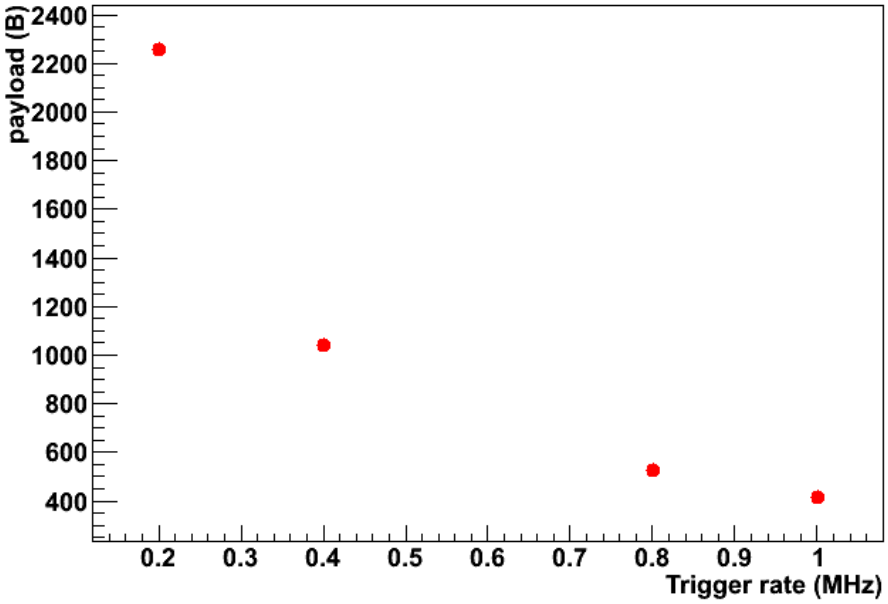

Figure 3.23: TEL62 data packet maximum payload size as function of the trigger rate using 4 output links.

Chapter 4

Studies of the NA62 L0 and L1 trigger

As we have already mentioned, the high beam intensity of the NA62 experiment requires a trigger system able to reject a large part of the background events, while losing the minimum amount of signal events ($K^+ \to \pi^+\nu\overline{\nu}$). To do that, NA62 adopts a multi-level trigger scheme composed of three levels: the first is hardware (L0) and is implemented in the firmware of the TEL62 common readout board and in the firmware of the L0TP; the other two (L1 and L2) are software high level triggers that run on a PC farm. At the nominal intensity, we expect an events rate on the main trigger detectors of about 13 MHz while for the PC farm the maximum average acceptable L0 trigger rate must not exceed 1 MHz, due to the available bandwidth, the size of the PC buffers and the average event size [15]. This rate should include the trigger for the main physics channel ($K^+ \to \pi^+\nu\overline{\nu}$) but also secondary triggers useful for other physical studies and control samples. The NA62 experiment could be useful to search and to measure the branching ratio of other rare or forbidden K^+ or π^+ decays [59]. For this reason the L0 trigger must reduce the background at least by a factor 10 or better 20.

4.1 Pre-run simulation

In the pre-run period (2014) the NA62 collaboration performed some Monte Carlo Analysis to find a L0 trigger scheme capable of selecting the main data stream for the $K^+ \to \pi^+\nu\overline{\nu}$ analysis. Proposals for different trigger schemes were considered: the guidance parameter to choose the L0 Trigger conditions was the achievement of a suppression factor of 50 on the event rate; this value allows to add to the data stream other physics channels, such as like lepton number violating decays, lepton flavour violating decays, etc.[59] ($K^+ \to \pi^- l_1^+ l_2^+$, $K^+ \to \pi^+ e^\pm \mu^\mp$ and $\pi^0 \to e^\pm \mu^\mp$, etc).

Monte Carlo simulations took in account the following contributions to the event rate[87]:

- the main 6 decay modes of the K^+ in the region between z = 100 m (just

after the GTK3) to z = 300 m [1]: $K^+ \to \pi^+\pi^0(\gamma)$, $K^+ \to \mu^+\nu(\gamma)$, $K^+ \to \pi^+\pi^+\pi^-$, $K^+ \to \pi^+\pi^0\pi^0$, $K^+ \to \pi^0 e^+\nu$, $K^+ \to \pi^0\mu^+\nu$;

- the muon halo due to $K^\pm$ and $\pi^\pm$ decays upstream the GTK3;
- beam π^+ that decay or interact with the material;
- beam protons that interact with the material.

The hadronic interactions of beam particles and the decay of K^+ in non muonic state both upstream the GTK3 was instead neglected.

An important part of that analysis was the simulation of the accidental activity, that is when there is an overlay of different events. In the analysis, simulated events of the physics processes described were mixed up and superimposed to the events of the studied process. To mix the events the assumption that the number of accidental events in a time window follow a Poissonian distribution was made. So that the probability to have at least one accidental event within a time t from the studied event is:

$$f(t) = 1 - e^{-Rt}$$

. where R is the total event rate.

Then the digitized hits of the different processes were added inside the sub-detector simulation to obtain overlayed events; the expected pulse width was taken into account in merging the signals.

The aim of the study was the evaluation of the total rate of the events passing the L0 trigger, that was simulated as a sequence of cuts, and of the trigger efficiency over the signal $K^+ \to \pi^+\nu\overline{\nu}$.

These Monte Carlo studies led to choose the following hardware conditions for each sub-detector involved in the L0 trigger decision:

- RICH: at least 3 PMs fired;
- CHOD: at least a crossing in one quadrant[2] (called Q1 condition);
- LKr: total energy between 1.5 GeV and 20 GeV, where total energy is the sum of the energy deposited in the cells with at least 50 MeV each;
- IRC, SAC: total energy deposited below 4 GeV;
- LAV1,12: total energy deposited per station below 4 GeV;
- MUV1,2: total hadronic energy greater than 8 GeV;
- MUV3: no pad fired.

The resulting rates for physics processes satisfying the above L0 trigger conditions are summarized in figure 4.1. Accidentals have a big effect in the result, indeed they increase the total rate by about 15% and decrease the efficiency of the signal by 16%.

[1] The coordinate z is parallel to the beam line, the axis origin is set at the target position.
[2] see section 2.3.3.

Process	Original	Rate, no accidentals	Rate, with accidentals
$K_{\mu 2}$	8397	2.4±0.5	11.3±1.5
$\pi^+\pi^0$	2729.9	40±2	39±1
$\pi^+\pi^+\pi^-$	738.6	39.2±0.9	34.4±0.8
$\pi^+\pi^0\pi^0$	232.7	1.0±0.1	1.2±0.1
K_{e3}	669.9	13.9±0.5	12.9±0.5
$K_{\mu 3}$	443.0	8.7±0.3	6.9±0.3
Beam π^+	526000	48±5	48±5
Beam protons	173000	3.9±0.7	3.0±0.7
Muons upstream	135000	1±1	22±5
Total L0		158±6	179±8
		ϵ, no accidentals	ϵ, with accidentals
Signal		(91.13±0.004)%	(74.85±0.006)%

Figure 4.1: Expected particle rate (kHz) and trigger efficiency (ϵ) after L0 (Errors are statistical only). The first value is the original rate (kHz) in input to the L0.

The final event rate is composed mainly of $K^+ \to \pi^+\pi^0$ and $K^+ \to \pi^+\pi^+\pi^-$ decays, beam π^+ and, considering accidentals, upstream-produced muons. The result of this Monte Carlo simulation is that the total rate of events passing L0 is below 200 KHz and the signal efficiency is about 75%.

4.2 Data sample

During the 2015 run it was not yet possible to use all the simulated trigger conditions and that reality was shown to be not completely described by the simulation, indeed we found a beam component inside the detector acceptance larger than expected, which changed the trigger efficiency.

The second part of my PhD work was to study the L0 trigger scheme for the selection of the $K^+ \to \pi^+\nu\overline{\nu}$ decay, on the real data obtained in 2015; this run lasted about 5 months, from June 15 to November 16. The study is based on the subdetectors which will generate L0 trigger primitives in the next data taking run starting in April 2016, and their trigger algorithms.

During the 2015 Na62 collected data with simple L0 triggers and often without a L1 and L2 trigger. We scanned the whole beam intensity range from about 0.6% to 100% of the nominal intensity. In this way we have almost a complete sample to study trigger efficiency and inefficiency for the 2016 run.

For this study I used 3 specific runs with different intensities (see table 4.1): 3809 (0.6% of the nominal intensity), 4069 (12% of the nominal intensity) and 4098 (60% of the nominal intensity). For each run I selected a single trigger channel to obtain a rate measurement before and after the complete trigger reconstruction.

I didn't use runs over the 60% of nominal intensity because some detector readout system were not yet able to sustain the corresponding rate of hits.

RUN NUMBER	T10 (ppp)	% Intensity	Number of Events	L0 Trigger Type ($N°$ events trigger)
3809	0.2×10^{11}	$\sim 0.6\%$	108904	Mask 0: $CHOD\&\overline{MUV3}\&L1KTAG$ (52605) Mask 1: $CHOD/2$ (97278)
4069	4.3×10^{11}	$\sim 12\%$	4069	Mask 0: $CHOD/200$ (123645) Mask 1: $CHOD\&\overline{MUV3}/200$ Mask 2: $CHOD\&LKr/10$
4098	21×10^{11}	$\sim 60\%$	243799	$LKr/14(MUV1 > 5GeV\&LKr < 5GeV)$

Table 4.1: Data Sample

4.3 L0 trigger studies

4.3.1 L0 primitive simulation

The starting point for the trigger analysis was to elaborate the raw data of the 2015 data-taking using the NA62Reconstruction software[83] that unpacks the raw data, applies the detector and time calibrations (hit reconstruction) and finally does the detectors' complete reconstruction returning event candidates. For this trigger analysis I did not use a complete detector reconstruction but only the reconstructed hits to start from informations similar to those we have in the online trigger.

The analysis evaluates the trigger primitives for each detector involved in the L0 trigger: CHOD, LKr, MUV1, RICH, MUV3, LAV12. The L0 trigger primitives transmitted to the L0TP contain the following informations [63]:

- The **Primitive ID** is the identifier of the primitive conditions being satisfied in the detector.
- The **Timestamp** is the time of the event that generated the L0 primitive, the LSB equals the period of the master clock, roughly 25 ns.
- The **Fine Time** allows to know the time of the primitive with a better granularity, the least significant bit is about 100 ps.

The CHOD is considered as the reference detector (see section 3.3.1): the time matching of the other detector primitives is verified in a time window of ± 6.4 ns around the CHOD primitive fine time.

We use CHOD, RICH, LKr and MUV1 as positive detectors to select the events, while MUV3 and LAV12 are in veto to reject events with muons or photon in the final state:

$$Trigger\ condition\ :\ CHOD\ and\ RICH\ and\ LKr/MUV1\ and\ \overline{MUV3}\ and\ \overline{LAV12}$$

Here follows a the description of the conditions for each detector to generate trigger primitives; LKr and MUV1 information are merged together to generate trigger primitives.

- **CHOD:** The CHOD primitives are based on the coincidences between horizontal and vertical planes; the time measurement is improved with the impact-point time correction. The scintillation light can take up to 10 ns

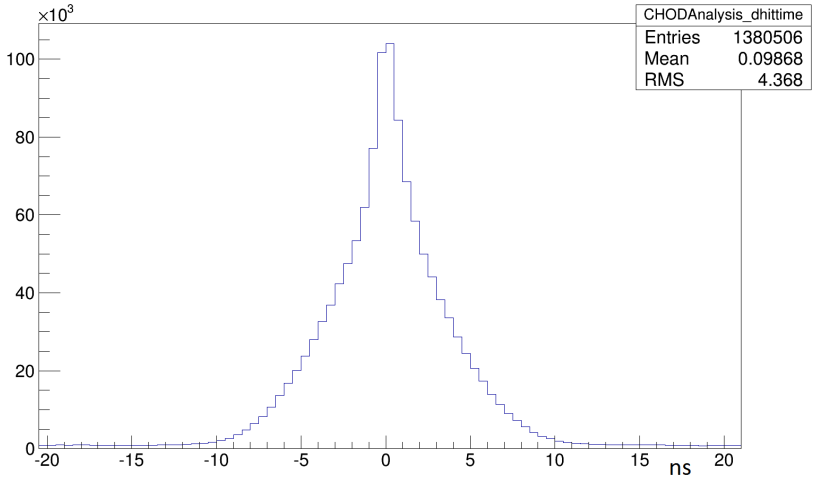

Figure 4.2: Time difference between the hits of the two CHOD planes after the application of the impact-point correction.

to cover all the slab length introducing a corresponding uncertainty in the time measurement. Once the position of the particle crossing is known one can correct and improve the time measurement subtracting to the time a constant depending on the difference between the crossing position and the PMT position.

The L0 trigger algorithm first splits the leading times of the CHOD hits between the two detector planes (x and y), then it looks for pair coincidences in space and time. Spatially the two channels should belong to the same CHOD quadrant and the required time condition was -3.2 ns $< \Delta t < 3.2$ ns (Δt is the time difference between the hits of the two plane, see figure 4.2). Coincidences within the same time interval are then grouped into the same primitive. One could also use informations about the hits or quadrant multiplicities, but the accidental activity and the particle interactions don't allow to have a safe [3] cut at L0. We prefer to use only a safe condition: at least 1 crossing point in in the CHOD to select events inside the CHOD acceptance.

- **RICH:** RICH primitives are based on the multiplicity of the leading times from super-cells evaluated in a single TEL62 board. The super-cells are the digital OR of 8 PMs made by a NINO chip[18]. All the leading times are clustered in a time interval (-3.2ns $< \Delta t < 3.2$ns, see figure 4.3) and a primitive is generated if the multiplicity of the cluster is at least 3. In this analysis, as in the RICH firmware of the 2016 RUN, we use a true time difference instead of filling a histogram with time measurements and cutting on its bins. Using histograms, the previous version of the firmware was subject to edge effects: two hits arbitrarily close in time could fall in different adjacent bins, in this way creating two different primitives for the

[3] at high beam rate the accidental activity and the particle interactions add several hits inside the selected time window

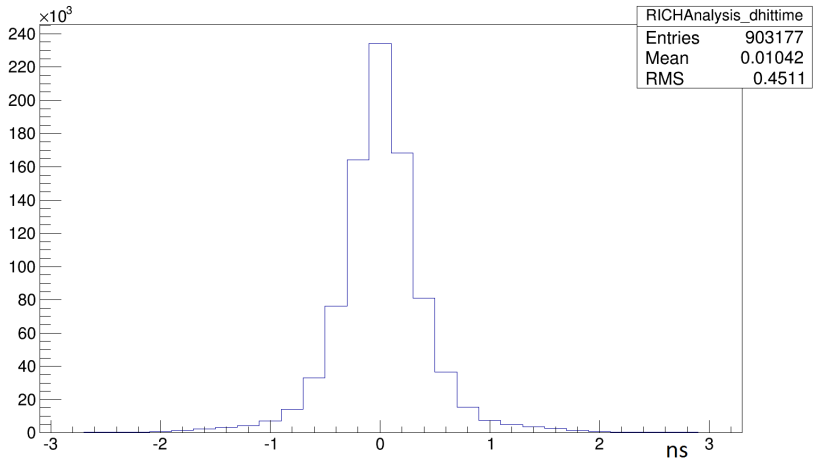

Figure 4.3: Time difference between the hits of the RICH.

same event or none if the hit multiplicity in the two bins did not pass the threshold.

- **LKr:** I wrote a software algorithm that simulates what is done at hardware level based on the collected data, even if the two implementations (primitive generator and read-out data system) are very different. The read-out of the LKr is based on a 25 ns sampling by FADC on each detector cell to find the energies peak and its time. The system also provides to the primitive generator a sampling of SuperCells (SC) energy. SuperCells are groups of 4 x 4 adjacent cells in a square, the sum is made digitally by the CREAM readout module[46]. 32 SC are analysed by 36 TEL62s linked like in a daisy chain: 28 "front-end" boards elaborate the informations of all the SuperCells and send the results to 7 "1st concentrator" TEL62s, these TEL62s put together the data received and send the result to one final "2nd concentrator" TEL62 [25]. This last TEL62 takes care of generating the trigger primitive and sending it to the L0TP. In the offline simulated algorithm we use the information of all the individual cells summing the energy of all the LKr channels and reconstructing the energy clusters. The LKr primitive is generated together with the MUV1 primitive (and in the future together with the IRC and SAC primitive);

- **MUV1:** the MUV1 uses the same readout and trigger system of the LKr, sampling from the scintillator strips and summing the energy information with the CREAM modules. The informations are evaluated by one TEL62 board that sends the results to the last board ("2nd concentrator") of the LKr daisy chain.

- **LKr/MUV1:** Two possible and rather different primitive conditions are under study for the two detectors LKr and MUV1 in the 2016 RUN. The first condition is looser on the rejection of events with photons in the final state as $K^+ \to \pi^+\pi^0$ but is safer then the second one for the signal efficiency:

to generate this trigger primitive at least one SuperCell in the LKr should have measured more than 1.2 GeV and the total energy in the LKr should be below 20 GeV ot, alternatively the MUV1 should have an energy larger than 5 GeV. This looser condition allow to select both the events with a pion producing an hadronic shower inside the LKr and that with the pion producing the hadronic shower inside the MUV1.

$$(E_{\text{LKr cluster}} > 1.2\ \text{GeV}\ \textit{and}\ E_{\text{total LKr}} < 20\ \text{GeV})\ \textit{or}\ E_{\text{MUV1}} > 5\ \text{GeV} \quad (4.1)$$

The second possibility allows to reject a bigger part of the background with the L0 but could lead to larger signal losses. It requires conditions on the LKr and the MUV1: at least one SC with more than 1.2 GeV energy and total energy below 8 GeV, and more than 5 GeV in the MUV1.

$$(E_{\text{LKr cluster}} > 1.2\ \text{GeV}\ \textit{and}\ E_{\text{total LKr}} < 8\ \text{GeV})\ \textit{and}\ E_{\text{MUV1}} > 5\ \text{GeV} \quad (4.2)$$

The energy threshold at 8 GeV together with the "and" condition between MUV1 and LKr allow to obtain a better rejection over events with photons in the final state but at the same time about the 40% of good signal event, with a pion producing an hadronic shower inside the LKr, could be lost.

- **LAV12:**For the moment only the last LAV station is used for trigger purposes. A primitive is generated if both the low threshold and the high threshold leading times are within 6.4 ns from each other (see figure 4.4). We require leading times for both the threshold to allow computing the slewing correction that is needed to reach an adequate time resolution of the primitives. The slewing correction is computed with a linear approximation of the rising edge of the pulse:

$$t_p = t_l - \frac{(t_h - t_l)V_l}{V_h - V_l}$$

where t_p is the time of the primitive corrected by the slewing correction, V_h and V_l are respectively the high and low thresholds, t_h and t_l are the leading times of the two threshold crossings.

- **MUV3:** The generation of the MUV3 L0 trigger primitive is based on the coincidence of the leading time hits from both PMTs belonging to the same scintillator pad. The time coincidence of the the hits should be within ±6 ns; figure 4.5 shows the time differences between the PMTs of the same pad. During the 2015 RUN a looser condition was used: a primitive was generated even if only one leading hit of the pad was present. This condition was used for debugging purposes and because the readout of some PMT was inefficient.

4.3.2 L0TP simulation

The L0TP has to match all the primitives coming from the detectors: it does not evaluate a trigger condition but it performs the time matching of the primitives.

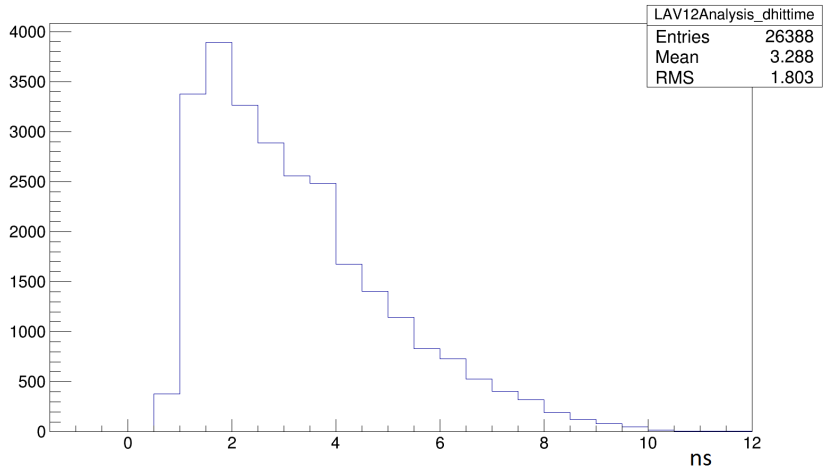

Figure 4.4: Time differences between the low threshold and the high threshold in the LAV12 leading times.

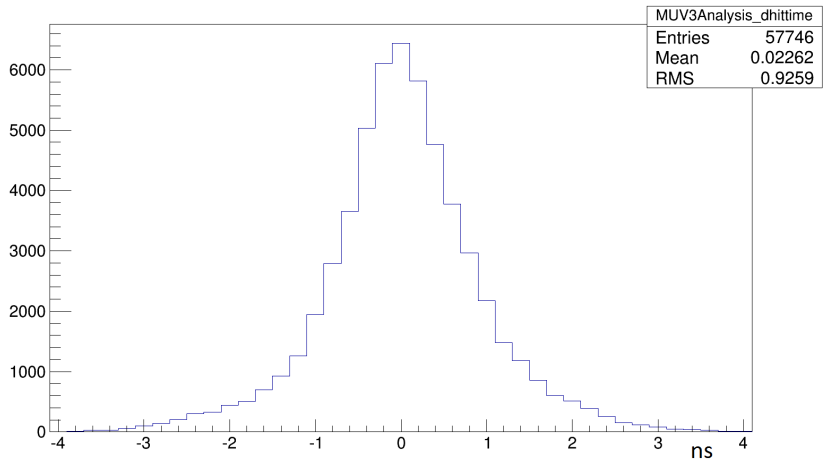

Figure 4.5: Time differences between hits of the same pad PMTs of the MUV3.

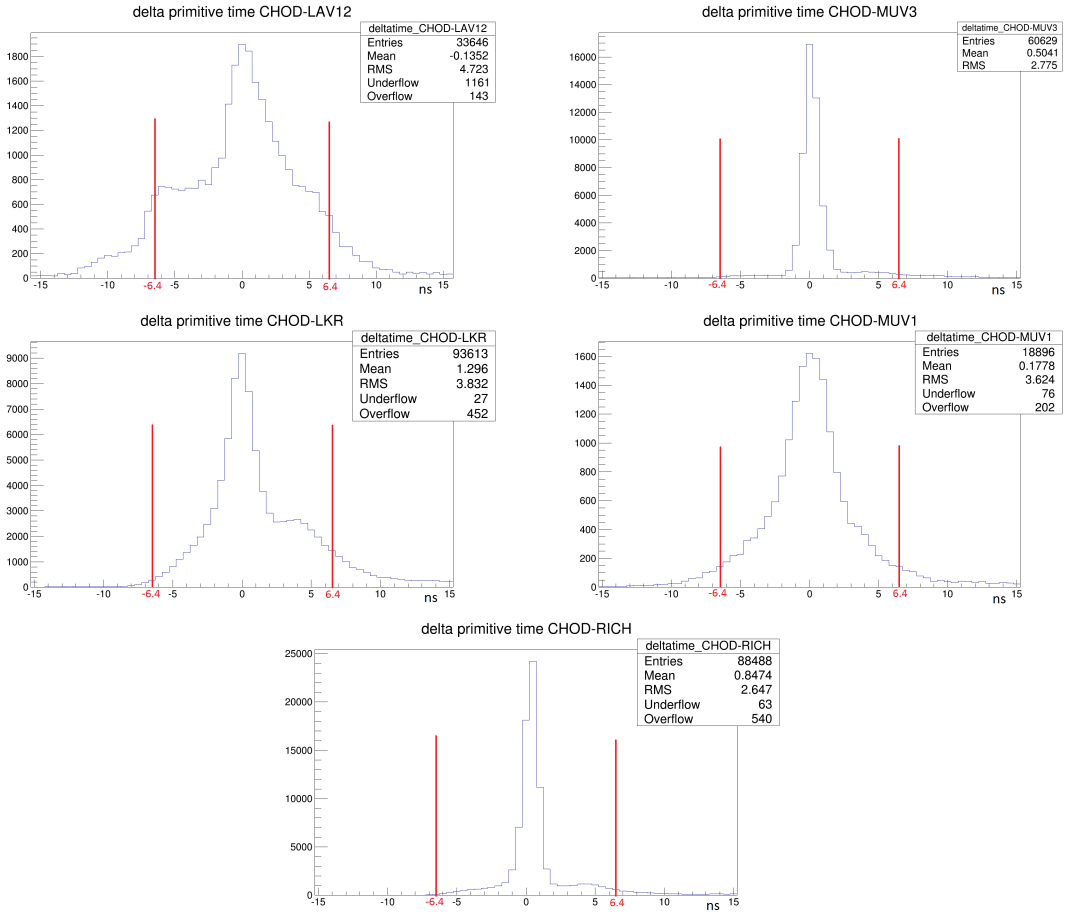

Figure 4.6: Time differences between CHOD and the other primitives.

The L0TP can implement several trigger masks to generate different trigger conditions for several purposes. The time matching always starts from the primitives of one detector called the *reference detector*: it is a positive element in the trigger chain and it gives its own timestamp to the trigger. At the moment the L0TP can use only one *reference detector* at a time, but for the 2016 RUN it should allow at least 2 *reference detectors*, In this way one could use completely uncorrelated triggers to compute the trigger efficiencies. The two *reference detectors* could be the CHOD and the RICH because they are positive elements in the chain and they have good time resolution. The primitive matching is done within a time window whose width is adjustable by firmware. The possible values of the time matching window size are ± 3.2, ± 6.4, ± 12.8 or ± 25.6 ns around the time of the primitive from the *reference detector*. Figure 4.6 shows the time differences between the CHOD primitive and other detectors' primitives. From these time differences one can see that the best compromise between the matching efficiency and the possibility to have random veto, due to the matching with noise or background events, is a time windows of ± 6.4 ns; indeed with a small time windows too many LAV12 and LKr/MUV1 primitives are lost.

A improvement for the next run could be the possibility to choose any size for the time matching window. To use small time windows while maintaining

a good efficiency, a precise time alignment of all the subdetectors is essential, indeed some software was developed to perform this alignment during the data taking.

4.3.3 L0 simulation results

The following two tables show the results of imposing, step by step, all the L0 trigger conditions on the data selected from 3 runs at different intensities (see table 4.1). To understand better the results I select the data collected with only one trigger channel for each run: CHOD trigger with downscale factor 2 for run 3809 at intensity 0.6% of nominal, CHOD trigger with downscale factor 200 for run 4069 at intensity 12% of nominal and LKr trigger with downscale factor 14 for run 4098 at intensity 60% of nominal. The CHOD condition during the data taking for run 4069 was equal to the one used in this analysis, i.e. at least 1 crossing in the detector; for run 3809 a loose condition was used instead: if the CHOD hit multiplicity is at least 3, the firmware generated a primitive. Other differences between this analysis and the actual implementation could be due to the different implementations (firmware instead of analysis software), edge effects in the time clustering which cause hits belonging to the same event fill adjacent bins instead of the same one and by time windows larger than in this reconstruction (this reconstruction aim to study the trigger implementation of the next run, not the previous one). The LKr condition used in run 4098 was similar to the tighter condition explained before (see equation 4.2). In the first table (figure 4.7a) the looser LKr/MUV1 condition (4.1) is applied, while in the second one (figure 4.7b) the tighter condition (4.2) is applied.

From the table we can see that the results for run 3809 and run 4069 are similar; the small differences could be attributed to some change betweem the two data samples due to the implementation of a new firmware in the TEL62 board that takes care of generating the CHOD primitive in the time between the two data taking periods. Indeed during run 3809 in the CHOD TEL62 board run a multiplicity primitive generator similar to the RICH one (more than 3 slabs firing in the CHOD), while during run 4069 the CHOD primitives creation were given by the crossings (at least 1 crossing).

A validation of this analysis is obtained comparing the actual generated primitives, that are recorded in the data files, with those simulated in the analysis. We use three detectors (RICH, LAV12 and MUV3) and run 3809 for this comparison: due to the low beam intensity, the sample is less subject to the accidental activity. In figures 4.8 the comparison between the generation of the primitives in this analysis and their generation inside the firmware is shown: the first bin contains the number of events that have primitives generated both by the firmware and this analysis, the second one the number of events which have only firmware generated primitives and the last bin the number of events with only the simulated primitives. The figures show a good agreement between the firmware and the analysis, particularly for the LAV12. In the RICH there is a significant number of events in which only the simulation finds at least one primitive (about the 14% of the events); this could be due to the edge effect in the time windows selection that should be removed in the firmware of the *2016 data taking*. The events in

Detector	Condition	Fraction of Events Remaining (Rejection factor detector) (Total rejection factor)		
		3809 only CHOD/2	4069 only CHOD/200	4098 LKr/14
CHOD	Al least 1 crossing	93% (1.08) (1.08)	87% (1.15) (1.15)	94% (1.06) (1.06)
LKr	$E_{cluster}$ > 1.2 GeV & E_{total} < 20 GeV	24% (3.88) (4.17)	28% (3.11) (3.57)	79% (1.19) (1.27)
MUV1	$E_{cluster}$ > 5 GeV			
RICH	N SuperCells > 3	16% (1.5) (6.25)	19% (1.47) (5.26)	63% (1.25) (1.59)
MUV3	At least 1 tight signal	13% (1.23) (7.69)	16% (1.19) (6.25)	48% (1.31) (2.08)
LAV12	At least 1 hit (both leading of low and high threshold)	10% (1.3) (10)	13% (1.23) (7.69)	41% (1.17) (2.44)

(a) *looser L0 contitions on LKr/MUV1.*

Detector	Condition	Fraction of Events Remaining (Rejection factor detector) (Total rejection factor)		
		3809 only CHOD/2	4069 only CHOD/200	4098 LKr/14
CHOD	Al least 1 crossing	93% (1.08) (1.08)	87% (1.15) (1.15)	94% (1.06) (1.06)
LKr	E_{total} <8 GeV	3.6% (25.8) (27.8)	3.9% (22.3) (25.6)	80% (1.17) (1.25)
MUV1	$E_{cluster}$ > 5 GeV			
RICH	N SuperCells > 3	2.6% (1.38) (38.5)	2.9% (1.34) (34.5)	67% (1.19) (1.49)
MUV3	At least 1 tight signal	2.2% (1.18) (45.5)	2.5% (1.16) (40)	47% (1.43) (2.13)
LAV12	At least 1 hit (both leading of low and high threshold)	1.9% (1.16) (52.6)	2.1% (1.19) (47.6)	41% (1.15) (2.44)

(b) *tighter L0 contitions on LKr/MUV1.*

Figure 4.7: Results of the simulation oftwo L0 trigger conditions.

MUV3 with only firmware primitives generation is explained by considering that the analysis implemented a tighter primitive condition (the coincidence of the hits from both the two PMTs of a single tile) instead of the condition used during the data taking; in which even a single PMT hit generated a trigger primitive. I have simulated this tighter condition because it will be implemented in the next data taking in order to reduce the random veto caused by the noise and the loose condition together.

Tables in figure 4.7 show that the LKr/MUV1 tighter condition (equation 4.2) allows to reach about a factor 5 higher L0 rejection. In run 4098 we don't see this improvement respect to the loose condition (equation 4.1) because in the actual firmware trigger condition for that run was already required this tight condition. This condition allows to have a lower input bandwidth to the PC farm but a preliminary study shows that it rejects a significant fraction ($\sim 70\%$) of events with a single π^+ in the final state resolving in an important inefficiency ($\sim 70\%$) in the $K^+ \to \pi^+\nu\bar{\nu}$ selection. For this reason in the rest of this work we'll consider only the safer condition (see 4.1) that allows to reach almost a factor 10 rejection, which is the goal of the L0 Trigger.

4.4 L1 trigger analysis

L1 is a software trigger implemented in the PC farm, so it is easier to obtain a reliable analysis of all the conditions applied on the detector data. For this analysis the L1 trigger conditions for 4 detectors are studied: KTAG, CHOD, LAV and STRAW. These are the most important detectors to reduce the trigger rate

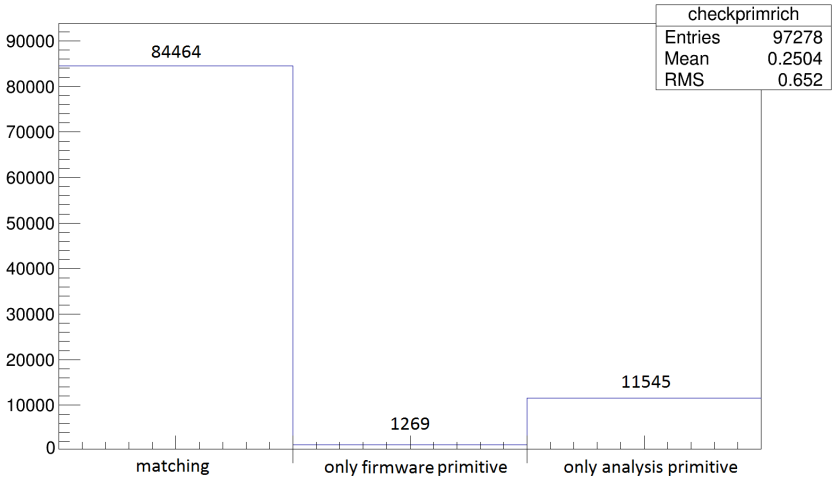

(a) *RICH*.

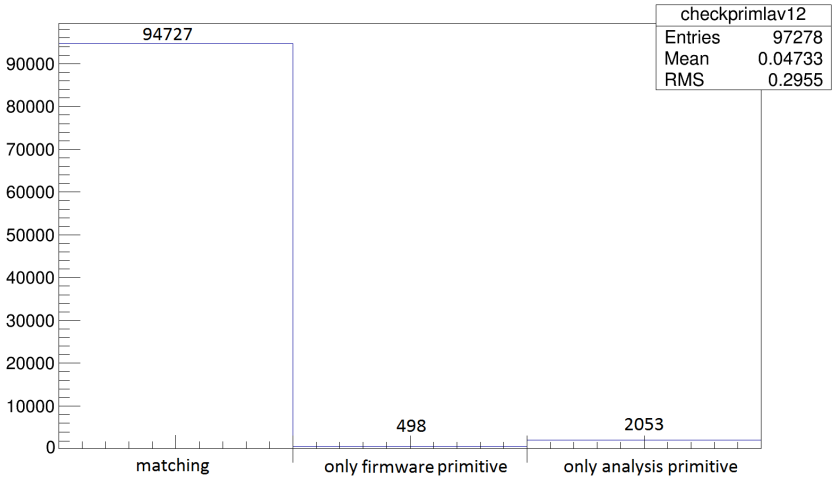

(b) *LAV12*.

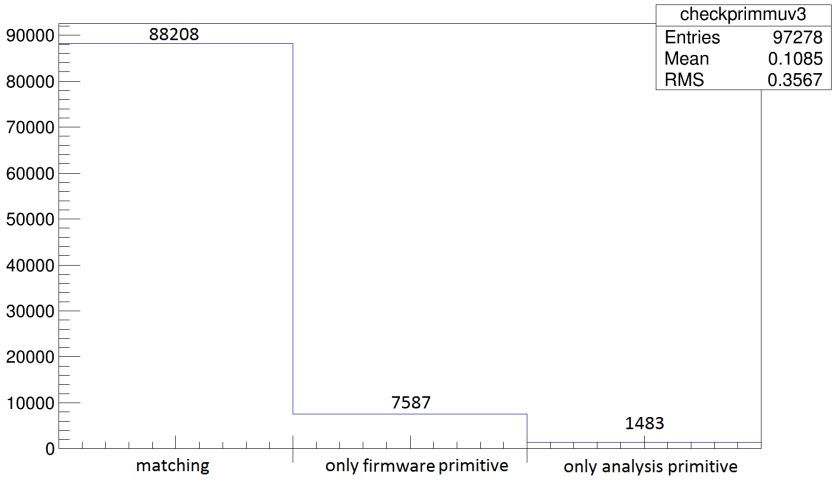

(c) *MUV3*.

Figure 4.8: Result of the comparison between the generation of primitives in this analysis and their generation inside the firmware.

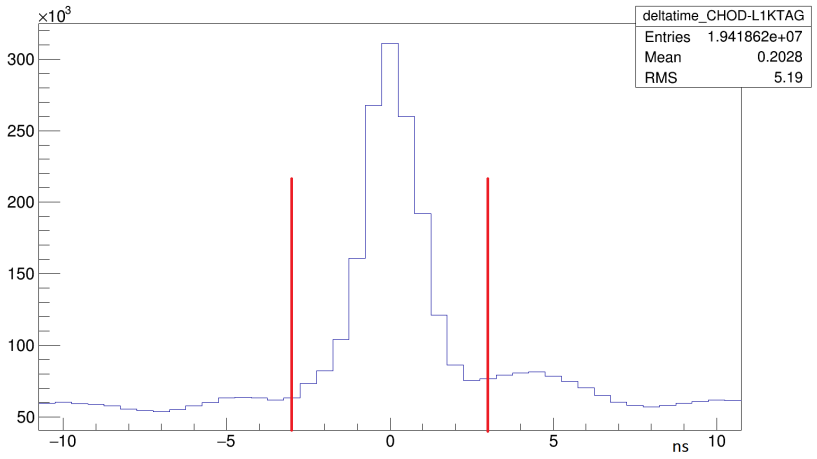

Figure 4.9: Time differences between KTAG hits time and the L0 trigger time.

although, after further studies, it appeared that other detectors could be added in the trigger during the 2016 run. The trigger algorithms for these detectors are already implemented in the PC farm, ready for use since the start of the 2016 RUN.

In the first weeks of the run the L1 algorithms will be used in flagging mode: if an event does not satisfy the trigger conditions the L1 will not reject it but the algorithm will just flag the event before passing it to the L2. In this way we can study the trigger efficiency and compare it with the present analysis. After validation, the L1 trigger will be put in cutting mode, so we can increase the beam intensity without the need of a random event downscaling.

The following study is done by applying one after the other the different L1 conditions to the data sample already used in the previous section and after the application of the L0 loose condition (equation 4.1).

4.4.1 KTAG

The KTAG is useful in the trigger selection because it allows to reject all the events not due to kaon decays: it removes a large fraction of the beam component (protons and pions are 93% of the beam). The KTAG indeed allows to select only K^+ particles, passing through it, cutting all the events who not exceed a threshold on the number of firing sectors (see section 2.2.1). In this analysis we select a time window of ± 3 ns (see figure 4.9) to do the matching of the kaons selected by the KTAG with the timestamp of the L0 trigger. The efficiency of this cut is very sensitive to accidental activity and therefore to the size of the time matching window: if many particles turn up inside the time window we'll have a greater number of firing sectors due to the contribution of all particles; in this way a large time matching window reduces the rejection factor of the KTAG condition. Figure 4.10 shows the distribution of the number of firing KTAG sectors: on the right of the red line indicating the cut condition is the K^+ contribution, and on the left is the background due to pions and protons. To keep only the kaon

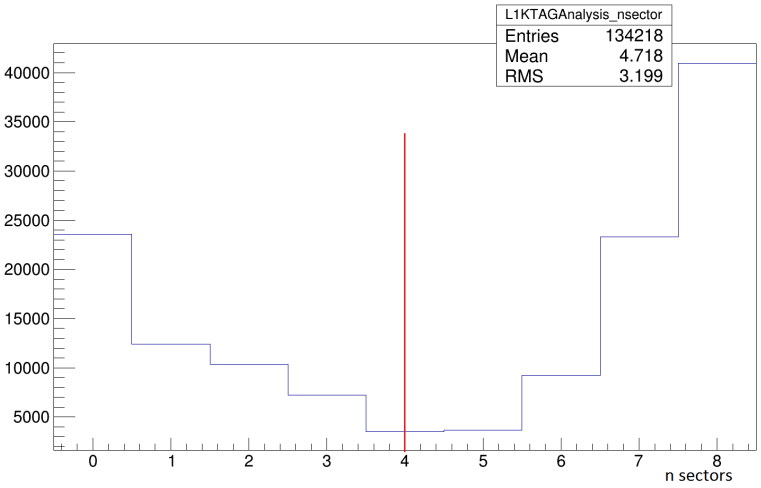

Figure 4.10: number of KTAG firing sectors for each event of run 4098 at intensity 60% of nominal, the red line shows the cut condition.

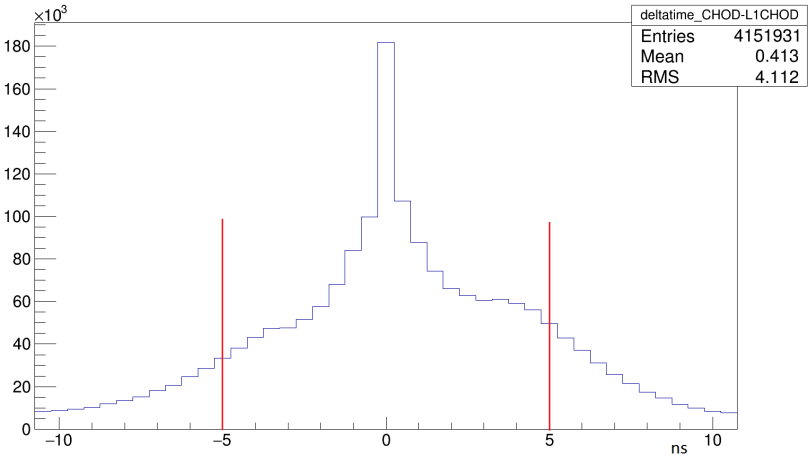

Figure 4.11: Time differences between CHOD hits time and the L0 trigger time.

contribution we decided to select only events with more than 4 sectors firing. This condition results in a rejection factor of about 1.6 for all three runs.

4.4.2 CHOD

The goal to use the CHOD in the L1 trigger is the rejection of multi-particle events; in this way we can prevent the STRAW algorithm from elaborating very large events, thus reducing the variability in its execution time (a significant fraction of the execution time of tracks reconstruction algorithm is due to the number of hit combinations that it has to analyse). The CHOD L1 algorithm looks for hits inside a ± 5 ns time window (see figure 4.11) around the L0 trigger time. In the 2015 run a condition on the number of CHOD slabs firing was used (< 5 slabs) but this cut is applicable only at low intensity (see figure 4.12a): indeed at 60% of the nominal intensity we have on average 26 slabs firing inside

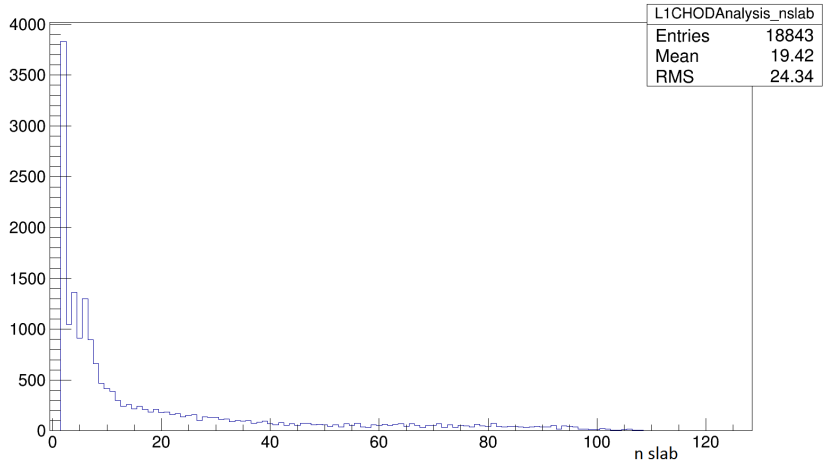

(a) 0.6% *of the nominal intensity.*

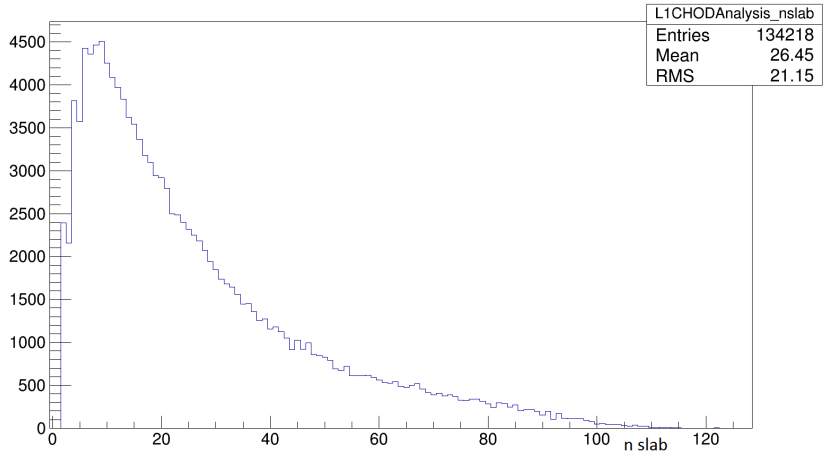

(b) 60% *of the nominal intensity.*

Figure 4.12: Number of firing slabs inside the CHOD time window (±5 ns).

the time window (see figure 4.12b).

We decided for a safe condition on the number of crossings (less than 5 crossings, see figure 4.13) to reject only very large events without losing a significant number of the signal events. Signal events could have more than one crossings for many reasons: accidental activity, emission of a delta ray, back-splash of particles that interact with the LKr calorimeter or particles produced in nuclear interactions with the RICH mirror. The CHOD L1 condition gives a rejection factor ranging from 1.3 for run 4098 to 1.58 for run 3809. The drop in rejection factor for run 4098 is probably due to a loss of efficiency correlated to the presence of accidental hits that can move a crossing out of the time window.

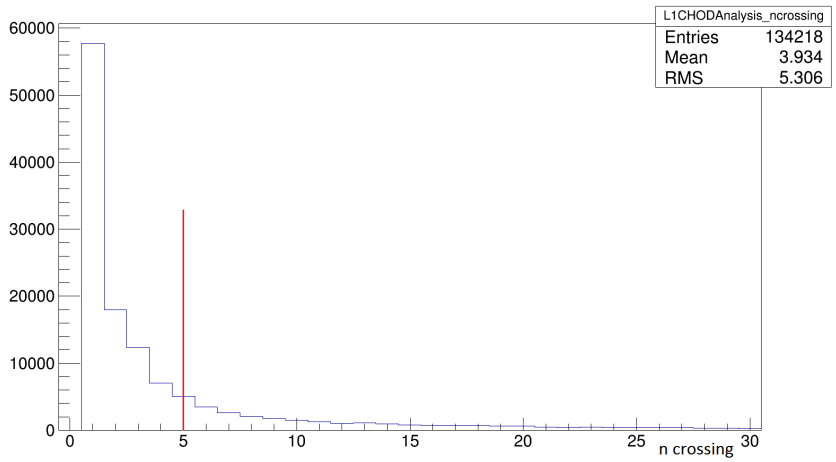

Figure 4.13: Number of CHOD crossings inside the time window (±5 ns); 60% of the nominal intensity.

4.4.3 LAV

All the LAV stations are used for the L1 trigger to reject the events with more than 1 *complete hit* (see figure 4.14) in any station in a time window of ±3 ns (see figure 4.15) around the L0 trigger time. We define a *complete hit* as hit that has all informations: both leading and trailing time measurement of both low and high threshold crossing. This cut is useful to reject events with photons in the final state and we require at least two hits to reduce random veto due to accidentals or noise events. The rejection factor for the LAV condition, after applying the KTAG and CHOD conditions, is about 1.3.

4.4.4 STRAW

A complete track reconstruction using the STRAW spectrometer is very useful in the rejection of the background because it allows to obtain new informations about the events, which can not be obtained with other detectors. Moreover, the STRAW spectrometer information is not used at all in L0 trigger, due to the slow time response of the detector and the complexity of the possible trigger condition. By using the track momentum, for example cutting above 70 GeV/c, is possible to remove the beam component that remains after the application of the KTAG condition, that is the kaon component and some proton or pion not vetoed by KTAG condition (due to accidental activity). Particles decay vertex reconstruction then allows to select only events decaying in or close to the fiducial region, rejecting, e.g., all the kaon decays occurring 180 m downstream the target. The value was choose far away from the fiducial region be sure not rejecting goos events. Moreover we can look for multi-track events to select them, for other physics purposes, or to reject them. The STRAW reconstruction is more complex than other L1 conditions and its development took a relevant fraction of my PhD thesis work so it will be described in detail in the next chapter.

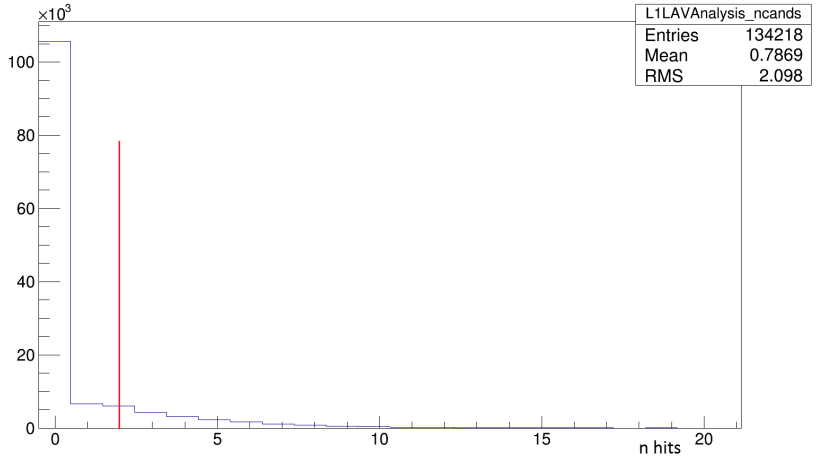

Figure 4.14: Number of LAV hits inside the time window; 60% of the nominal intensity..

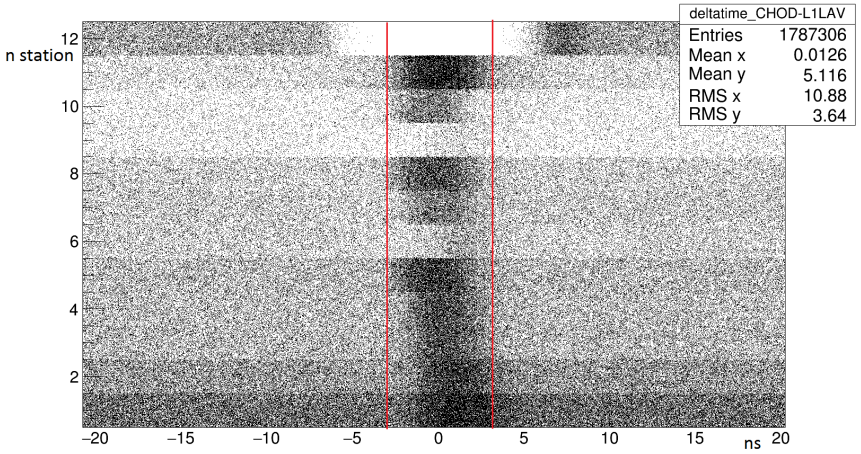

Figure 4.15: Time differences between LAV hits time and the L0 trigger time for each of the 12 LAV stations. The misalignment does not reduce the trigger efficiency because all stations have the physics peak inside the time windows. LAV12 does not have hits within the time window becuse is already used as veto in the L0 trigger.

Detector	Condition	Fraction of events remaining (Rejection factor detector) (total rejection factor)		
		3809 only CHOD/2	4069 only CHOD/200	4098 LKr/14
L0		10% (1.3) (10)	13% (1.23) (7.69)	41% (1.17) (2.44)
KTAG	N sector > 4 (inside ± 3 ns)	6.3% (1.59) (15.9)	8.1% (1.6) (12.3)	26% (1.58) (3.84)
CHOD	N Crossing < 5 (inside ± 5 ns)	4% (1.58) (25)	5.5% (1.47) (18.2)	20% (1.3) (5)
LAV	N complete hit < 2 (inside ± 3 ns) (both leading and trailing of low and high threshold)	2.9% (1.38) (34.5)	4.3% (1.28) (23.3)	15% (1.33) (6.66)

Figure 4.16: Result of the L1 trigger condition before straw application.

4.4.5 L1 result

In the figure 4.16 a table shows a summary of the L1 results before the application of the L1 STRAW algorithm. The rejection factors are in agreement among the three runs, the differences being mostly due to the changes in the L0 trigger. The total L0-L1 rejection factor so far is a factor between 23 and 35 so we miss another factor 3-4 to reach our goal of a 100 kHz output rate after L1.

4.5 GPUs

In recent years the use of commercial graphics cards "Graphic Processing Units" (GPUs) for scientific computing has grown considerably. Although GPUs have been designed for three-dimensional graphics and are produced mainly for the video game market, their parallel structure for data processing and their computing power can be used in several applications in the scientific field (for example in medical physics, astrophysics, quantum mechanics, molecular chemistry, etc. [57]). For these reasons a branch of computing research called General-Purpose Computing on Graphics Processing Units (GPGPU) was developed: it has the goal of using GPUs for computations that require a lot of processing power. GPUs have a different structure compared to the CPU (Central Processing Unit which is the processor of standard computers) with more chip area devoted to the computing unit with respect to flow control or caching, making the device more appropriate to highly parallelizable tasks (see figure 4.17).

From a comparison between the GPU and CPU (see figure 4.18) we note that the computing performance of GPUs exceeds by a factor 6 that of CPUs at present.

GPUs could be used to fill the lack of commercial processing devices on which the lowest level trigger of a high-energy experiment can be implemented and to reduce the size of PC farm used for the high level triggers [51].

4.5.1 GPUs in high energy physics

In the past decades High-Energy Physics experiments exploited custom-built processors with the most recent technology for the trigger and data acquisition systems. Lately, the large distribution of mass-market electronic devices changed this trend, since commercial hardware manufacturers now lead the development of the most performing digital computing devices. Moreover, the development of

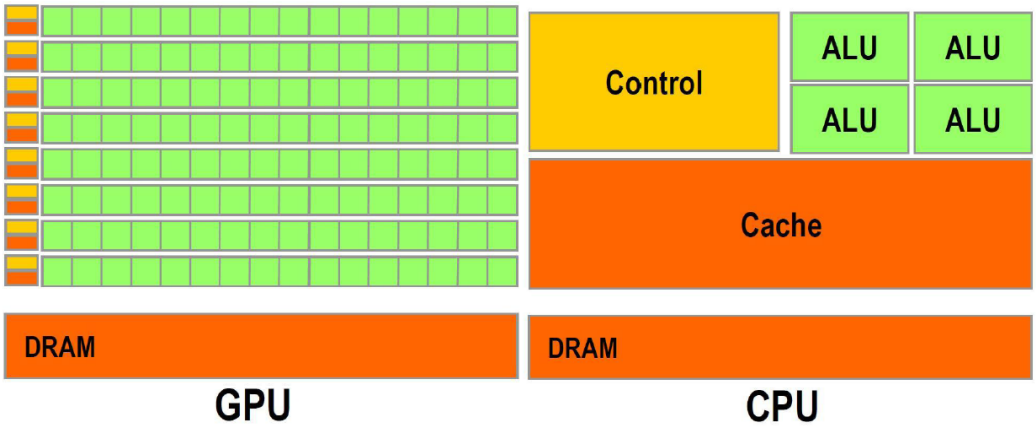

Figure 4.17: GPU and CPU architectures showing the ammount of chip area devoted to the different parts. The largest area (green) GPU chip is devoted to ALU (Arithmetic and Logic Unit) circuits that are fundamental block for computing operation; Flow control (yellow) and caching (red) units occupy a little fraction of the chip area.

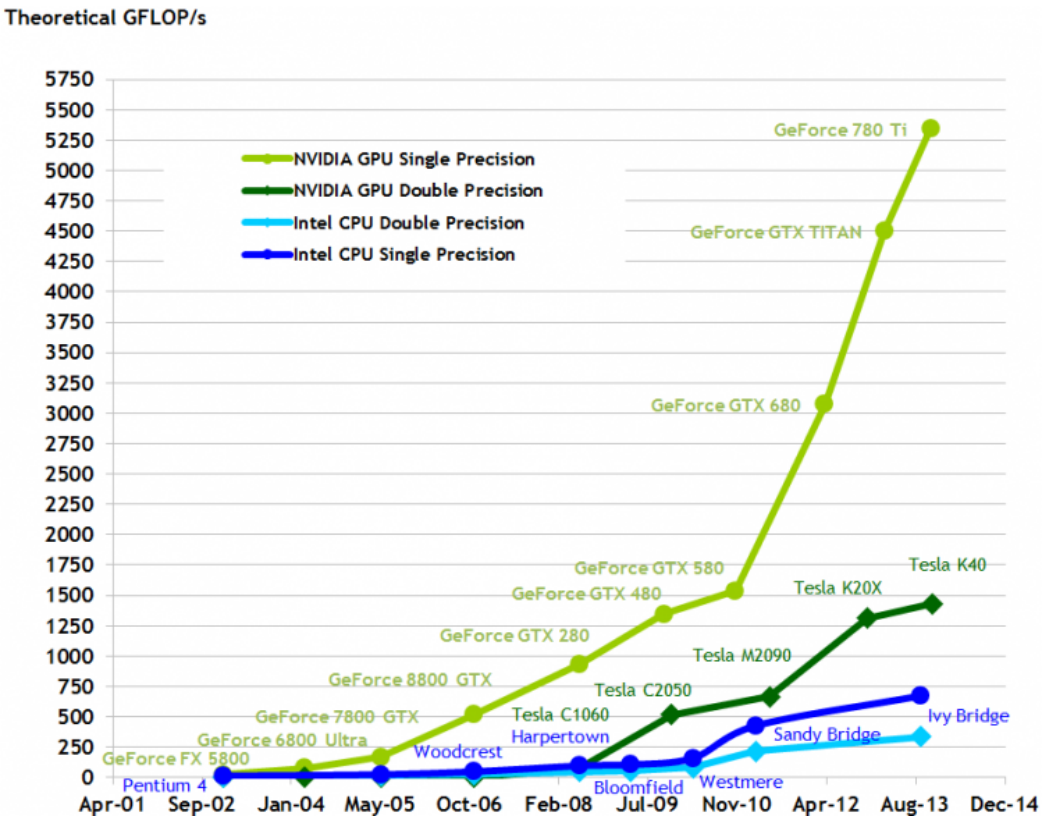

Figure 4.18: Time evolution of floating-Point Operations per Second for CPUs and GPUs in recent years.

these performing devices with the latest silicon technology involves costs usually not affordable for research groups.

These facts pushed the scientific community to evaluate commercial solutions instead of custom electronic systems for a growing part of TDAQ system. The obvious advantages of such trend lie in an optimization of the costs, installation and maintenance issues, as well as the possibility of easy upgrade, since more powerful devices become available every year at the same (or lower) price.

The only exception is given by very specific front-end electronics. Indeed until now it was not possible to implement the entire trigger and data acquisition system on a commercial processor for a *triggerless* approach, because the computer farm required would have an impractically large size.

GPUs can fill the missing gap between custom front-end electronics and commercial devices. They can be used to implement low level triggers or to reduce the size and the cost of computer farms used for running high level triggers.

The main problem with this approach is that GPUs are not designed for low latency response, since their target applications have only to deal with video frames at rates usually below a hundred Hz. The first level trigger of a HEP experiment must instead handle event rates even higher than 10 MHz in a maximum latency that is defined by the size of the buffer memories where data are stored. In recent HEP experiments this latency is of the order of $1 \div 10\ \mu$s even if there are some experiments, like NA62, with latencies that reach 1 ms.

Every year the computing power of GPUs increases so fast that their intrinsic time latencies approach the requirements of HEP lowest level triggers. Indeed in the last years the interest of the High-Energy Physics community for these devices grew considerably [33].

The LHC luminosity upgrade foreseen for the next years leads profit from GPU developments; the improvement of highly selective algorithms will be essential to obtain a sustainable trigger rate. To exploit these more complex algorithms a large computing performance is needed, which can't be any more obtained by increasing of CPU clock frequency. Indeed until few years ago the CPUs performance improved mostly with the increases of the clock frequency. Now the CPU clock frequency can't be increased due to physical constraints (the CPU power consumption increase with the CPU clock frequency) and increases in computing capabilities can be obtained only by using more cores and processors together. Several experiments are studying algorithms and developing the environment to use GPUs in their high-level trigger.

- The **ATLAS** experiment is studying a GPU implementation for the muon selection [27] and the track reconstruction for its Inner Detector [53][28]. The muon trigger algorithm is at the moment implemented as a simplified version in the ATLAS level 2 trigger system and it is based on the repeated execution of the same particle trajectory reconstruction. The high computing capability of GPUs will allow to use a more refined muon algorithm for better selection and efficiency. Concerning the track reconstruction algorithm the parallelization of the data preparation step on a GPU reached a speed-up of up to 26x over the serial CPU version and the implementation of a Reference Kalman-Filter on the GPU achieved a speed-up of 16x

compared to a single threaded CPU version[28].

- **CMB** (Compressed Baryonic Matter), a future heavy-ion experiment, is studying the implementation of its online First Level Event Selection on a dedicated many-core CPU/GPU cluster. IThis system should be able to elaborate a huge data quantity of up to 1 TB/s [7].

- The **LHCB** experiment in its upgrade phase is developing a trigger-less data acquisition system to read-out all the detector at the bunch-crossing rate of 40 MHz. The events that LHCB stores have a small size (order of 100 kB) so it is relatively easy to use GPUs or multi-core CPUs to process many events in parallel for a real time selection without lose time in the bottleneck due to the transfer speed to the GPUs. Moreover this possible solution might reduce the cost of the High Level Trigger (HLT) Farm. Since the vertex finding and the track reconstruction algorithms are the more time consuming threads running in the HLT, they will be probably the first to be implemented on GPUs. Preliminary results show a speed-up of a factor 3 with respect to CPUs obtained using the GPU for the tracking algorithm respect to the sequential one [56].

- The **CMS** experiment is studying the benefits of using GPUs to reconstruct high energy tracks in the core of high P_T jets coming from the heavy quarks. Indeed the tracks from B-decays, ad high transverse momentum, become more collimated, reducing the efficiency of the standard track-finding algorithms. The combinatorial complexity of such algorithms could profit from an implementation on GPUs [33].

- The **PANDA** hadronic physics experiment, under construction at FAIR (the Facility for Antiproton and Ion Research in Darmstadt) will not use hardware-based triggering but sophisticated software-based online event triggers. They are investigating three different GPU-based algorithms for the track reconstruction [66]: the Hough transform (a method that allows to detect edges in images), a Riemann Track Finder (which uses the projection of two dimensional hit points onto a Riemann surface) and a Triplet Finder (an algorithm specifically designed for the PANDA straw Tube Tracker that analyses only small subsets of data at time). Using the Triplet Finder algorithm, a cluster of O(100) GPUs seems sufficient for the PANDA trigger system to cope with the expected rates.

4.5.2 GPUs in NA62

The NA62 Collaboration has been considering GPUs for two different applications: finding rings inside the RICH in the L0 trigger [16] and implementing a complete track reconstruction in the L1 trigger reducing its execution time [86].

GPUs for a L0 RICH trigger

As already mentioned in this chapter, the L0 Trigger primitives for the RICH are based on the multiplicity of the leading time measurements from the detector

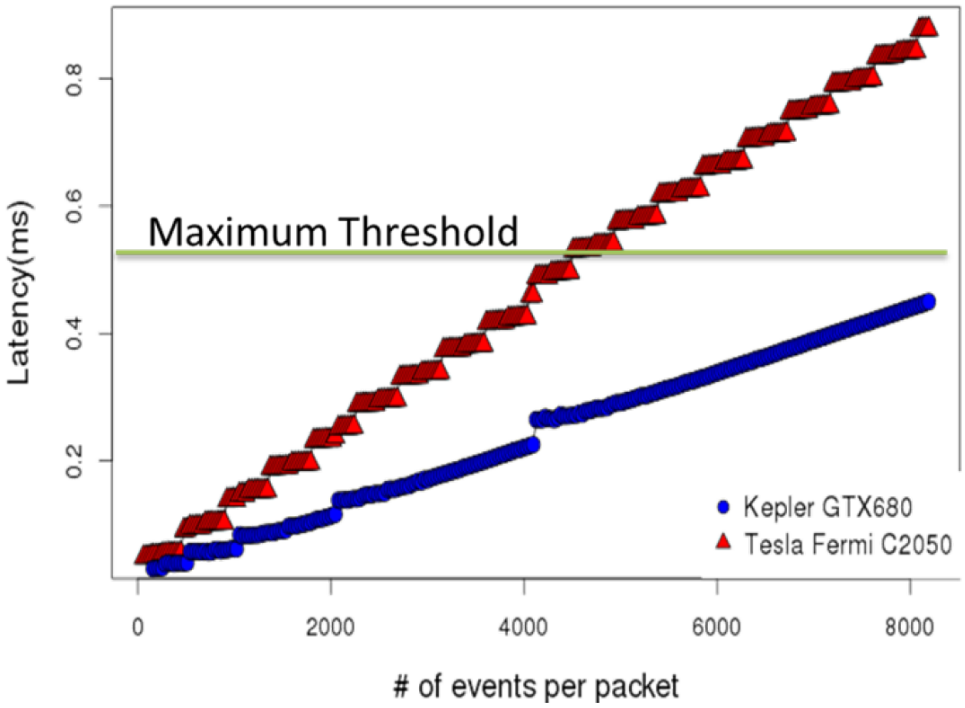

Figure 4.19: Total latency, including data transfer and computing, of the RICH L0 algorithm using two different GPUs.

super-cells. The use of GPUs at this trigger level can allow to evaluate a more complex condition for the trigger primitive, based on the velocity or the direction of the charged particles crossing the RICH detector. It is possible to use this information to compute other physical quantities, like the decay vertex of the K^+ and the missing mass, in the following of trigger levels.

The system proposed for the use of the GPUs inside the L0 Trigger will initially operate in a parasitic mode to study the performance during the normal data taking.

Several different ring reconstruction algorithms were studied to find the best compromise between execution time and trigger efficiency [51]. For most of the events from kaon decays a single ring reconstruction can be performed. In terms of computing throughput, algebraic non-iterative fits, like Crowford and Taubin fits [90][47], are suitable for hard-real time performances. In case of multiple rings a fast and trackless algorithm [73] (also known as "Almagest") has been developped. Starting from purely geometrical considerations based on the Ptolemy's theorem, this algorithm is able to reconstruct multi rings events with an offline quality in less than 1 μs.

Figure 4.19 shows the total computing latency, including data transfer time to and from the GPU and the kernel computing time; The green line marks the maximum latency allowed to the GPU in the experiment (The total NA62 latency is 1 ms but we must subtract the time required to the data transfer and to the L0TP operations), showing that the use of GPUs for this purpose is possible.

To reduce the data transfer time to the GPU a custom FPGA-based NIC (Network Interface Card) board will be used instead of a standard one. Indeed

usually the detector data reaches a commercial NIC board which copies it on a dedicated area in the PC RAM, and from that area data is copied to the user space memory where applications can process them. In user space data is formatted and copied to GPU memory through the PCI express bus. These multiple copy operation impact on the latency and should be avoided in the present application.

A custom FPGA-based NIC called NaNet[76] was developed to improve in this aspect: NaNet is able to exploit the GPUDirect peer-to-peer (P2P) capabilities of NVIDIA recent GPUs, enabling to directly inject UDP input data from the detector front-end into GPU, with speeds compatible with the low latency real-time requirements of the trigger system.

Preliminary results on the complete system with GPUs show that it is suitable for sustaining the event rates within the required latency.

GPUs for a L1 STRAW trigger

A complete track reconstruction at the L1 trigger level could be very time consuming, so that other trigger algorithms, in particular those for L2, will have only a limited time budget available for their operations. I worked on the implementation of a preliminary STRAW algorithm for NA62 on GPU for my master thesis, obtaining promising results: the algorithm execution time was about 63 μs [86]. The algorithm should be able to stand the expected rate if we consider the use of up to 32 GPUs in parallel (the total capability of the NA62 PC farm) and the fact that applying after the other L1 conditions the expected input rate to the algorithm should be below 300 kHz. Furthermore the GPU used for the measurement is, by now, obsolete and we could use new and more performing devices.

It is in our plans so to study the implementation of the new STRAW algorithm on GPU for the next NA62 runs.

Chapter 5

STRAW L1 trigger study

5.1 Introduction

This chapter describes another important part of my PhD work: the study of a L1 trigger algorithm for the STRAW spectrometer that is now implemented as a sequential version in the NA62 PC farm and could be implemented as a parallel version on GPUs. The GPUs will reduce the execution time needed to reconstruct events' tracks and will allow to implement other time consuming algorithms at the L2 trigger.

The L1 STRAW algorithm was developed using a Monte Carlo simulation and it was validated and fine-tuned with real data collected during the 2015 run.

5.2 Simulation

The NA62MC[83] software was used to simulate the experiment and to generate decays. The six main decay modes of the K^+ were simulated in a region extending from GTK3 to z = 300 m (where z = 0 m is the target position and z = 300 m is the end of the experiment zone): $K^+ \to \mu^+\nu(K_{\mu 2})$, $K^+ \to \pi^+\pi^0$, $K^+ \to \mu^+\pi^0\nu$ $(K_{\mu 3})$, $K^+ \to e^+\pi^0\nu$ (K_{e3}), $K^+ \to \pi^+\pi^+\pi^-$, $K^+ \to \pi^+\pi^0\pi^0$. In addition, two sources of beam halo events were added to the simulation: the beam pions and the muons generated *upstream* (from beam pion and kaon decays before of the GTK3). The *upstream* muons can be divided in 4 classes depending on their parent particle (K^+, K^-, π^+, π^-). The proton beam component was not considered in this simulation, because the protons do not decay and so they should not generate a big rate on the detector. The signal $K^+ \to \pi^+\nu\overline{\nu}$ was simulated in the fiducial decay region (from z = 105 m to z = 165 m) and with a π^+ momentum between 15 GeV/c and 35 GeV/c. The maximum straw drift time ($\sim$ 200 ns) makes it mandatory to include accidentals in the simulation, indeed, with a decay rate of about 13 MHz, within the spectrometer time window there is on average at least 1 track of a particle that belongs to an overlaid event. In the simulation I use a time window twice the drift time ($\sim$ 320 ns) because there would be both preceding and following hits with a leading time within the drift time window of the central event. I used a modified version of the NA62MC generator code to include accidentals in the main decays. Additional K decays (according to

their branching ratios) were added to the central event of the process under the assumption that the number of accidental events is described by a Poissonian distribution. The formula $P(t) = 1 - e^{-Rt}$ gives the probability of having at least one accidental event within a time interval t after or before the central event.

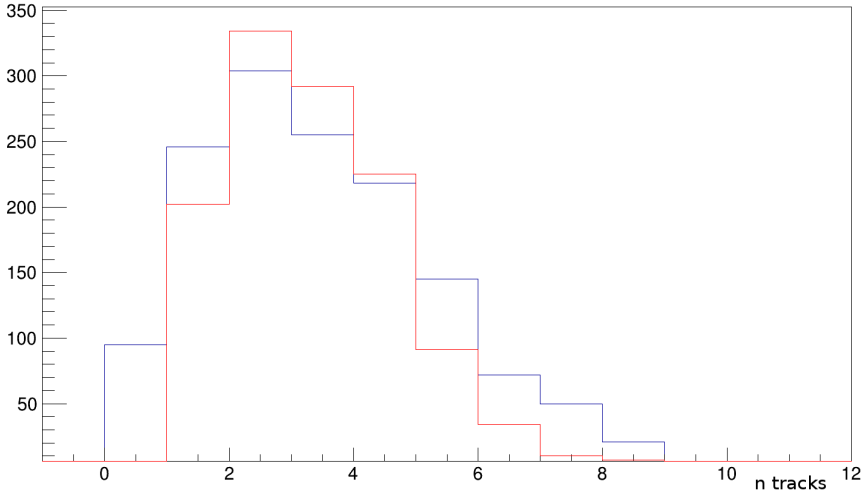

(a) number of tracks in the spectrometer in a 320 ns windows.

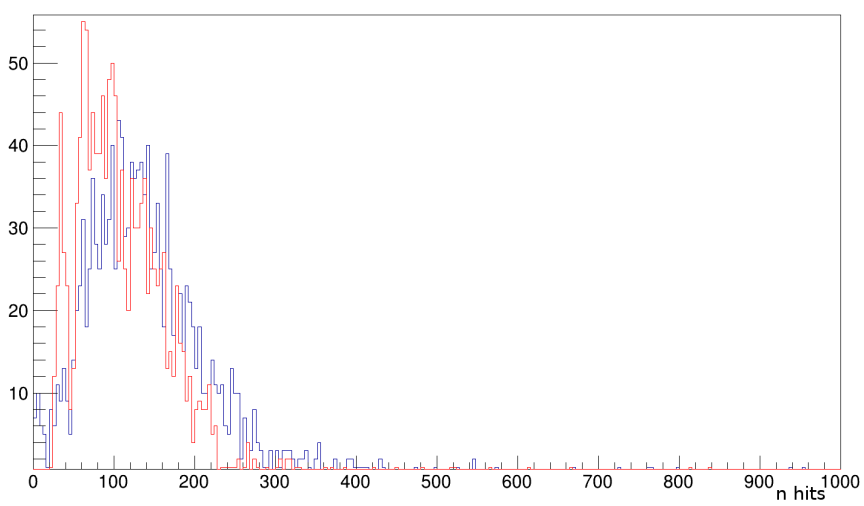

(b) number of hits in the spectrometer in a 320 ns windows.

Figure 5.1: Events of $\pi^+\nu\overline{\nu}$ (red) and $\pi^+\pi^+\pi^-$ (blue) with accidentals superimposed.

Accidentals don't allow the use of hits multiplicity to cut background events because inside a time window of 320 ns there are about 3 tracks on average in the spectrometer, both for $\pi^+\nu\overline{\nu}$ events and background events such as $\pi^+\pi^+\pi^-$ (see figure 5.1).

Each straw hit generates a leading and a trailing time: when compared to the time of the track passage in the chamber, the former depends on the distance of the hit from the wire, the latter is fixed by the straw radius. The simulation takes the straw hit times and the true crossing point of the particles, and, using a *parametric MC Straw Response* that transforms a distance from the straw wire to

a drift time, it generates the hit leading and trailing times. The *parametric MC Straw Response* already simulates the leading time resolution, while the trailing time was smeared with a Gaussian distribution with $\sigma = 40$ ns (fig:5.2) that was the estimated resolution.

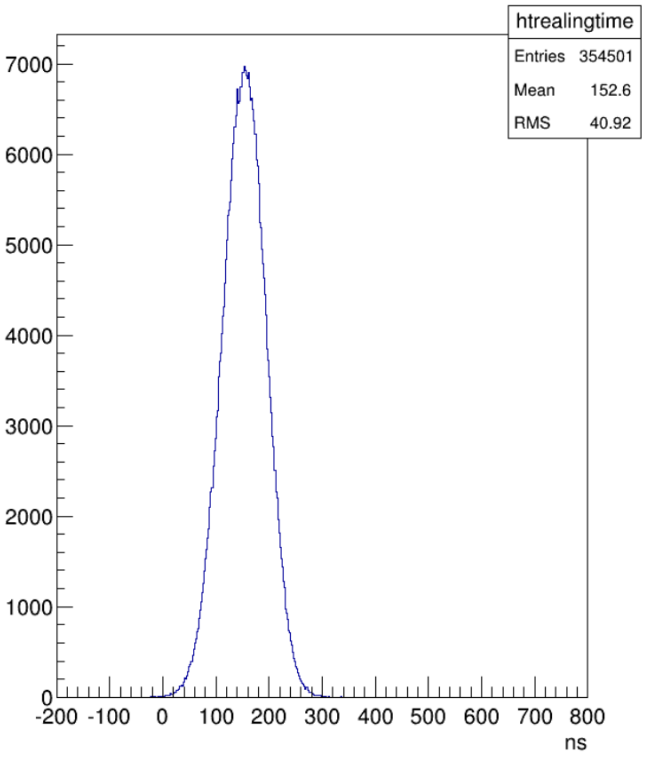

Figure 5.2: Trailing time distribution with 40 ns smearing for events of $\pi^+\nu\overline{\nu}$ (without accidentals).

Both the leading time, used to reconstruct the track distance from the wire, and the trailing time are useful to reject accidentals.

5.3 Algorithm flow

Due to the large number of hits, the only effective way to use the STRAW Tracker to cut the background is to completely reconstruct the tracks. Thus, we can remove the events that don't have reconstructed tracks with the longitudinal momentum within a specific range or that have the decay vertex outside the fiducial region. An essential point of the algorithm, before these cuts are applied, is to remove accidentals. Because of chamber geometry and multiplicity considerations[1], we have to cluster the hits generated by the single particles before starting with the pattern recognition. The main steps of the L1 Straw trigger algorithm are:

- hit clustering within one view;
- hit clustering within one chamber;

[1]For each chamber we could have up to 12 hits belonging to the same track and each hit gives only a partial information.

- pattern recognition of the tracks;
- tracks selection and trigger cuts;

5.3.1 Hit clustering within one view

A view-plane is composed by four adjacent straw-planes with parallel straw tubes that are staggered to solve the left-right ambiguity intrinsic to the hit minimum distance measurement (fig. 5.3).

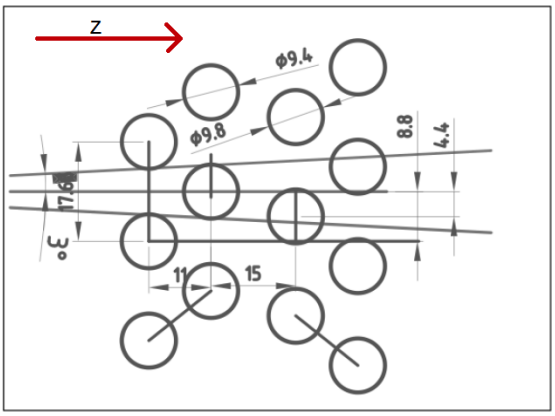

Figure 5.3: Straw layout in one view (beam direction from left to right)[15]. The distances are in mm. The four layer are visible, with 3 straws in each.

The number of straws hit by a particle in one view depends on the position of the impact point of the particle on the first plane, in the hypothesis of a straight path parallel to the z axis (that is along the beam line). There are only two cases: a particle can hit either two or three straws. I decided to use anyway only two hits for each cluster to speed up the algorithm, because I did not observe any efficiency improvement in the final result using three-hits clusters: 97.9% of efficiency for $\pi^+\nu\overline{\nu}$ events compared to 98.4% using only two-hits cluster, the difference being inside the statistical error of 3.1%. Two-hit clusters are composed by one hit in the first two straw-planes (the first half-view) and one hit in the second one (the second half-view). The cluster coordinate is obtained as the average of the two hit positions. The three-hits clusters are considered as two-hit clusters for the coordinate computation.

The 4 possible types of two-hit clusters are shown in Figure 5.4 where a letter is associated to each track and to its own cluster. The average coordinate which is associated to each type of cluster is:

$$cluster\ A : coordinate = [(y_n - r_0) + (y_n - d + r_3)]/2$$

$$cluster\ B : coordinate = [(y_n + r_0) + (y_n + d - r_2)]/2$$

$$cluster\ C : coordinate = [(y_m - e - r_1) + (y_{m-1} + d + r_2)]/2$$

$$cluster\ D : coordinate = [(y_m - e + r_1) + (y_m - d - r_3)]/2$$

Where $y_{n,m}$ is the coordinate of the centre of straw n or m in plane 0, r_a (a is the number of the straw-plane) is the transverse distance between hit and the straw

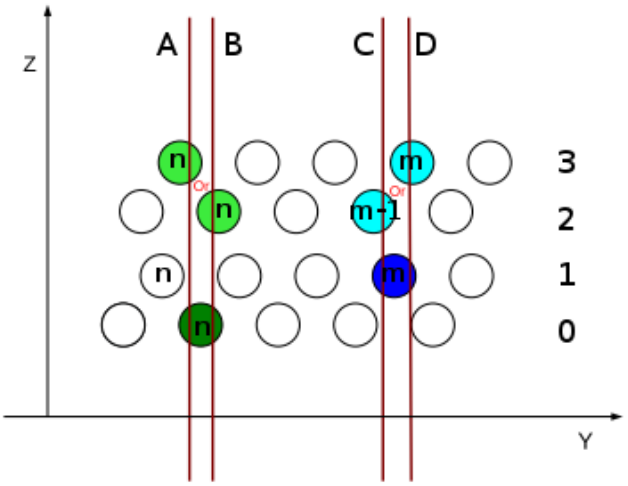

Figure 5.4: Types of two hit clusters: n and m are straw numbers, the letters near the tracks identify the type of the cluster and the numbers to the side identify the straw plane inside a view. Planes 0 and 1 belong to the first half-view whereas 2 and 3 belong to the second half-view.

centre obtained from the leading time, the trigger time and the function that parametrizes the straw response, $d = 4.4$ mm is the distance between two straw centres belonging to different half-views, $e = 8.8$ mm is the distance between two straw centres belonging to the same half-view. Fig 5.5 shows the cluster resolution obtained by the algorithm.

Only the hits that pass the following timing cut on the leading time and the trailing time take part in the clustering (fig. 5.6).

$$T1 < \textit{leading time} < T2 \qquad T3 < \textit{trailing time} < T4 \tag{5.1}$$

The value of the above cut parameters will be discussed in the next section.

The trailing time of the clusters are the averages of the corresponding trailing times of the hits that compose them (fig. 5.7).

Clustering allows to implement a cut derived from the view-plane geometry: the sum of the distances $r_{a,b}$ to the closest wires for two hits (a and b) belonging to the same track but in planes of different half-views should be equal to the distance between the straw wires (4.4 mm). For this cut I evaluated the smearing due to the track slopes and to the leading time uncertainty (fig. 5.8).

$$CUT_{low} < r_a + r_b - 4.4 \text{ mm} < CUT_{high} \tag{5.2}$$

I use different cut values on the 2 sides because of the asymmetry of the distribution for the signal with and without accidentals.

5.3.2 Clustering within one chamber

When a track passes through one chamber, it may hit 1,2,3 or 4 views (see fig. 5.9) depending on its impact point position. In order to compute the position of

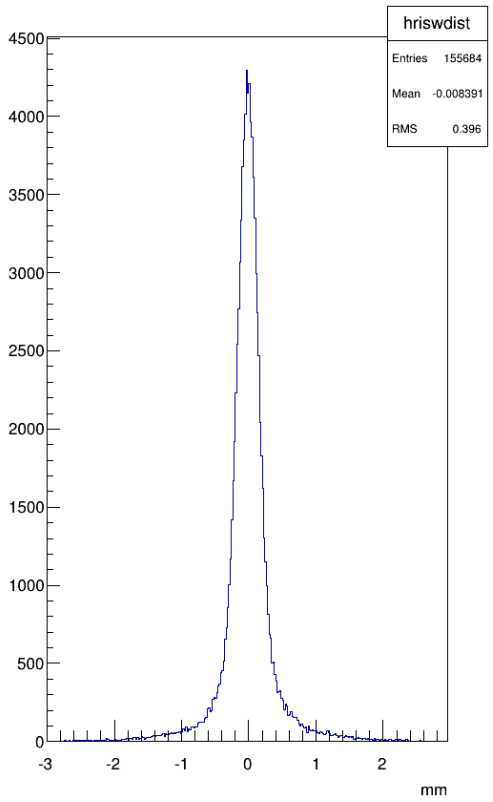

Figure 5.5: Difference between the average cluster position and the true particle position (MC truth) for simulated $\pi^+\nu\overline{\nu}$ events without accidentals.

the particle in the chamber, the clusters produced in the different views must be combined to obtain a space point.

All possible three and four view-combinations in each chamber are analysed.

Space point candidates in each station are obtained by computing the intersections of any possible x- and y-cluster combinations. For each such point the u- and v-projections are then computed; if at least one cluster in either u- or v-views is found within a fixed range distance ($D_{clustering}$) from such projections, the algorithm generates a three-dimensional space point. Clusters used to generate space point are flagged in order to be excluded from next cluster generation. The algorithm then performs the same operation using u- and v-cluster as starting point.

The time associated with each space point is the average of the trailing times of the clusters used in the combination (fig. 5.10).

We might add space points built by only two view-combinations (in the two view sector of the chamber only even if straw inefficiency and time resolution could bring to have two view-combinations in three view sector, see Figure 5.9) to increase spectrometer acceptance of about 3% (see fig. 5.11) but this would slow down the execution of the algorithm of order of 10 μs per event.

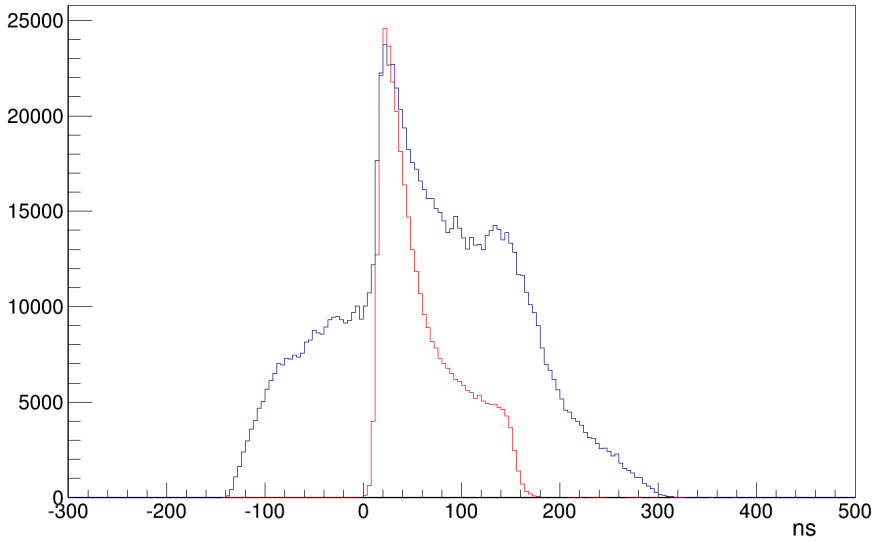

(a) Hit leading time distribution for simulated $\pi^+\nu\overline{\nu}$ events with (blue) and without (red) accidentals.

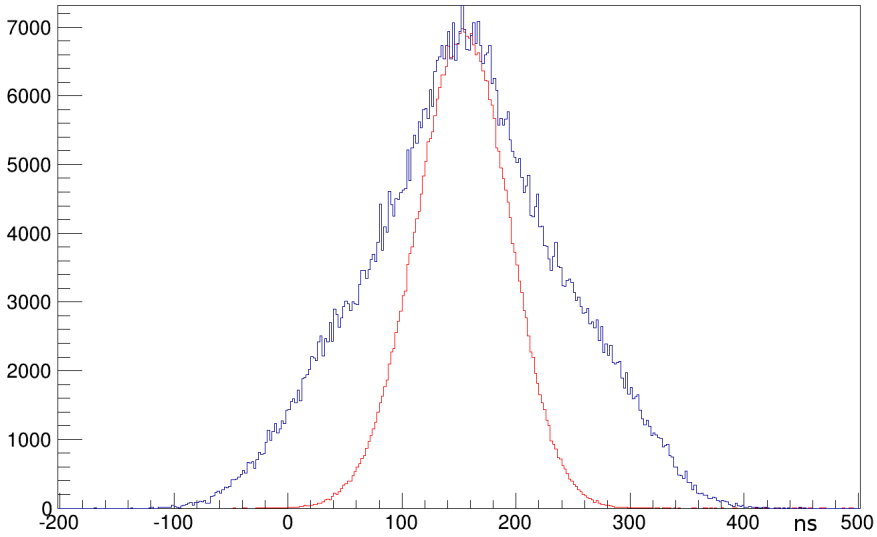

(b) Hit trailing time distribution for simulated $\pi^+\nu\overline{\nu}$ events with (blue) and without (red) accidentals.

Figure 5.6

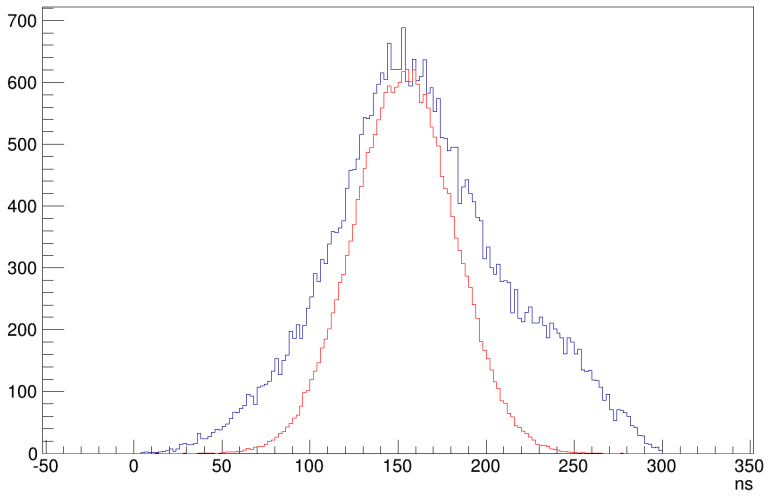

Figure 5.7: View-cluster trailing time distribution for simulated $\pi^+\nu\overline{\nu}$ events with (blue) and without (red) accidentals.

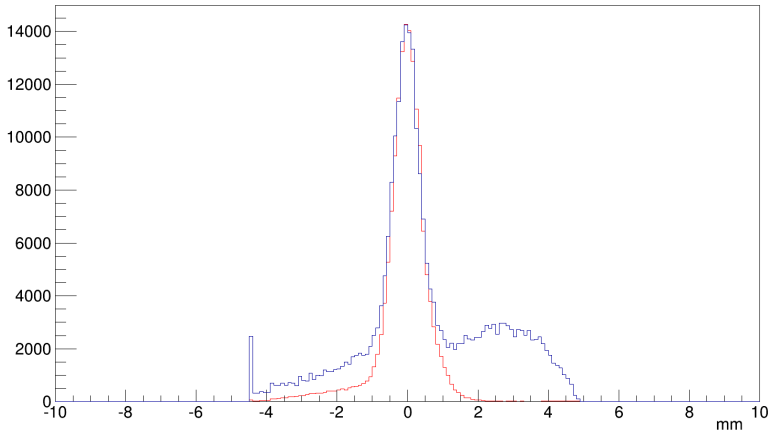

Figure 5.8: $r_a + r_b - 4.4$ mm distribution for simulated $\pi^+\nu\overline{\nu}$ events with (blue) and without (red) accidentals; The accumulation point at -4.4 mm is due to a cut off in the function that computes the radius from the leading time: to all negative leading times below 0 ns (due to the leading time resolution) a distance to the wire of 0 mm is associated.

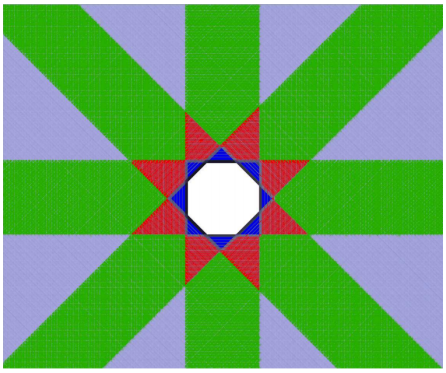

Figure 5.9: Sketch of the central part of a chamber where the chamber sectors with different expected numbers of crossed views are shown. White: beam hole; Blue: 1-view; red: 2-views; green: 3-views; violet: 4-views.

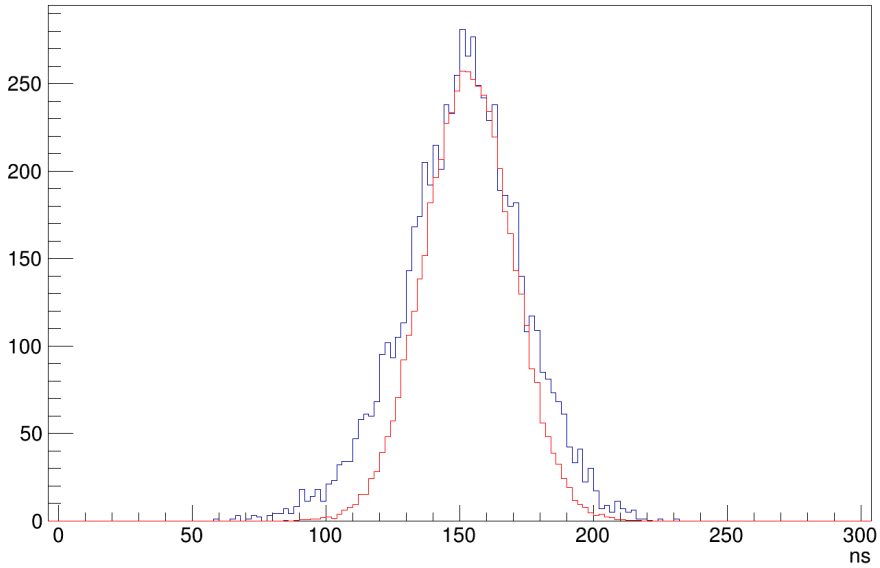

Figure 5.10: Space point trailing time distribution for $\pi^+\nu\overline{\nu}$ events with (blue) and without (red) accidentals.

5.3.3 Pattern recognition of the tracks

After clustering a pattern recognition algorithm is executed. The algorithm performs a two-dimensional (y,z) Hough transform, a technique that permits the identification of geometric patterns[52]. I use only two dimensions (the non bending transverse coordinate) to avoid the effect of the magnetic field and work with straight tracks. At the end of the pattern recognition step the information on the second transverse coordinate is added to compute the magnetic bending and the particle momentum.

The Hough transform converts the two-dimensional projection (y,z) of each point into a sheaf of straight lines $y = m_y * z + q_y$, which corresponds to a single line in the parameter space (m_y, q_y). A bidimensional histogram for the parameters m_y and q_y of the tracks, with 160 (0.2 mrad wide, [-40,40] mrad interval) $\times$ 200 (10 mm wide, [-1000,1000] mm interval) bins is created. For each line in the

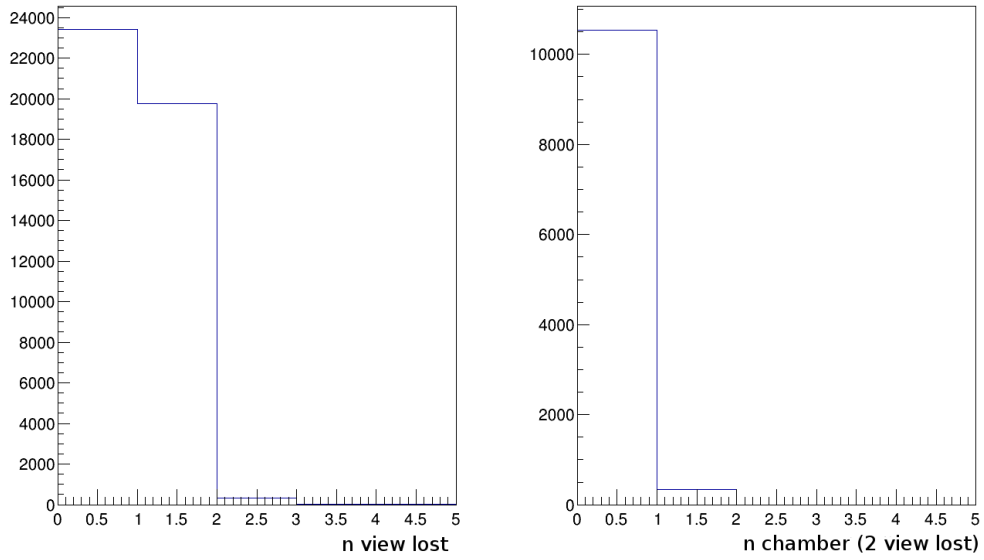

Figure 5.11: Distribution of the number of lost view (when the particle crosses the hole of the view) and distribution of the number of chambers in which the particle crosses only 2-views, for $\pi^+\nu\overline{\nu}$ events and $\sigma_{trailingtime} = 40ns$.

parameter space, the algorithm increases by one the value of all the crossed bins and saves the information on the related space point in a structure linked to the histogram. Once the histogram is filled, the algorithm looks for accumulation bins (i.e. the portions of the histogram where intersection points of three or four lines are located); the accumulation bins yield the parameters m_y and q_y of candidate tracks. An example of this technique is shown in figure 5.12, where each point in the (y, z) space (figure a) corresponds to a line of the same colour in the (m_y, q_y) space (figure b).

The algorithm scans all the bins, searching for those that have at least 2 entries and that contain points related to different chambers in the linked structure. The algorithm then scans the neighbouring bins (all the 8 bins around the central one) looking for some entries belonging to the remaining chambers not yet used. The sum of the entries in the selected bins should be 3 or 4, because we reconstruct only tracks composed by 3 or 4 points of different chambers.

Considering that more hits, belonging to the same chamber, could generate lines that cross the same accumulation area, the algorithm creates one candidate track for each combination of the points that it finds in the area (fig. 5.13). Most of the tracks created in this way are fake tracks and the algorithm must identify the true ones among those.

The algorithm evaluates the parameters of each candidate track:

- (m_y, q_y): slope and intersection at the z coordinate of the magnet, for y projection;

- $(m_{1x}, m_{2x}, q_{1x}, q_{2x})$: slope and intersection at the z coordinate of the magnet for x projection, where the tracks are divided in two straight segments (tracklets) by the effect of magnet;

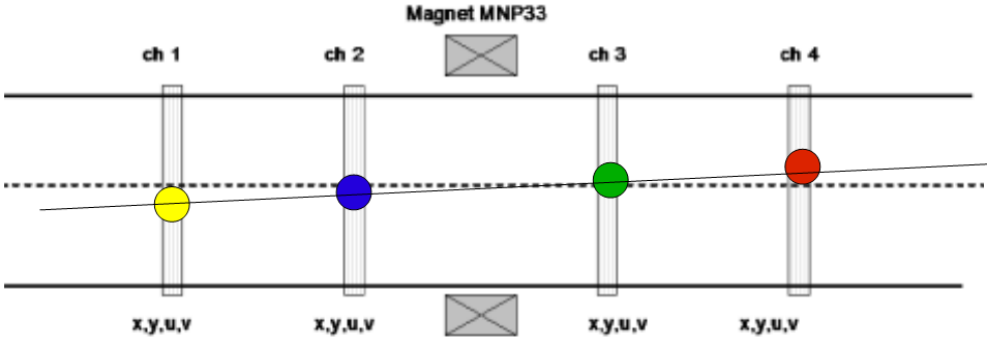

(a) Space points produced by a track (continuous line) in the STRAW spectrometer. The dotted line is the beam axis.

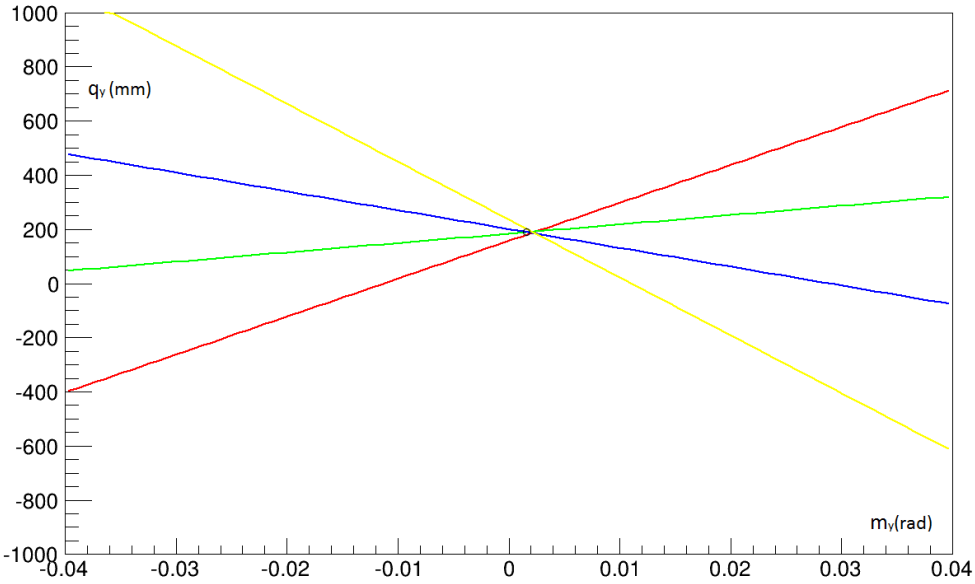

(b) lines corresponding to the coloured clusters in figure (a). The accumulation bin corresponds to the actual track parameters.

Figure 5.12: Example of Hough transform for a single-track event with 4 clusters.

- the position of the decay vertex along z using a Closest Distance Approach (CDA) algorithm between the candidate tracks and the nominal beam direction;
- P_z: the longitudinal momentum is computed using the approximation that the magnetic field effect is a momentum kick of 270 MeV/c ($P_z = |270\text{ MeV}/(m_{x2} - m_{x1})|$, where m_{x1} and m_{x2} are the horizontal slopes of the tracks before and after the magnet).

I use these informations to cut the fake tracks caused by combinations of hits generated by different particles:

- $Q_{low} < q_{2x} - q_{1x} < Q_{high}$ (tracklets should be connected at the magnet: ideally $q_{2x} - q_{1x}$ should be equal to 0);
- the temporary track should pass through the MUV2;

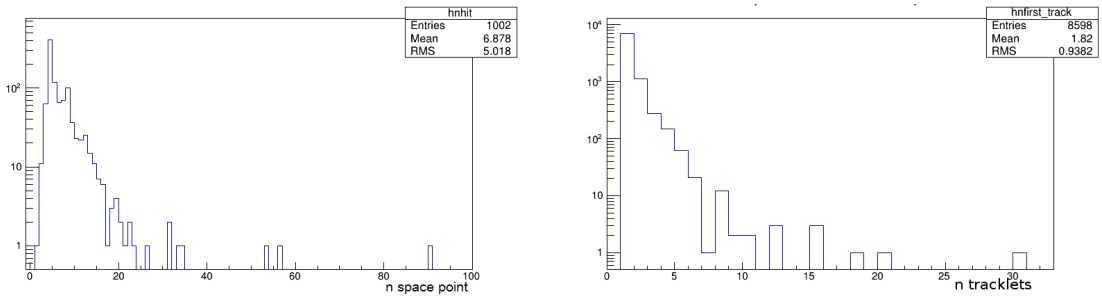

Figure 5.13: Distribution of the number of space points per event and of the number of tracklets reconstructed for each accumulation point, for simulated $\pi^+\nu\overline{\nu}$ events with accidentals and a trailing time resolution of 40 ns.

- T_{low} < average of the cluster trailing times of the temporary track < T_{high}.

The value of each cut parameter will be discussed in the next section. In fig. 5.14 the number of tracks per event that remain after the above cuts is shown.

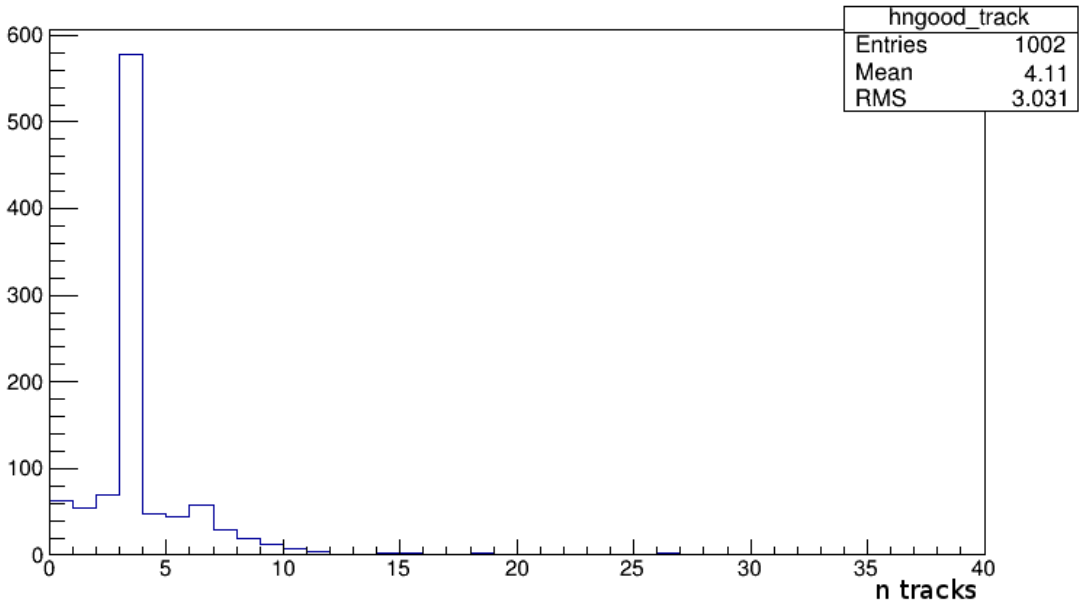

Figure 5.14: Distribution of the number of tracks per event after the first cuts, for simulated $\pi^+\nu\overline{\nu}$ events with accidentals and a trailing time resolution of 40 ns.

Some fake tracks aren't removed by the above cut, so there are many tracks that share one or more space points: the algorithm must identify the real tracks among others. To do this, it considers the tracks obtained with 4 space points that share at least 2 points and compares the value of $|q_{2x} - q_{1x}|$ keeping only the track with the smaller value. Then it merges the chosen candidate tracks with others who share all the space points (averaging the track parameters) and removes the tracks obtained with 3 space points that share at least 1 cluster with those. Similarly, the algorithm then chooses the best remaining tracks with 3 points, looking for those that have more points in the central bin or a smaller

CDA, in case they have the same number of point central bin. Thus, it merges these chosen tracks with those which have the same cluster (averaging the tracks parameters). The tracks that share with the chosen tracks at least 2 points or 1 point if located in the central bin are removed. Merged tracks and the tracks which are not removed proceed to the next step (fig. 5.15).

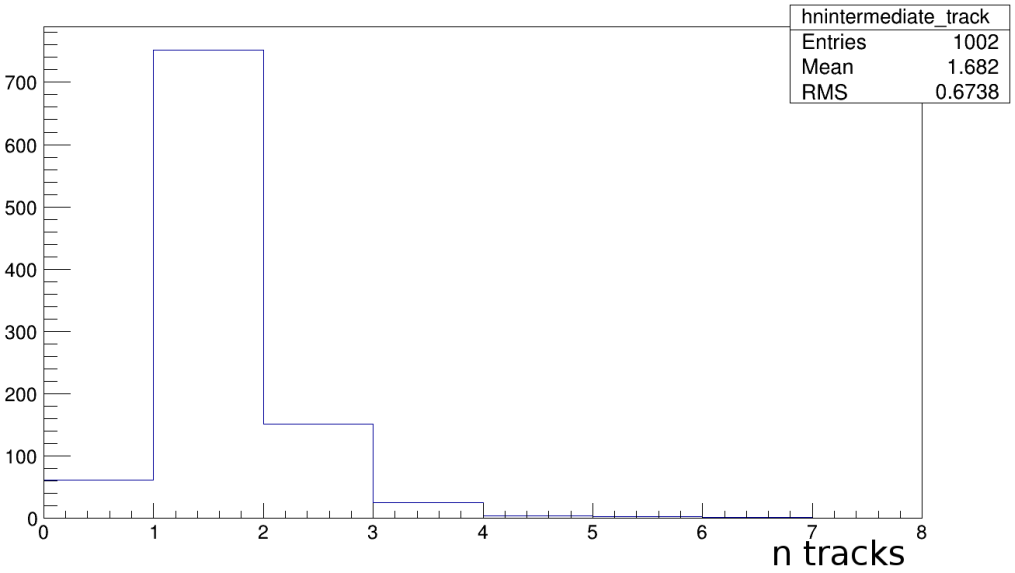

Figure 5.15: Distribution of the number of tracks per event after the second step, for simulated $\pi^+\nu\overline{\nu}$ events with accidentals and a trailing time resolution of 40 ns.

In the last step, the algorithm removes the tracks which share the space points with other tracks and it applies two physical cuts to the tracks:

- $P_1 < P_z < P_2$
- $z_1 < z_v < z_2$

where z_v is the z coordinate of the track vertex.

Finally, to improve the rejection of $K^+ \to \pi^+\pi^+\pi^-$ events, the algorithm removes all the events that have one track with a positive x slope and another with a negative one. This cut reduces the signal efficiency by about 0.7% but improves the rejection of $\pi^+\pi^+\pi^-$ events from a factor 1.9 to a factor 3.7 therefore reducing the total rate by about 9 KHz.

Fig. 5.16 shows the distribution of final number of tracks per event.

5.4 The parameters

The algorithm parameters are chosen in order to maximise the algorithm efficiency for events of $\pi^+\nu\overline{\nu}$ with accidentals and to reduce background rate. I show, as an example, only a few plots obtained by scanning one parameter at a time while keeping the other parameters fixed (see figure 5.17).

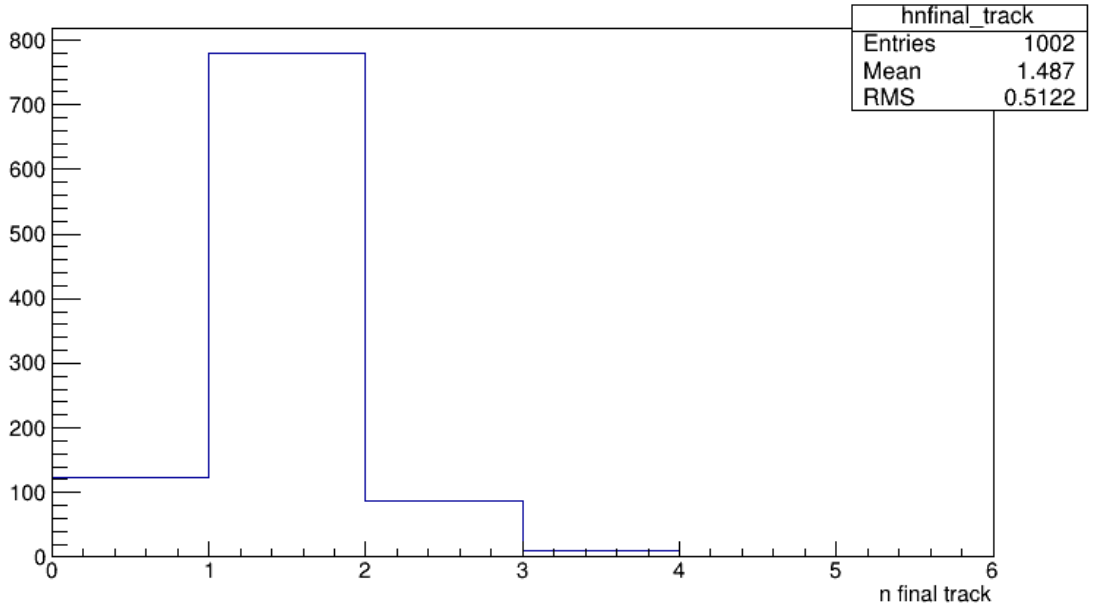

Figure 5.16: Distribution of the number of final tracks per event, for simulated $\pi^+\nu\overline{\nu}$ events with accidentals and a trailing time resolution of 40 ns

	lower limit	upper limit
leading time	T1 = 0.0 ns	T2 = 140 ns
hit trailing time	T3 = 40 ns	T4 = 270
$r_a + r_b - 4.4$ mm	CUT_{low} = -2.4 mm	CUT_{high} = 2.6 mm
clustering range	no low cut	$D_{clustering}$ = 6 mm
track trailing time	T_{low} = 120 ns	T_{high} = 180 ns
$q_{2x} - q_{1x}$	Q_{low} = -30	Q_{high} = 20

Table 5.1: table of algorithm cuts

Table 5.1 lists the values chosen for each parameter of the algorithm.

For what concerns the physical cuts (that is particle momentum and decay vertex), I choose to not maximise the background rejection (fig. 5.19) to be safer in not introducing any bias on the signal, despite the excellent resolution achieved (see figure 5.18) for the longitudinal momentum (~ 0.66 GeV/c) and for the decay vertex (~ 1.9 m); so I use the following values for the longitudinal momentum and the longitudinal z_v decay vertex:

- 10 GeV/c $<$ P_z $<$ 40 GeV/c
- 90 m from target $<$ z_v $<$ 180 m from target

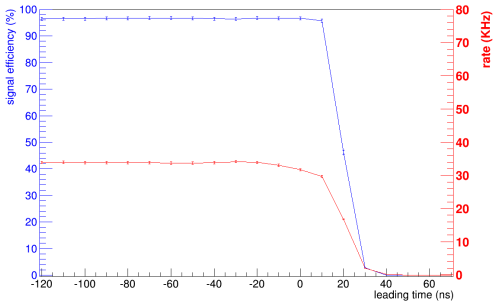

(a) Scan over the leading time lower cut T1.

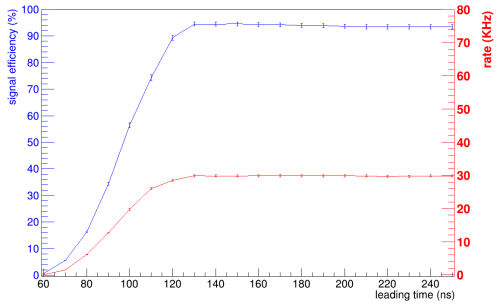

(b) Scan over the leading time upper cut T2.

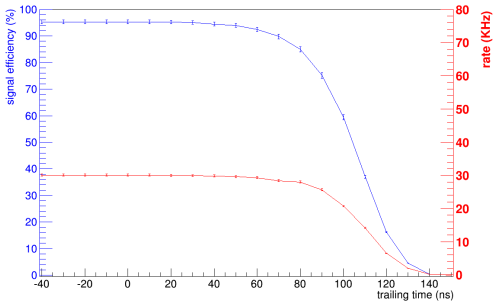

(c) Scan over the trailing time lower cut T3.

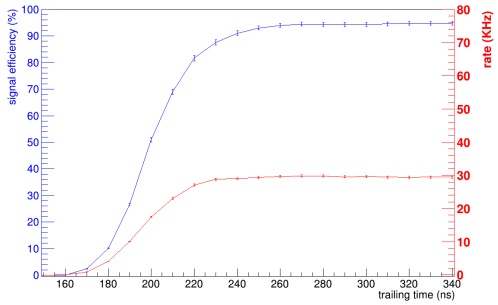

(d) Scan over the trailing time upper cut T4.

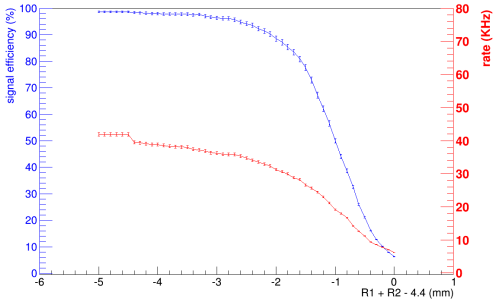

(e) Scan over the lower cut of the $r_a + r_b - 4.4$ mm distribution (see eq. 5.2).

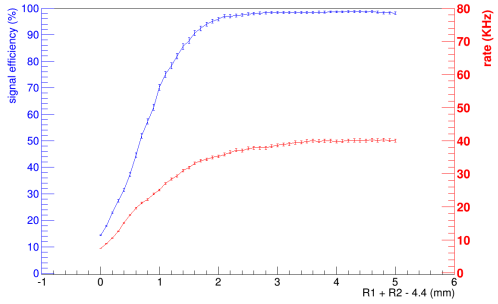

(f) Scan over the upper cut of the $r_a + r_b - 4.4$ mm distribution (see eq. 5.2).

Figure 5.17: Algorithm efficiency for signal events with accidentals (bloe dots, left scale) and estimated trigger rate (red dots, right scale) as a function of different values of cut limits.

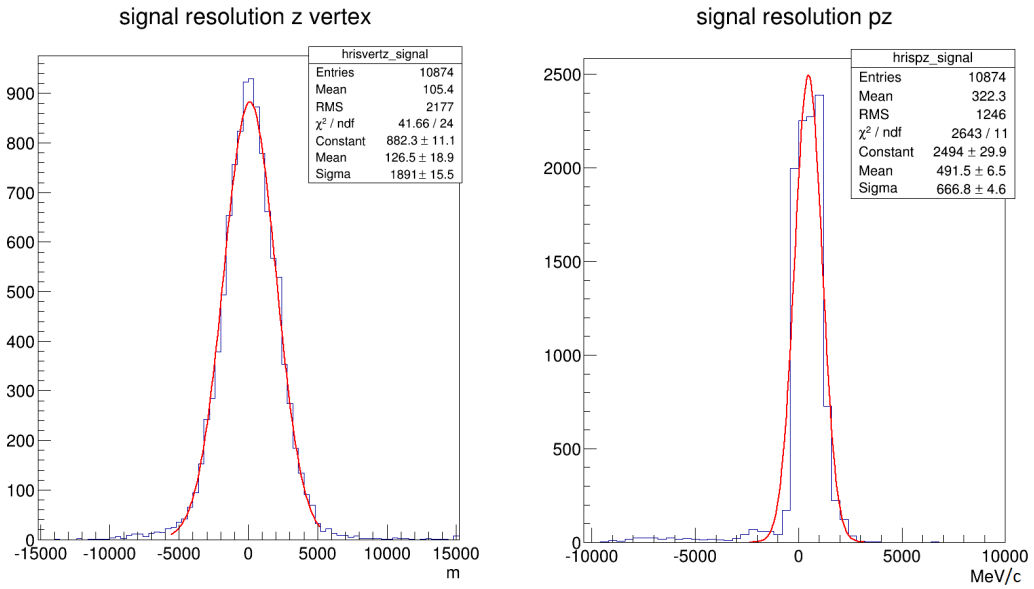

Figure 5.18: Distribution of the difference between reconstructed and generated decay vertex longitudinal position, and between reconstructed and generated longitudinal momentum; for simulated $\pi^+\nu\overline{\nu}$ events with accidentals and a trailing time resolution of 40 ns.

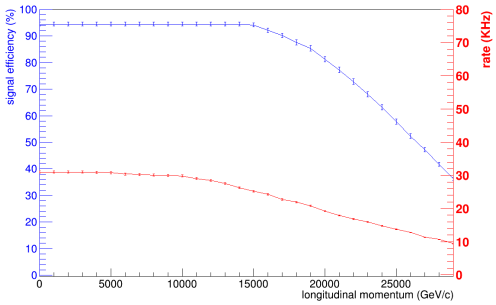

(a) Scan over the longitudinal momentum lower cut P_1.

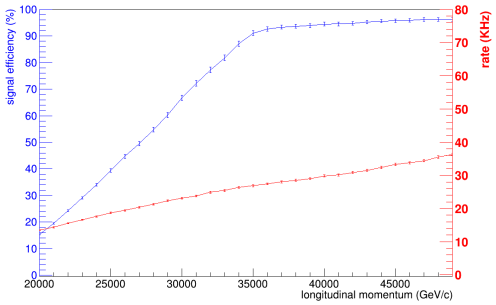

(b) Scan over the longitudinal momentum upper cut P_2.

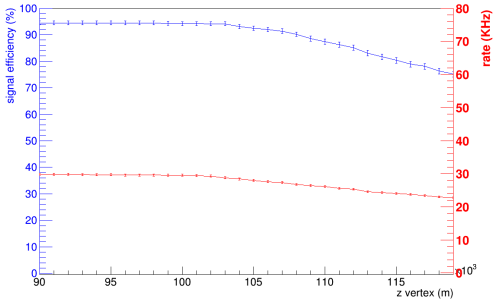

(c) Scan over the z decay vertex lower cut z_1.

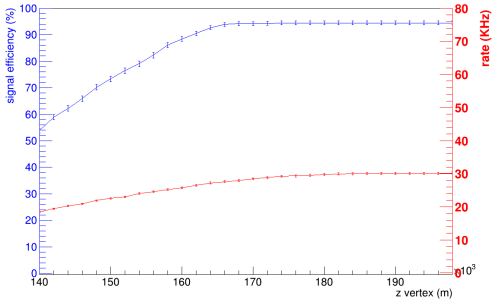

(d) Scan over the z decay vertex upper cut z_2.

Figure 5.19: Algorithm efficiency for signal events with accidentals (bloe dots, left scale) and estimated trigger rate (red dots, right scale) as a function of different values of physical cut limits.

5.5 Conclusions on the STRAW simulation

This algorithm is satisfactory since, as shown in table 5.2, we obtain a good signal efficiency $(94\% \pm 1)\%$ and a total background rejection factor of about 4 without considering the upstream muon and the beam pion components which will be also rejected. The output rate after this L1 STRAW algorithm are computed according to the Pre-RUN L0 simulation (see fig 4.1) discussed in the section 4.1.

Process	rejection factor	L0 simulated rate (kHz)	Rate simulation after STRAW L1 (kHz)
$K_{\mu 2}$	4.9	11.3 ± 1.5	2.3 ± 0.1
$K_{\mu 3}$	3.3	6.9 ± 0.3	2.1 ± 0.1
K_{e3}	2.6	12.9 ± 0.5	4.9 ± 0.1
$\pi^+\pi^0$	5.3	39 ± 1	7.4 ± 0.1
$\pi^+\pi^+\pi^-$	3.7	34.4 ± 0.8	9.3 ± 0.2
$\pi^+\pi^0\pi^0$	4	1.2 ± 0.1	0.3 ± 0.1
Muons upstream (90% confidence level)	>13.9	22 ± 5	<1.6
Beam π^+ (90% confidence level)	>4.8	48 ± 5	<10
Total	>4.7	179 ± 8	<37.9
Signal efficiency	(94 ± 1) %		

Table 5.2: Algorithm results

5.6 Algorithm fine-tuning with 2015 data

As already said in the previous chapter (see section 4.2) the 2015 RUN showed that real conditions are in part different from the simulation. In particular for the STRAW detector the straw response to the particle passage was not satisfactorily simulated (e.g. the trailing time shape) and the accidental impact on the STRAW time windows was much larger than expected. So we studied the developed algorithm with real data, starting from the results of the L0 and the other L1 algorithms described in sections 4.3.1 and 4.4. The data samples used are listed in the table 4.1; more importance will be given to the data sample of run 4098 because its intensity (about 60 % of the nominal) allows a better understanding of the 2016 run condition and a better evaluation of the accidentals at high beam intensities.

To evaluate the accidentals effect on the STRAW detector with real data, figure 5.20a and 5.20b show the number of hits revealed in the detector in the 400 ns STRAW time windows (between -100 ns and +300 ns around the trigger

time) respectively for run 3809 (about 0.6 % of the nominal intensity) and 4098 (about 60 % of the nominal intensity). Figure 5.20b could be compared with the

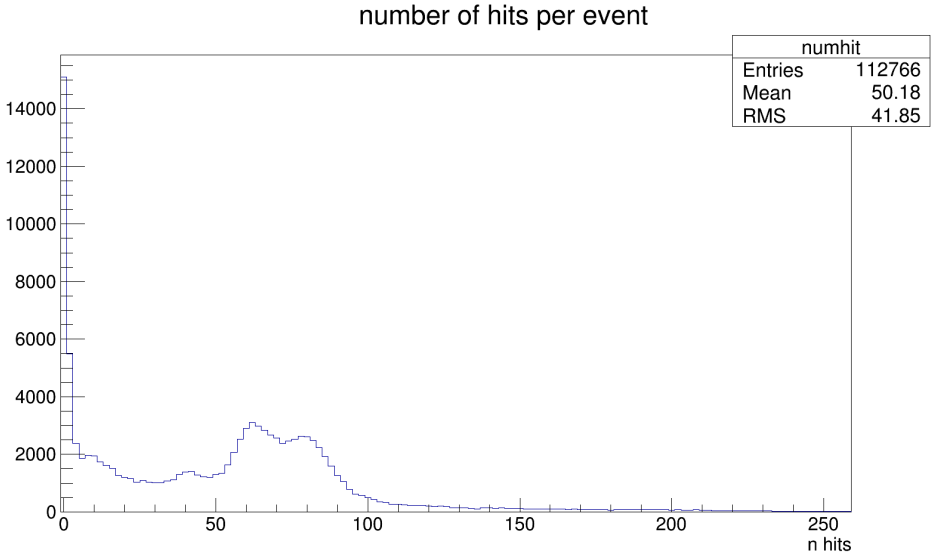

(a) Run 3809: $\sim 0.6\%$ of the nominal intensity.

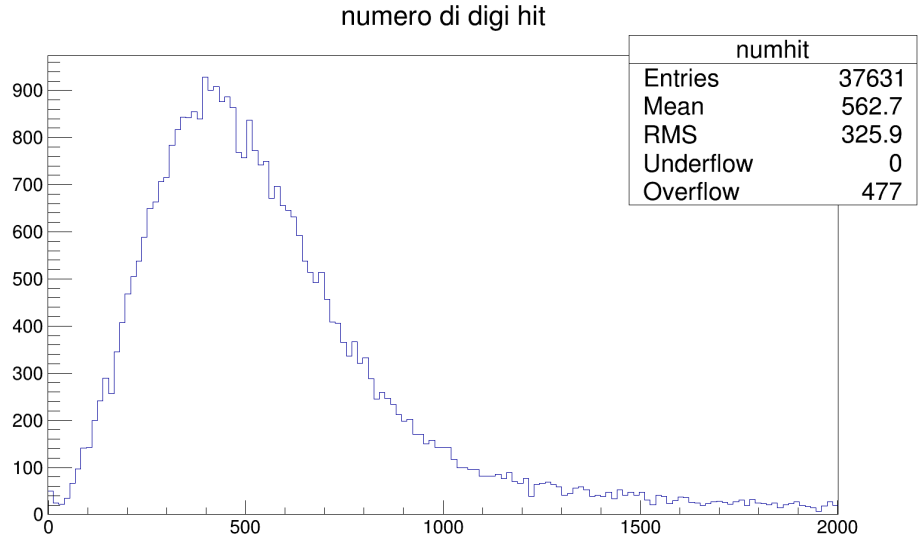

(b) Run 4098: $\sim 60\%$ of the nominal intensity.

Figure 5.20: number of hits in the STRAW detectors in a 400 ns around the trigger time during the 2015 run.

number of hits in the spectrometer obtained in the simulation with accidentals (see figure 5.1b). The time window of the simulation was 320 ns instead of 400 ns but the beam was simulated at full intensity: real data show about a factor five more hits with respect to the simulation. The large multiplicity of hits decreases the reconstruction capability of the algorithm thus requiring a fine-tuning of the parameters and of the algorithm structure.

Figures 5.21 and 5.22 show the leading time and trailing time distributions at $\sim 0.6\%$ and $\sim 60\%$ of the nominal intensity; new time windows used in the

algorithm to select only the hits in time with the L0 trigger are shown between the red lines.

- 0 ns $<$ leading time $<$ 175 ns
- 55 ns $<$ trailing time $<$ 250 ns

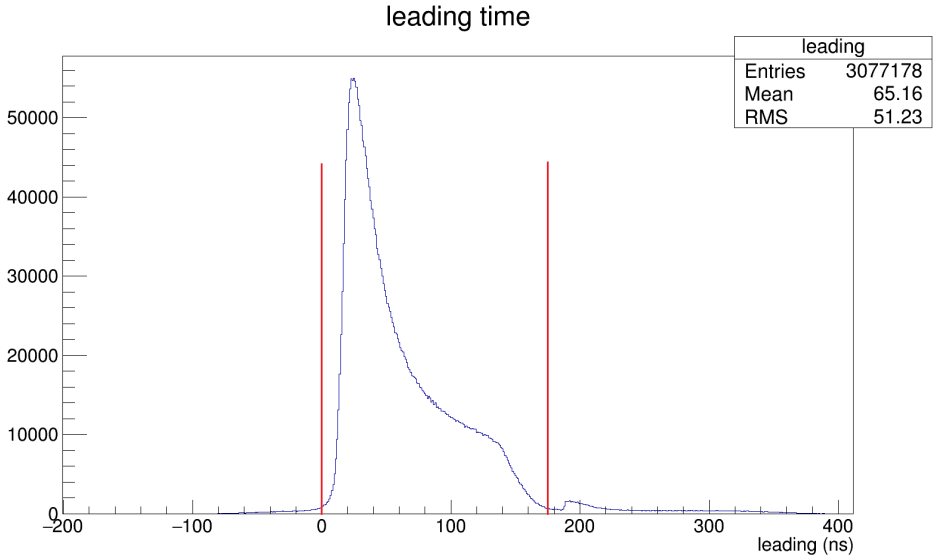

(a) RUN 3809: $\sim 0.6\%$ of the nominal intensity.

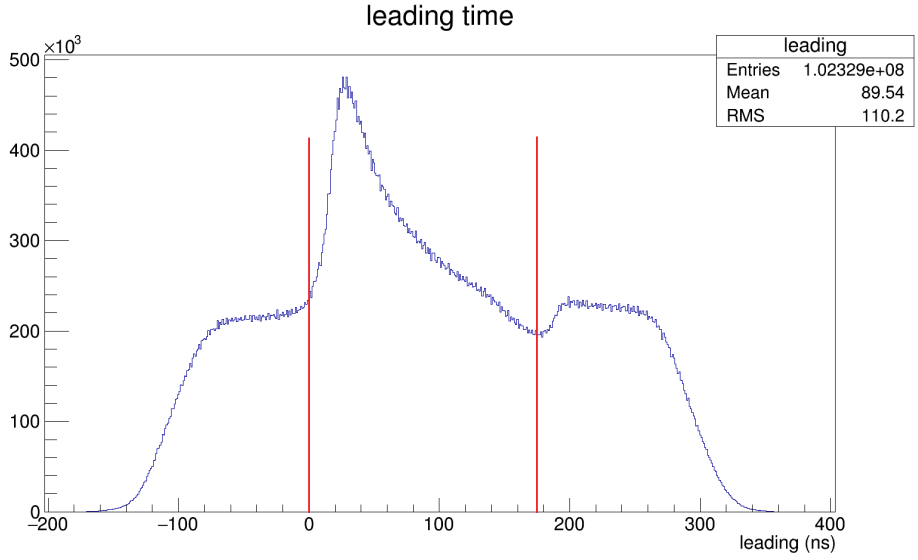

(b) RUN 4098: $\sim 60\%$ of the nominal intensity.

Figure 5.21: Hit leading time distributions for two runs; the two red lines identify the time selection.

There are three main differences and improvements with the STRAW algorithm described previously:

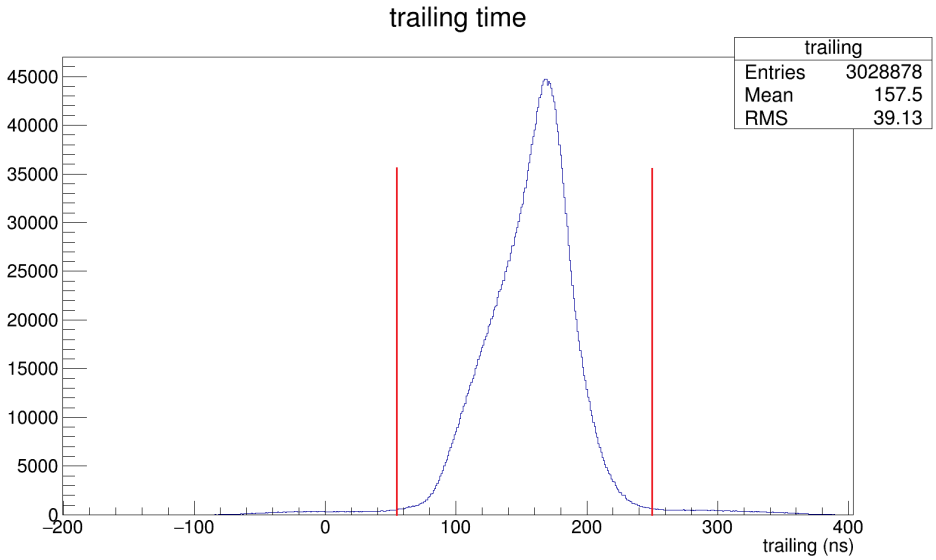

(a) RUN 3809: $\sim 0.6\%$ of the nominal intensity.

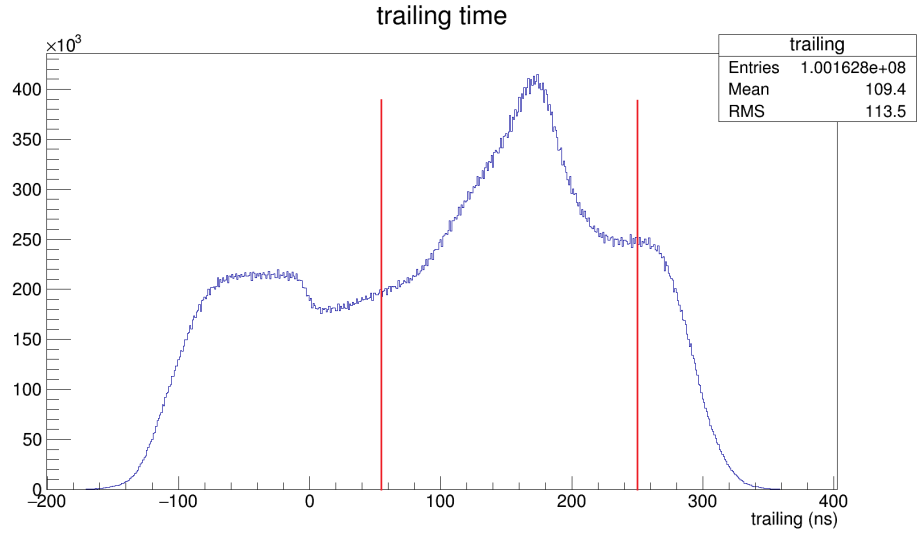

(b) RUN 4098: $\sim 60\%$ of the nominal intensity.

Figure 5.22: Hit trailing time distribution for two runs; the two red lines identify the time selection.

- The huge number of hits made forced us create view clusters even with the combination of 3 straws: the use of the 3 straws case allows to reduce the possible combinations of 2 view clusters reducing both the possibility to create fake clusters and the execution time. There are four possible 3 hits clusters (see figure 5.23) but in any case two straws are hit near the edge (like straws a and b in figure) and one is hit in the middle (straw c in figure). So, while the sum of the wire distance $r_a + r_c$ (r_a is the distance between the hit a and the closest wire) is about 4.4 mm like for $r_b + r_c$, for $r_a + r_b$ it is about 8.8 mm. This helps us to make a clean selection of these three straw clusters.

- In the chamber clustering step and only for the two view zones, space points obtained by only two view-combinations are added. This was done not to decrease the spectrometer acceptance and reconstruction efficiencies. The loop to build the 2 view-clusters is done after the reconstruction of the 3 and 4 view-clusters to reduce the number of possible 2 view-combinations and to speed-up this part of the algorithm. The search is made only in the 2 view zones, to limit the number of additional fake clusters.

- A selection step for space points was added: if two or more space points share at least one view-cluster, the one with a better clustering range ($D_{clustering}$ see section 5.3.2) will be chosen.

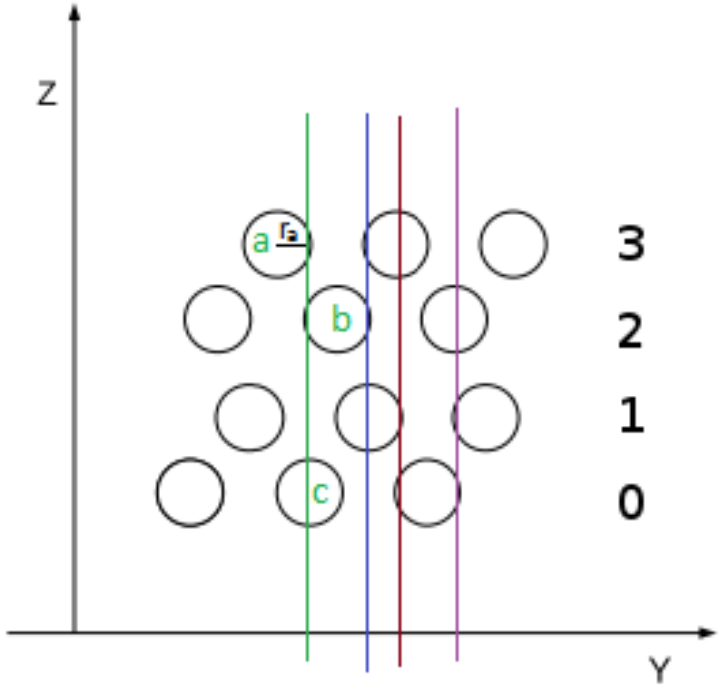

Figure 5.23: Types of three hit clusters.

The algorithm parameters after the fine-tuning are shown in the table 5.3.

	lower cut	upper cut
leading time	T1 = 0.0 ns	T2 = 175 ns
hit trailing time	T3 = 55 ns	T4 = 250
$r_a + r_b - 4.4$ mm (2 hits view clusters)	CUT_{low} = -1.5 mm	CUT_{high} = 1.4 mm
$r_a + r_b - 8.8$ mm (3 hits view clusters)	CUT_{low} = -0.2 mm	CUT_{high} = 0.2 mm
clustering range (chamber cluster)	no low cut	$D_{clustering}$ = 6 mm

Table 5.3: table of algorithm cuts

Cuts on the track times (the average of the trailing times of all the track hits) and on $q_{2x} - q_{1x}$ were no longer necessary with real data. Indeed the reconstructed tracks are already well selected in time: as we can see in figure 5.24 there are no large differences between the track time distribution in run 3809 where the accidental activity is negligible ($\sim 0.6\%$ of the nominal intensity) and in run 4098 ($\sim 60\%$ of the nominal intensity).

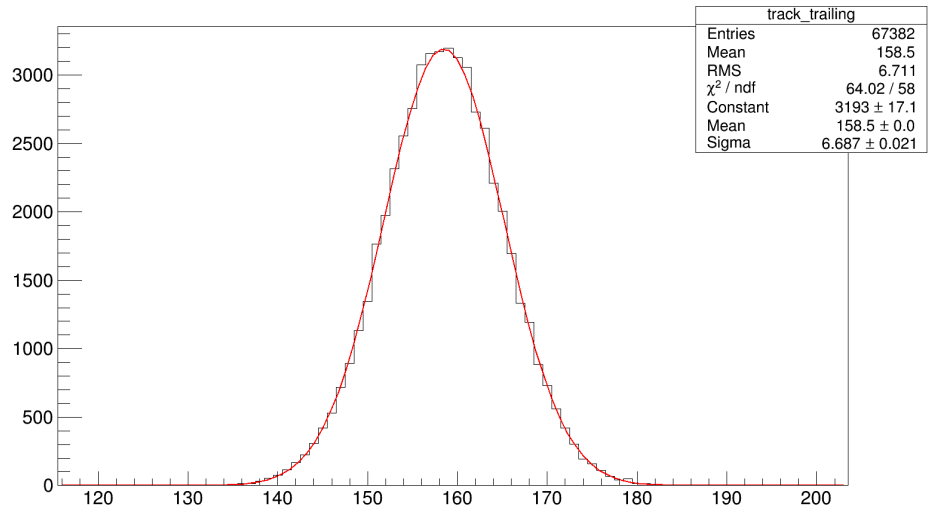

(a) Run 3809: $\sim 0.6\%$ of the nominal intensity.

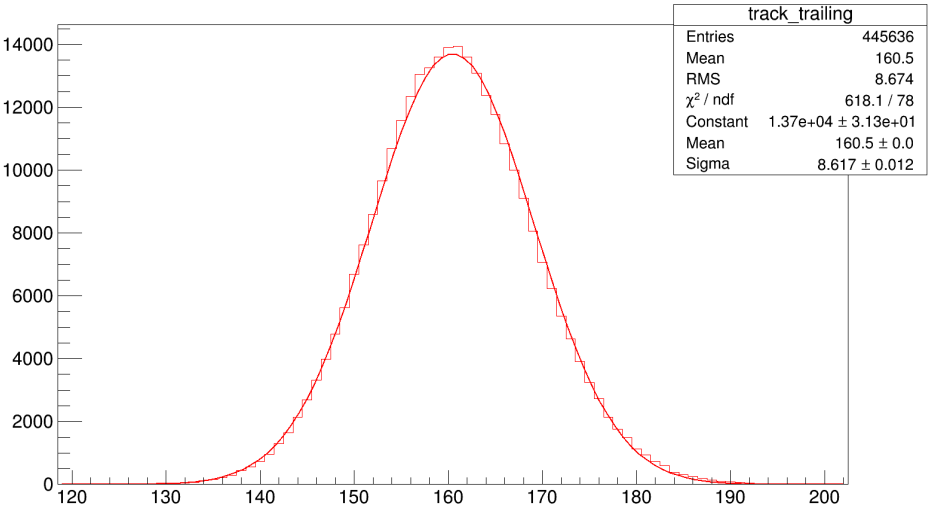

(b) Run 4098: $\sim 60\%$ of the nominal intensity.

Figure 5.24: Time distributions of the candidate tracks (before the physics cuts are applied) for two runs. The time of the tracks is obtained by the average of trailing time of all the track hits.

5.7 Algorithm trigger condition

After track reconstruction, this STRAW L1 Algorithm rejects all events without at least one track defining a decay vertex within 180 m from target, CDA < 200 mm and $P_z < 70$ GeV/c (see figures 5.25 and 5.26).

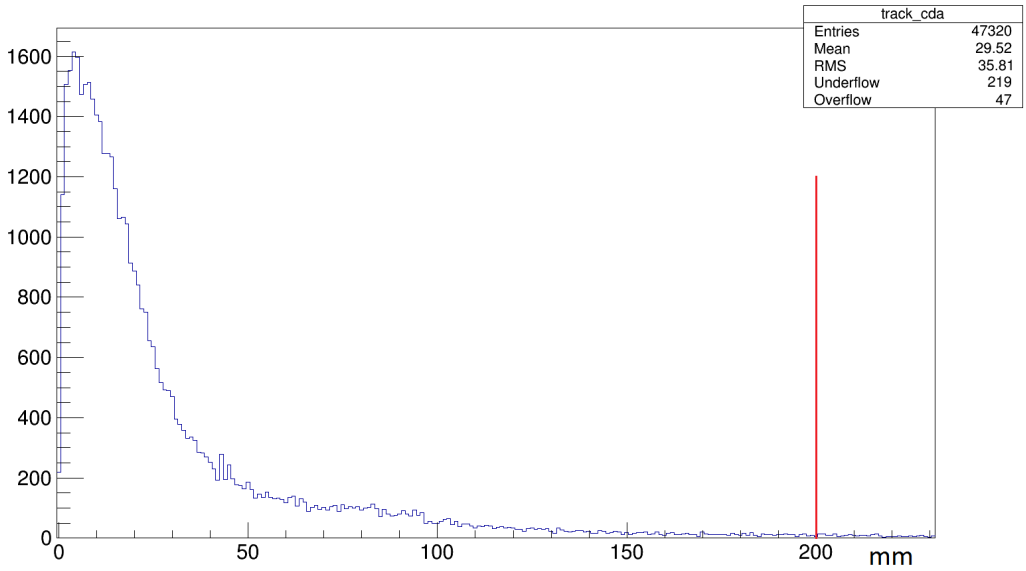

Figure 5.25: Distribution of the CDA of the tracks with the nominal beam direction for RUN 4098 ($\sim 60\%$ of the nominal intensity).

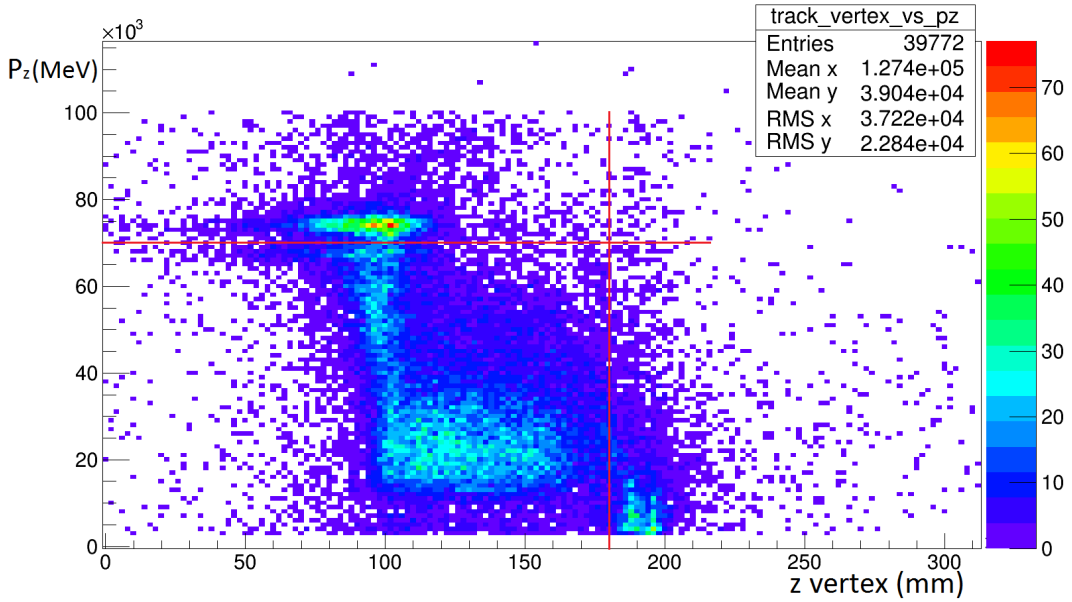

Figure 5.26: Track momentum vs longitudinal vertex (z_v), run 4098 ($\sim 60\%$ of the nominal intensity).

These cuts are chosen far from the regions that will be used in the analysis (15 GeV/c < track momentum < 35 GeV/c and 105 m < z_v < 165 m from the target) to not lose good signal events due to resolution effects (momentum resolution is about 3 GeV/c and the z_v resolution is about 5 m). A comparison of the tracks reconstructed by this L1 STRAW algorithm and by the official NA62 analysis is done to validate the algorithm. The comparison shows a good agreement of the reconstructed tracks as can be seen in figures 5.27 and 5.28.

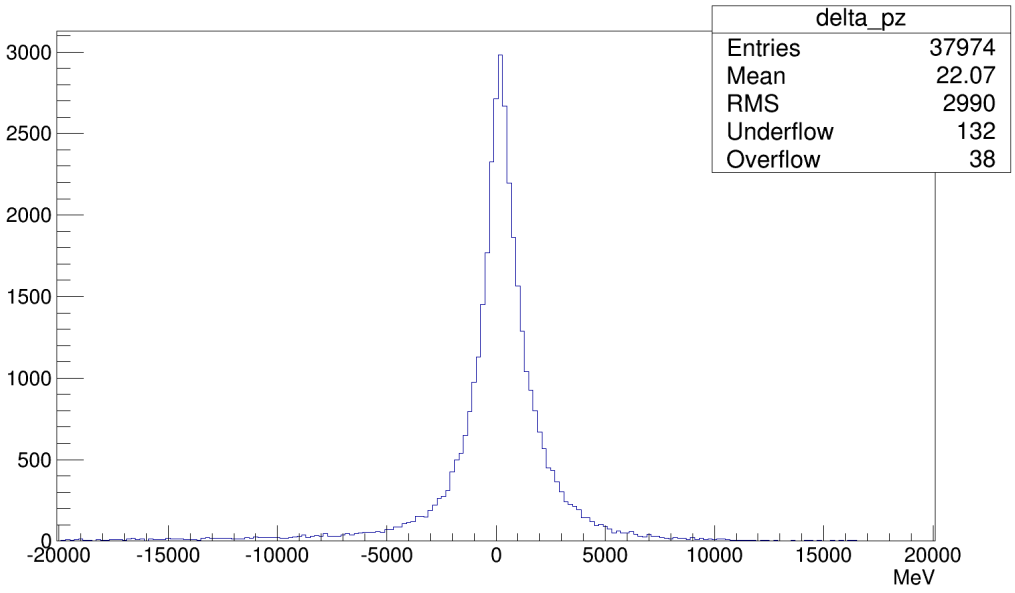

Figure 5.27: Difference between the longitudinal momentum for tracks reconstructed by the L1 algorithm and by the official NA62 Analysis software. Run 3809 ($\sim$ 0.6% of the nominal intensity).

The good longitudinal momentum resolution of the tracks can allow to bring the upper momentum cut up to 50 GeV/c, thus reducing the output rate of the L1 trigger further.

Moreover, for each event with more than one track, the CDA among the two tracks is computed to select and reject multi-body decays. Each combination of two tracks that satisfies the condition CDA < 30 mm is removed. If no other tracks remain, the event will be rejected.

Figures 5.29a and 5.29b show vertex positions for the rejected multi-body decay: as expected, vertexes are located along the beam line and in proximity of the STRAW chambers, since they are likely due to particle interactions with the straws material.

5.8 Algorithm results

We summarize here the physics cuts applied on the tracks.

- P_z < 70 GeV/c

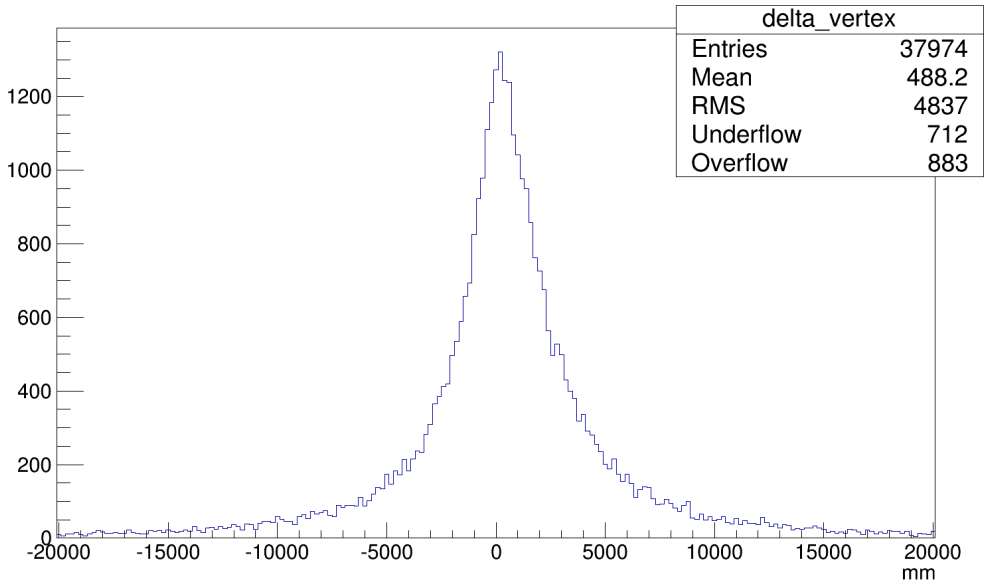

Figure 5.28: Difference between the vertex longitudinal position reconstructed by the L1 algorithm and by the official NA62 Analysis software. Run 3809 ($\sim 0.6\%$ of the nominal intensity).

- z_v $<$ 180 m from target
- CDA vertex $<$ 200 mm
- no track identified as belonging to a multi-body decay (all CDA between tracks $>$ 30 mm)

Figure 5.30 shows the results of the L1 STRAW trigger algorithm on the data samples listed in section 4.2 after the application of the L0 and L1 conditions (see chapter 4).

Depending on the Run number, and therefore on the beam intensity, the fraction of rejected events varies from 48% to 57%, reaching a rejection factor of about 2.3. In figure 5.30 the rejection factor obtained using the multi-body cut (see previous physics cuts summary) is also included (from 12% to 16%).

The very different rejection factor for run 4098, as already mentioned in the section 4.3.3, is due to the L0 trigger condition used to collect the data sample: instead of a simple CHOD condition of geometrical acceptance a tight LKr/MUV1 condition on the event energy was used at L0. Indeed if we don't consider the LKr/MUV1 condition we obtain about the same results for the L0 (between a factor 2 and 2.6).

The official NA62 off-line Reconstruction program was used to evaluate the algorithm inefficiency and *false positive* events[2]. The inefficiency is evaluated by looking at the events that have at least one track with the following properties in the NA62 Reconstruction:

[2] *False positives* are events accepted which L1 STRAW algorithm which don't satisfy at least one trigger condition when reconstructed with the more precise off-line Reconstruction program.

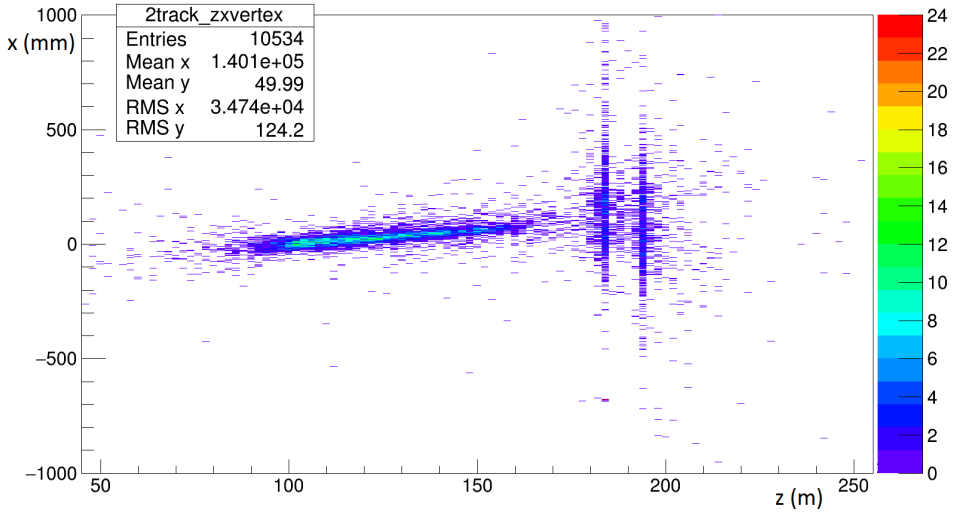

(a) (x,y) plane.

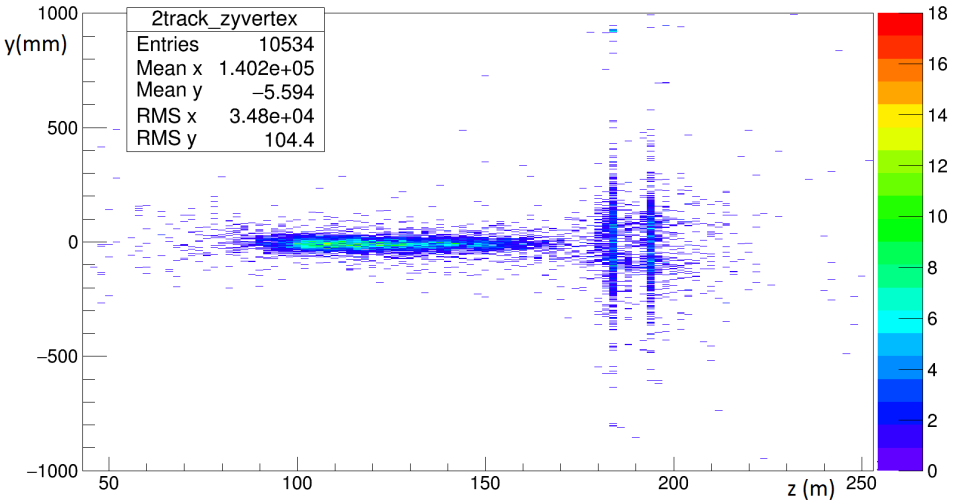

(b) (y,z) plane.

Figure 5.29: Decay vertex positions of the rejected multi-body decays.

- $P_z < 35$ GeV/c;
- 105 m from target $< z_v <$ 165 m from target;
- the track is built using one space point for each chamber;
- the track fit has a chi-square< 20;
- the track projection matches[3] with a CHOD or RICH Reconstructed candidate.

[3]Algorithm looks for CHOD candidate with x and y coordinate within $\pm$6 cm and timestamp within $\pm$30 ns from the track projection. In the same way it looks for RICH candidate with x and y angle within $\pm$1.5 mrad and timestamp within $\pm$30 ns from the track.

RUN NUMBER	Intensity	Fraction of cut events (track properties)	Fraction of cut events (3 track rejection)	Fraction of cut events (total)	Inefficiency (RECO event lost)	False Positives (non-RECO event accepted)
3809	~0.6%	~35%	~13%	~48%	~0.7%	~0.7%
4069	~12%	~35%	~16%	~51%	~3.1%	~0.7%
4098	~60%	~45%	~12%	~57%	~3.7%	~2.8%

Figure 5.30: Results of the L1 STRAW trigger algorithm.

The efficiency and purity decrease with increasing beam intensity due, to the accidental activity.

If we use a tighter cut om the longitudinal momentum ($P_z < 50$ GeV/c) the fraction of rejected events reaches 69%, or a rejection factor of about 3.2.

5.9 Computing time

An important test about this algorithm is related to its execution time. A L1 algorithm have to respect two conditions:

- it must cope with the average input rate of events;
- it must elaborate each event within the L1 latency.

While it is relatively easy to remain within the L1 latency, because the PC farm environment allows to keep data for the whole duration of the spill (several seconds), the challenge is to cope with the L1 input rate that will reach 1 MHz of average. The complete L1 trigger, composed at the moment by 4 algorithms (CHOD, LAV, KTAG and STRAW, see section 4.4), should elaborate one event in 1 μs in average. The CHOD, LAV and KTAG algorithms are faster than the STRAW algorithm because they require very simple conditions (the total execution time of this three algorithms is 50 μs in average), so it is better to execute them before the STRAW algorithm. In this way the input rate to the STRAW algorithm is reduced of about a factor 3. The PC farm is composed at present by 30 PCs and each one can schedule 16 concurrent processes. In conclusion the STRAW algorithm has about 1.3 ms on average to elaborate one event on a single PC process.

The algorithm implements a cut-off on the number of hits in an event to prevent running on very large events which would need a long time to be elaborated: events with more than 1500 hits are skipped by this algorithm and automatically sent to the L2 (accepted).

To estimate the actual algorithm execution time I ran it on a PC similar to those of the PC farm (but with less computing power). The average execution time measured was about 415 μs (see figure 5.31) that is within the requirement. For such test data of the run 4098 was used ($\sim$ 60% of the nominal intensity), results with other data samples are shown in figure 5.32 together with the fraction of skipped events due to the 1500 hits cut-off.

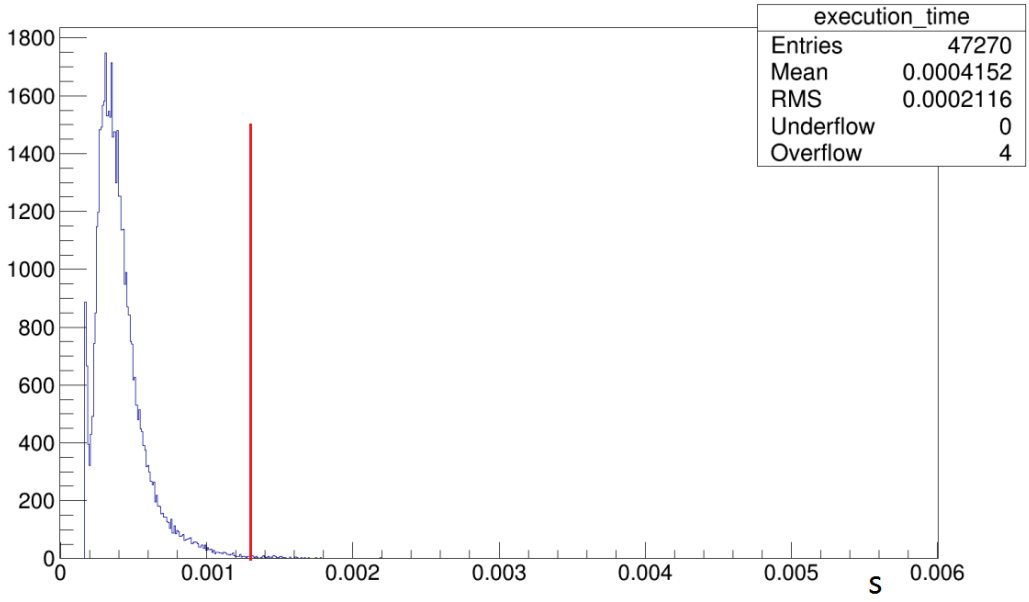

Figure 5.31: Distribution of the execution time of the L1 STRAW trigger algorithm using data of run 4098 ($\sim$ 60% of the nominal intensity).

RUN NUMBER	Intensity	Average Execution Time per Event	Skipped Events
3809	~0.6%	251 µs	0.02 %
4069	~12%	299 µs	0.06 %
4098	~60%	415 µs	3.7 %

Figure 5.32: Execution time results of the L1 STRAW trigger algorithm.

5.10 Summary of the L0 and L1 study

I can now put together the results of this L1 STRAW algorithm with the L0-L1 analysis of chapter 4 to verify the goal concerning the output rate (maximum 100 kHz). The expected event L0 input rate at nominal intensity is about 13 MHz so the L0 and L1 should provide a rejection factor of at least 130: a factor 13 should be obtained with the L0 to reach the design L1 input rate of 1 MHz, and a factor 10 has to be provided by the L1 trigger.

The total rejection factor obtained with L0 and L1, before the STRAW L1 algorithm is applied, is about between 23 to 34 so at least a further factor 5 is needed to reach the goal.

Figures 5.33 and 5.34 show a summary of the L0 and L1 study using two possible cut sets for the STRAW algorithm. The two sets differ only by the longitudinal momentum condition: $P_z < 70$ GeV/c or $P_z < 50$ GeV/c. The

tighter condition ($P_z < 50$ GeV/c) almost allows to reach the required rejection factor and the L1 output contribution (9.2 instead of 10).

Detector	Condition	Fraction of initial events (Rejection factor detector) (total rejection factor)		
		3809 only CHOD/2, 0.6%	4069 only CHOD/200, 12%	4098 LKr/14, 60%
CHOD	Al least 1 crossing	93% (1.08) (1.08)	87% (1.15) (1.15)	94% (1.06) (1.06)
LKr	$E_{cluster} > 1.2$ GeV & $E_{total} < 20$ GeV	24% (3.88) (4.17)	28% (3.11) (3.57)	79% (1.19) (1.27)
MUV1	$E_{cluster} > 5$ GeV			
RICH	N SuperCells > 3	16% (1.5) (6.25)	19% (1.47) (5.26)	63% (1.25) (1.59)
MUV3	At least 1 tight signal	13% (1.23) (7.69)	16% (1.19) (6.25)	48% (1.31) (2.08)
LAV12	At least 1 hit (both leading of low and high threshold)	10% (1.3) (10)	13% (1.23) (7.69)	41% (1.17) (2.44)
L0 Total Rejection Factor		10	7.7	2.4
KTAG	N sector > 4 (within ± 3 ns)	6.3% (1.59) (15.9)	8.1% (1.6) (12.3)	26% (1.58) (3.84)
CHOD	N Crossing < 5 (within ± 5 ns)	4% (1.58) (25)	5.5% (1.47) (18.2)	20% (1.3) (5)
LAV	N complete hit < 2 (within ± 3 ns) (both leading and trailing of low and high threshold)	2.9% (1.38) (34.5)	4.3% (1.28) (23.3)	15% (1.33) (6.66)
STRAW	Z-vertex < 180 m && CDA<200 mm && track momentum < 70 GeV && multitrack cut	1.5% (1.93) (66.7)	2.1% (2.05) (47.6)	6.4% (2.33) (15.5)
L1 Total Rejection Factor		6.7	6.2	6.4
L0-L1 Total Rejection Factor		67	48	15

Figure 5.33: Results for the L0 and L1 trigger using the $P_z < 70$ GeV/c condition for the L1 STRAW algorithm.

Detector	Condition	Fraction of initial events (Rejection factor detector) (total rejection factor)		
		3809 only CHOD/2, 0.6%	4069 only CHOD/200, 12%	4098 LKr/14, 60%
CHOD	Al least 1 crossing	93% (1.08) (1.08)	87% (1.15) (1.15)	94% (1.06) (1.06)
LKr	$E_{cluster} > 1.2$ GeV & $E_{total} < 20$ GeV	24% (3.88) (4.17)	28% (3.11) (3.57)	79% (1.19) (1.27)
MUV1	$E_{cluster} > 5$ GeV			
RICH	N SuperCells > 3	16% (1.5) (6.25)	19% (1.47) (5.26)	63% (1.25) (1.59)
MUV3	At least 1 tight signal	13% (1.23) (7.69)	16% (1.19) (6.25)	48% (1.31) (2.08)
LAV12	At least 1 hit (both leading of low and high threshold)	10% (1.3) (10)	13% (1.23) (7.69)	41% (1.17) (2.44)
L0 Total Rejection Factor		10	7.7	2.4
KTAG	N sector > 4 (within ± 3 ns)	6.3% (1.59) (15.9)	8.1% (1.6) (12.3)	26% (1.58) (3.84)
CHOD	N Crossing < 5 (within ± 5 ns)	4% (1.58) (25)	5.5% (1.47) (18.2)	20% (1.3) (5)
LAV	N complete hit < 2 (within ± 3 ns) (both leading and trailing of low and high threshold)	2.9% (1.38) (34.5)	4.3% (1.28) (23.3)	15% (1.33) (6.66)
STRAW	Z-vertex < 180 m && CDA<200 mm && track momentum < 50 GeV && multitrack cut	1.1% (2.66) (90.7)	1.4% (3.05) (70.9)	4.6% (3.24) (21.6)
L1 Total Rejection Factor		9.2	9.18	8.9
L0-L1 Total Rejection Factor		92	71	21

Figure 5.34: Results for the L0 and L1 trigger using the $P_z < 50$ GeV/c condition for the L1 STRAW algorithm.

The missing gap on the total L0 and L1 rejection must be achieved by the L0 to reach 1 MHz of L0 output rate. A possibility is to use a slightly tighter condition about LKr/MUV that indeed could supply by itself a rejection factor 25 (see figure 4.7).

Conclusions

The work presented in this thesis covers almost all the aspects of the common Trigger and Data Acquisition of the NA62 experiment that has as main goal the measurement the Branching Ratio of the ultra-rare $K^+ \to \pi^+ \nu\overline{\nu}$ decay, very useful to obtain a stringent test of the Standard Model.

This PhD work began with the development and the testing of the firmware of common boards of the NA62 TDAQ system: TDCB and TEL62. The TDCB is a daughter-board of the TEL62 and measures the detector hit times. The TEL62 processes and stores these detector data in a buffer memory; at the arrival of a L0 trigger request, it extracts the data within a programmable time window around the trigger time to send them to the PC farm. The TEL62s of some detectors also take care of producing the L0 trigger primitives that are merged to generate L0 trigger requests.

In this thesis is described (chapter 3) the significant contribution given to the developing, the testing and the commissioning of the TDCB and TEL62 firmware. Since the 2012 Technical Run to the 2015 Run the system was tested, and evolved to be compatible with the detector input rate and the beam at growing intensity up to nominal. After three main versions the system composed by TDCB and TEL62 manages to cope with the design rate.

Once the work on the Data Acquisition system was concluded, I focuses on the Trigger system and the analysis of the L0 and L1 triggers. The goal of this work was to study the detector response and the trigger conditions required to obtain the needed rejection factor with the minimum amount of signal loss. Starting from 13 MHz of event rate, the L0 trigger must provide a factor 13 of rejection to reach the design L0 output rate of 1 MHz; the L1 trigger should provide a rejection of a factor 10 to achieve the goal of 100 KHz of L1 event output rate. The starting L0 and L1 scheme analysed in chapter 4 failed to reach the output rate request by a factor 5. This gap could be filled only by using the STRAW spectrometer at the L1. For this reason in the last part of this work (see chapter 5) the development of a L1 STRAW algorithm is described, starting from a Monte Carlo simulation and validating with the use of real data samples used for the L0 and L1 analysis.

The results reached by the STRAW algorithm (a rejection factor of about 3) plus other improvements allows to achieve the required L1 rejection factor and the goal of 100 kHz L1 output rate is reachable by using a tighter LKr/MUV condition al L0.

Bibliography

[1] R Aaij et al. "Precision measurement of the B_s^0-$\bar{B}_s^0$ oscillation frequency with the decay $B_s^0 \to D_s^- \pi^+$". In: *New J. Phys.* 15 (2013), p. 053021. DOI: 10.1088/1367-2630/15/5/053021. arXiv: 1304.4741 [hep-ex].

[2] A. Abulencia et al. "Observation of $B_s^0 - \bar{B}_s^0$ Oscillations". In: *Phys. Rev. Lett.* 97 (2006), p. 242003. DOI: 10.1103/PhysRevLett.97.242003. arXiv: hep-ex/0609040 [hep-ex].

[3] S. Adler et al. "Evidence for the decay K+ —> pi+ neutrino anti-neutrino". In: *Phys. Rev. Lett.* 79 (1997), pp. 2204–2207. DOI: 10.1103/PhysRevLett.79.2204. arXiv: hep-ex/9708031 [hep-ex].

[4] Stephen Scott Adler et al. "Search for the decay K+ —> pi+ nu anti-nu in the momentum region P(pi) less than 195-MeV/c". In: *Phys. Lett.* B537 (2002), pp. 211–216. DOI: 10.1016/S0370-2693(02)01911-1. arXiv: hep-ex/0201037 [hep-ex].

[5] S. Adler et al. "Further Evidence for the Decay $K^+ \to \pi^+ \nu\overline{\nu}$". In: *Phys. Rev. Lett.* 88 (4 Jan. 2002), p. 041803. DOI: 10.1103/PhysRevLett.88.041803. URL: http://link.aps.org/doi/10.1103/PhysRevLett.88.041803.

[6] K. Ahmet et al. "The OPAL detector at LEP". In: *Nucl. Instrum. Meth.* A305 (1991), pp. 275–319. DOI: 10.1016/0168-9002(91)90547-4.

[7] Valentina Akishina et al. "FLES - First Level Event Selection Package for the CBM Experiment". In: *Proceedings, GPU Computing in High-Energy Physics (GPUHEP2014)*. 2015, pp. 23–29. DOI: 10.3204/DESY-PROC-2014-05/4. URL: http://inspirehep.net/record/1386618/files/4.pdf.

[8] J. Christiansen et al. *TTCrx reference manual*. 2004. URL: http://ttc.web.cern.ch/TTC/TTCrx_manual3.9.pdf.

[9] Altera®. *Cyclone III Device Handbook*. URL: http://www.altera.com/literature/hb/cyc3/cyclone3_handbook.pdf.

[10] Altera®. *DE4 board User Manual*. URL: ftp://ftp.altera.com/up/pub/Altera_Material/12.1/Boards/DE4/DE4_User_Manual.pdf.

[11] Altera®. *Quartus II Software*. URL: http://quartushelp.altera.com/13.1/.

[12] Altera®. *Serial Configuration (EPCS) Devices Datasheet*. URL: http://www.altera.com/literature/hb/cfg/cyc_c51014.pdf.

[13] Altera®. *Stratix III Device Handbook*. URL: http://www.altera.com/literature/hb/stx3/stratix3_handbook.pdf.

[14] Altera®. *Stratix IV Device Handbook*. URL: http://www.altera.com/literature/hb/stratix-iv/stratix4_handbook.pdf.

[15] A. Ambrosino et al. "NA62 Technical Design Document". In: (2010). URL: https://na62.web.cern.ch/NA62/Documents/TD_Full_doc_v10.pdf.

[16] R. Ammendola et al. "GPUs for the realtime low-level trigger of the NA62 experiment at CERN". In: *Proceedings, GPU Computing in High-Energy Physics (GPUHEP2014)*. 2015, pp. 79–85. DOI: 10.3204/DESY-PROC-2014-05/15. URL: http://inspirehep.net/record/1386624/files/15.pdf.

[17] B. Angelucci et al. "TEL62: an integrated trigger and data acquisition board". In: *Proceedings, 2011 IEEE Nuclear Science Symposium and Medical Imaging Conference (NSS/MIC 2011)*. 2011, pp. 823–826. DOI: 10.1109/NSSMIC.2011.6154547.

[18] F. Anghinolfi et al. "NINO: An ultra-fast and low-power front-end amplifier/discriminator ASIC designed for the multigap resistive plate chamber". In: *Nucl. Instrum. Meth.* A533 (2004), pp. 183–187. DOI: 10.1016/j.nima.2004.07.024.

[19] V. V. Anisimovsky et al. "Improved measurement of the K+ —> pi+ nu anti-nu branching ratio". In: *Phys. Rev. Lett.* 93 (2004), p. 031801. DOI: 10.1103/PhysRevLett.93.031801. arXiv: hep-ex/0403036 [hep-ex].

[20] A. Antonelli et al. "The NA62 LAV front-end electronics". In: *JINST* 7 (2012), p. C01097. DOI: 10.1088/1748-0221/7/01/C01097. arXiv: 1111.5768 [physics.ins-det].

[21] A. V. Artamonov et al. "Study of the decay $K^+ \to \pi^+ \nu\bar{\nu}$ in the momentum region $140 < P_\pi < 199$ MeV/c". In: *Phys. Rev.* D79 (2009), p. 092004. DOI: 10.1103/PhysRevD.79.092004. arXiv: 0903.0030 [hep-ex].

[22] A. V. Artamonov et al. "New Measurement of the $K^+ \to \pi^+ \nu\overline{\nu}$ Branching Ratio". In: *Phys. Rev. Lett.* 101 (19 Nov. 2008), p. 191802. DOI: 10.1103/PhysRevLett.101.191802. URL: http://link.aps.org/doi/10.1103/PhysRevLett.101.191802.

[23] Y. Asano et al. "Search for a Rare Decay Mode K+ —> pi+ Neutrino antineutrino and Axion". In: *Phys. Lett.* B107 (1981), p. 159. DOI: 10.1016/0370-2693(81)91172-2.

[24] N. Azorskiy et al. "The NA62 spectrometer acquisition system". In: *Journal of Instrumentation* 11.02 (2016), p. C02064. URL: http://stacks.iop.org/1748-0221/11/i=02/a=C02064.

[25] M. Barbanera et al. "First operation of the level-0 trigger of the NA62 liquid krypton calorimeter". In: *JINST* 10.03 (2015), p. C03050. DOI: 10.1088/1748-0221/10/03/C03050.

[26] S. Baron. *Timing, Trigger and Control (TTC) Systems for the LHC*. 2013. URL: http://ttc.web.cern.ch/ttc/intro.html.

[27] Matteo Bauce et al. "The GAP project: GPU applications for High Level Trigger and Medical Imaging". In: *Proceedings, GPU Computing in High-Energy Physics (GPUHEP2014)*. 2015, pp. 3–8. DOI: 10.3204/DESY-PROC-2014-05/1. URL: http://inspirehep.net/record/1386616/files/1.pdf.

[28] Matteo Bauce et al. "Use of hardware accelerators for ATLAS computing". In: *Proceedings, GPU Computing in High-Energy Physics (GPUHEP2014)*. 2015, pp. 48–54. DOI: 10.3204/DESY-PROC-2014-05/10. URL: http://inspirehep.net/record/1386621/files/10.pdf.

[29] Biplob Bhattacherjee, Amit Chakraborty, and Arghya Choudhury. "Status of the MSSM Higgs sector using global analysis and direct search bounds, and future prospects at the High Luminosity LHC". In: *Phys. Rev.* D92.9 (2015), p. 093007. DOI: 10.1103/PhysRevD.92.093007. arXiv: 1504.04308 [hep-ph].

[30] Johan Bijnens and Karim Ghorbani. "Isospin breaking in K pi vector form-factors for the weak and rare decays K(l 3), K —> pi nu anti-nu and K —> pi l+ l-". In: (2007). arXiv: 0711.0148 [hep-ph].

[31] Monika Blanke et al. "FCNC Processes in the Littlest Higgs Model with T-Parity: a 2009 Look". In: *Acta Phys. Polon.* B41 (2010), pp. 657–683. arXiv: 0906.5454 [hep-ph].

[32] Monika Blanke et al. "Rare K and B Decays in a Warped Extra Dimension with Custodial Protection". In: *JHEP* 03 (2009), p. 108. DOI: 10.1088/1126-6708/2009/03/108. arXiv: 0812.3803 [hep-ph].

[33] Claudio Bonati et al., eds. *Proceedings, GPU Computing in High-Energy Physics (GPUHEP2014)*. DESY. Hamburg, Germany: DESY, 2015. DOI: 10.3204/DESY-PROC-2014-05.

[34] C. Bovet, S. Milner, and A. Placci. "The Cedar Project. Cherenkov Differential Counters with Achromatic Ring Focus". In: *IEEE Trans. Nucl. Sci.* 25 (1978), pp. 572–576. DOI: 10.1109/TNS.1978.4329375.

[35] C. Bovet et al. "The Cedar Counters for Particle Identification in the SPS Secondary Beams: A Description and an Operation Manual". In: (1982).

[36] Joachim Brod and Martin Gorbahn. "Electroweak Corrections to the Charm Quark Contribution to K+ —> pi+ nu anti-nu". In: *Phys. Rev.* D78 (2008), p. 034006. DOI: 10.1103/PhysRevD.78.034006. arXiv: 0805.4119 [hep-ph].

[37] Joachim Brod, Martin Gorbahn, and Emmanuel Stamou. "Two-loop electroweak corrections for the $K^+ \to \pi^+ \nu\overline{\nu}$ decays". In: *Phys. Rev. D* 83 (3 Feb. 2011), p. 034030. DOI: 10.1103/PhysRevD.83.034030. URL: http://link.aps.org/doi/10.1103/PhysRevD.83.034030.

[38] Gerhard Buchalla and Andrzej J. Buras. "The rare decays $K \to \pi\nu\bar{\nu}$, $B \to X\nu\bar{\nu}$ and $B \to l^+l^-$: An Update". In: *Nucl. Phys.* B548 (1999), pp. 309–327. DOI: 10.1016/S0550-3213(99)00149-2. arXiv: hep-ph/9901288 [hep-ph].

[39] A. J. Buras et al. "The Rare decay K+ —> pi+ nu anti-nu at the next-to-next-to-leading order in QCD". In: *Phys. Rev. Lett.* 95 (2005), p. 261805. DOI: 10.1103/PhysRevLett.95.261805. arXiv: hep-ph/0508165 [hep-ph].

[40] Andrzej J. Buras and Robert Fleischer. "Bounds on the unitarity triangle, sin 2 beta and $K \to$ neutrino anti-neutrino decays in models with minimal flavor violation". In: *Phys. Rev.* D64 (2001), p. 115010. DOI: 10.1103/PhysRevD.64.115010. arXiv: hep-ph/0104238 [hep-ph].

[41] Andrzej J. Buras, Andrea Romanino, and Luca Silvestrini. "K —> pi neutrino anti-neutrino: A Model independent analysis and supersymmetry". In: *Nucl. Phys.* B520 (1998), pp. 3–30. DOI: 10.1016/S0550-3213(98)00169-2. arXiv: hep-ph/9712398 [hep-ph].

[42] Andrzej J. Buras et al. "Patterns of Flavour Violation in the Presence of a Fourth Generation of Quarks and Leptons". In: *JHEP* 09 (2010), p. 106. DOI: 10.1007/JHEP09(2010)106. arXiv: 1002.2126 [hep-ph].

[43] Nicola Cabibbo. "Unitary Symmetry and Leptonic Decays". In: *Phys. Rev. Lett.* 10 (1963). [,648(1963)], pp. 531–533. DOI: 10.1103/PhysRevLett.10.531.

[44] G. D. Cable et al. "Search for rare k+ decays. ii. k+ —> pi+ nu anti-nu". In: *Phys. Rev.* D8 (1973), pp. 3807–3812. DOI: 10.1103/PhysRevD.8.3807.

[45] U. Camerini et al. "Experimental search for semileptonic neutrino neutral currents". In: *Phys. Rev. Lett.* 23 (1969), pp. 326–329. DOI: 10.1103/PhysRevLett.23.326.

[46] A. Ceccucci et al. "The NA62 liquid Krypton calorimeter's new readout system". In: *JINST* 9.01 (2014), p. C01047. DOI: 10.1088/1748-0221/9/01/C01047.

[47] Nikolai Chernov. *Circular and linear regression : fitting circles and lines by least squares*. Monographs on statistics and applied probability. A Chapman & Hall book. Boca Raton: CRC Press/Taylor & Francis, 2011. ISBN: 978-1-439-83590-6. URL: http://opac.inria.fr/record=b1131877.

[48] I. H. Chiang et al. "CsI endcap photon detector for a K+ —> pi+ nu anti-nu experiment at BNL". In: *IEEE Trans. Nucl. Sci.* 42 (1995), pp. 394–400. DOI: 10.1109/23.467813.

[49] J. Christiansen. *HPTDC, High Performance Time to Digital Converter*. 2004. URL: http://tdc.web.cern.ch/tdc/hptdc/docs/hptdc_manual_ver2.2.pdf.

[50] NA62 Collaboration. *NA62 Technical Design*. 2010. URL: https://na62.web.cern.ch/na62/Documents/TD_Full_doc_v10.pdf.

[51] G. Collazuol et al. "Fast online triggering in high-energy physics experiments using GPUs". In: *Nucl. Instrum. Meth.* A662 (2012), pp. 49–54. DOI: 10.1016/j.nima.2011.09.057.

[52] R.O. Duda and P.E. Hart. *Use of the Hough Transformation to Detect Lines and Curves in Pictures*. Tech. rep. 36. SRI Project 8259 Comm. ACM, Vol 15, No. 1. 333 Ravenswood Ave, Menlo Park, CA 94025: AI Center, SRI International, Apr. 1971.

[53] D Emeliyanov and J Howard. "GPU-Based Tracking Algorithms for the ATLAS High-Level Trigger". In: *Journal of Physics: Conference Series* 396.1 (2012), p. 012018. URL: http://stacks.iop.org/1742-6596/396/i=1/a=012018.

[54] V. Fanti et al. "The Beam and detector for the NA48 neutral kaon CP violations experiment at CERN". In: *Nucl. Instrum. Meth.* A574 (2007), pp. 433–471. DOI: 10.1016/j.nima.2007.01.178.

[55] F. Fontanelli et al. *CC-PC Gluecard Application and User's Guide*. 2003. URL: https://edms.cern.ch/file/500461/1/lhcb-2003-098.pdf.

[56] Stefano Gallorini. "Track pattern-recognition on GPGPUs in the LHCb experiment". In: *Proceedings, GPU Computing in High-Energy Physics (GPUHEP2014)*. 2015, pp. 38–43. DOI: 10.3204/DESY-PROC-2014-05/7. URL: http://inspirehep.net/record/1386620/files/7.pdf.

[57] *General-purpose computing on graphics processing units*. URL: http://en.wikipedia.org/wiki/General-purpose_computing_on_graphics_processing_units#Applications..

[58] S. L. Glashow, J. Iliopoulos, and L. Maiani. "Weak Interactions with Lepton-Hadron Symmetry". In: *Phys. Rev.* D2 (1970), pp. 1285–1292. DOI: 10.1103/PhysRevD.2.1285.

[59] E. Goudzovski and C. Parkinson. "Studies of the L0 trigger for rare decays". In: *Note NA62-14-07* (2014).

[60] Mentor Graphics®. *HDL Designer*. URL: https://www.mentor.com/products/fpga/hdl_design/hdl_designer_series.

[61] Mentor Graphics®. *ModelSim®*. URL: https://www.mentor.com/products/fpga/verification-simulation/modelsim/.

[62] Yuval Grossman and Yosef Nir. "K(L) —> pi0 neutrino anti-neutrino beyond the standard model". In: *Phys. Lett.* B398 (1997), pp. 163–168. DOI: 10.1016/S0370-2693(97)00210-4. arXiv: hep-ph/9701313 [hep-ph].

[63] Pisa TDAQ working group. *NA62 data formats*. 2016. URL: https://twiki.cern.ch/twiki/pub/NA62/TdaqSystem/DataFormats.pdf.

[64] The NA62 Pisa group. *TDCB Documentation*. 2016. URL: https://twiki.cern.ch/twiki/pub/NA62/TDAQFirmwareTdcb/TDCB-Manual.pdf.

[65] G. Haefeli et al. "The LHCb DAQ interface board TELL1". In: *Nucl. Instrum. Meth.* A560 (2006), pp. 494–502. DOI: 10.1016/j.nima.2005.12.212.

[66] Andreas Herten. "GPU-based Online Tracking for the PANDA Experiment". In: *Proceedings, GPU Computing in High-Energy Physics (GPUHEP2014)*. 2015, pp. 57–63. DOI: 10.3204/DESY-PROC-2014-05/11. URL: http://inspirehep.net/record/1386622/files/11.pdf.

[67] T. Inami and C. S. Lim. "Effects of Superheavy Quarks and Leptons in Low-Energy Weak Processes k(L) —> mu anti-mu, K+ —> pi+ Neutrino anti-neutrino and K0 <—> anti-K0". In: *Prog. Theor. Phys.* 65 (1981). [Erratum: Prog. Theor. Phys.65,1772(1981)], p. 297. DOI: 10.1143/PTP.65.297.

[68] Gino Isidori, Federico Mescia, and Christopher Smith. "Light-quark loops in K —> pi nu anti-nu". In: *Nucl. Phys.* B718 (2005), pp. 319–338. DOI: 10.1016/j.nuclphysb.2005.04.008. arXiv: hep-ph/0503107 [hep-ph].

[69] Gino Isidori et al. "Exploring the flavour structure of the MSSM with rare K decays". In: *JHEP* 08 (2006), p. 064. DOI: 10.1088/1126-6708/2006/08/064. arXiv: hep-ph/0604074 [hep-ph].

[70] P. Jovanovic. *Local Trigger Unit Preliminary Design Review.* URL: http://www.physi.uni-heidelberg.de/~minjung/tmp/LTU_ALICE-INT-2003-056.pdf.

[71] A. Kluge et al. "The {TDCpix} readout ASIC: A 75 ps resolution timing front-end for the {NA62} Gigatracker hybrid pixel detector". In: *Nuclear Instruments and Methods in Physics Research Section A: Accelerators, Spectrometers, Detectors and Associated Equipment* 732 (2013). Vienna Conference on Instrumentation 2013, pp. 511–514. ISSN: 0168-9002. DOI: http://dx.doi.org/10.1016/j.nima.2013.06.089. URL: http://www.sciencedirect.com/science/article/pii/S0168900213009352.

[72] Makoto Kobayashi and Toshihide Maskawa. "CP Violation in the Renormalizable Theory of Weak Interaction". In: *Prog. Theor. Phys.* 49 (1973), pp. 652–657. DOI: 10.1143/PTP.49.652.

[73] G. Lamanna. "Almagest, a new trackless ring finding algorithm". In: *Nucl. Instrum. Meth.* A766 (2014), pp. 241–244. DOI: 10.1016/j.nima.2014.05.073.

[74] LHCb. *Credit-Card PCs as ECS interface.* URL: http://lhcb-online.web.cern.ch/lhcb-online/ecs/ccpc/.

[75] P. Lichard et al. "Performance evaluation of multiple (32 channels) subnanosecond TDC implemented in low-cost FPGA". In: *JINST* 9 (2014), p. C03013. DOI: 10.1088/1748-0221/9/03/C03013.

[76] A. Lonardo et al. "NaNet: a configurable NIC bridging the gap between HPC and real-time HEP GPU computing". In: *JINST* 10.04 (2015), p. C04011. DOI: 10.1088/1748-0221/10/04/C04011.

[77] W. J. Marciano and Zohreh Parsa. "Rare kaon decays with 'missing energy'". In: *Phys. Rev.* D53 (1996), pp. 1–5. DOI: 10.1103/PhysRevD.53.R1.

[78] Federico Mescia and Christopher Smith. "Improved estimates of rare K decay matrix-elements from Kl3 decays". In: *Phys. Rev.* D76 (2007), p. 034017. DOI: 10.1103/PhysRevD.76.034017. arXiv: 0705.2025 [hep-ph].

[79] Mikolaj Misiak and Jorg Urban. "QCD corrections to FCNC decays mediated by Z penguins and W boxes". In: *Phys. Lett.* B451 (1999), pp. 161–169. DOI: 10.1016/S0370-2693(99)00150-1. arXiv: hep-ph/9901278 [hep-ph].

[80] D. Moraes et al. "The CARIOCA Front End Chip for the LHCb muon chambers". In: (2003).

[81] P. Moreira. *QPLL project*. 2005. URL: http://proj-qpll.web.cern.ch/proj-qpll/.

[82] H. Muller et al. *Quad Gigabit Ethernet plug-in card*. URL: https://edms.cern.ch/file/520885/2/gbe_manual_ver2.pdf.

[83] *NA62 framework*. URL: http://sergiant.web.cern.ch/sergiant/NA62FW/html/.

[84] K. A. Olive et al. "Review of Particle Physics". In: *Chin. Phys.* C38 (2014), p. 090001. DOI: 10.1088/1674-1137/38/9/090001.

[85] Elena Pedreschi et al. "A high-resolution TDC-based board for a fully digital trigger and data acquisition system in the NA62 experiment at CERN". In: *IEEE Trans. Nucl. Sci.* 62.3 (2015), pp. 1050–1055. DOI: 10.1109/RTC.2014.7097526,10.1109/TNS.2015.2423702. arXiv: 1407.2456 [physics.ins-det].

[86] Jacopo Pinzino. "Algoritimi di trigger paralleli per la ricerca di decadimenti rari del mesone k algoritim". PhD thesis. Pisa U., 2011. URL: http://etd.adm.unipi.it/theses/available/etd-09242011-182438/.

[87] G. Ruggiero. "Monte Carlo studies of a L0 trigger scheme for $K^+ \to \pi^+\nu\overline{\nu}$". In: *Note NA62-14-01* (2014).

[88] Franco Spinella et al. "The TEL62: A real-time board for the NA62 Trigger and Data AcQuisition. Data flow and firmware design". In: *Proceedings, 19th Real Time Conference (RT2014)*. 2014. DOI: 10.1109/RTC.2014.7097525.

[89] David M. Straub. "New physics correlations in rare decays". In: *CKM unitarity triangle. Proceedings, 6th International Workshop, CKM 2010, Warwick, UK, September 6-10, 2010*. 2010. arXiv: 1012.3893 [hep-ph]. URL: https://inspirehep.net/record/881964/files/arXiv:1012.3893.pdf.

[90] G. Taubin. "Estimation of planar curves, surfaces, and nonplanar space curves defined by implicit equations with applications to edge and range image segmentation". In: *IEEE Transactions on Pattern Analysis and Machine Intelligence* 13.11 (Nov. 1991), pp. 1115–1138. ISSN: 0162-8828. DOI: 10.1109/34.103273.

[91] B. G. Taylor. *TTC laser transmitter (TTCex, TTCtx, TTCmx) user manual*. URL: http://ttc.web.cern.ch/TTC/TTCtxManual.pdf.

[92] Lincoln Wolfenstein. "Parametrization of the Kobayashi-Maskawa Matrix". In: *Phys. Rev. Lett.* 51 (1983), p. 1945. DOI: 10.1103/PhysRevLett.51.1945.